University of Tennessee, Knoxville
TRACE: Tennessee Research and Creative Exchange

Doctoral Dissertations | Graduate School

5-2022

The Upgraded Measurement of the Neutron Lifetime Using the In-Beam Method

Jimmy P. Caylor
University of Tennessee, Knoxville, jcaylor2@vols.utk.edu

Follow this and additional works at: https://trace.tennessee.edu/utk_graddiss

 Part of the Nuclear Commons

Recommended Citation

Caylor, Jimmy P., "The Upgraded Measurement of the Neutron Lifetime Using the In-Beam Method. " PhD diss., University of Tennessee, 2022.
https://trace.tennessee.edu/utk_graddiss/7195

This Dissertation is brought to you for free and open access by the Graduate School at TRACE: Tennessee Research and Creative Exchange. It has been accepted for inclusion in Doctoral Dissertations by an authorized administrator of TRACE: Tennessee Research and Creative Exchange. For more information, please contact trace@utk.edu.

To the Graduate Council:

I am submitting herewith a dissertation written by Jimmy P. Caylor entitled "The Upgraded Measurement of the Neutron Lifetime Using the In-Beam Method." I have examined the final electronic copy of this dissertation for form and content and recommend that it be accepted in partial fulfillment of the requirements for the degree of Doctor of Philosophy, with a major in Physics.

Nadia Fomin, Major Professor

We have read this dissertation and recommend its acceptance:

Geoff Greene, Thomas Papenbrock, Sowjanya Gollapinni, David Donovan

Accepted for the Council:

Dixie L. Thompson

Vice Provost and Dean of the Graduate School

(Original signatures are on file with official student records.)

The Upgraded Measurement of the Neutron Lifetime Using the In-Beam Method

A Dissertation Presented for the

Doctor of Philosophy

Degree

The University of Tennessee, Knoxville

Jimmy Caylor

May 2022

© by Jimmy Caylor, 2022
All Rights Reserved.

Abstract

Precision measurements of neutron beta decay can provide answers to some of the most fundamental questions in particle physics, astrophysics and cosmology. Neutron beta decay is the simplest semi-leptonic decay; therefore, it provides a clean test of the charged current sector of the Standard Model (SM). A precise measurement of the neutron lifetime and λ, the ratio of axial vector and vector coupling constants of the weak interaction, allows for a determination of the Cabibbo-Kobayashi-Moskawa (CKM) matrix element V_{ud} that is free from nuclear structure effects. The SM predicts that the CKM matrix is unitary; therefore, the measurement of the neutron lifetime provides an important test of the SM. The neutron lifetime is also an important input parameter into early universe Big Bang Nucleosynthesis calculations. The neutron lifetime remains one of the most uncertain parameters in the calculation of cosmic ^4He abundance. The in-beam method of measuring the neutron lifetime requires the absolute counting of decay protons in a neutron beam of precisely known flux. Improvements in the neutron and proton detection systems as well as the use of a new analysis technique and apparatus upgrades allow for a rigorous re-examination of the systematic effects associated with this method. This work will discuss the development and optimization of new analysis techniques that provide improved proton energy resolution as well as an absolute timing comparison to simulation. The results of new proton systematic studies and a new simulation model will also be discussed.

Table of Contents

List of Tables

List of Figures

Chapter 1

Introduction and Theory

1.1 Discovery of the Neutron and Neutron Beta Decay

In March of 1896 while examining photographic plates upon which a uranium sulfate had been placed, Henri Becquerel discovered radioactivity when he observed the uranium emitted radiation without any external influence[10]. In the subsequent years, Earnest Rutherford and Paul Villard identified the observed radiation types by their penetrating depth, calling them alpha, beta, and gamma. Alpha particles were easily stopped by as little as a sheet of paper. Measuring the charge-to-mass ratio would eventually lead to identifying alpha radiation as the ^4He nucleus. Gamma rays were highly energetic and the most penetrating of the three types. As gamma radiation was unaffected by a magnetic field, it was thought to be massive and neutral. After Rutherford discovered that gamma radiation could be reflected off a crystal, gamma radiation was identified as electromagnetic radiation, photons [69]. Becquerel was able to measure the charge-to-mass ratio of beta radiation and found that it was consistent with J.J. Thomson's "cathode ray." This was the first evidence that beta radiation was an electron.

In 1920, Earnest Rutherford first proposed the idea of a neutral massive particle in the nucleus of an atom to account for the difference in atomic mass and atomic number [81]. In the early 1930s Walther Bothe, Herbert Becker, and Iréne and Frédéric Joliot-Curie carried out a set of experiments that showed that light elements irradiated with alpha particles would produce neutral penetrating radiation. They originally thought this was gamma radiation.

However in 1932, James Chadwick submitted evidence of the existence of the neutron [27]. To conserve energy and momentum, he identified the penetrating radiation from irradiated beryllium must be the neutron and not gamma radiation. In 1934 and 1935, while measuring the binding energies of deuterium and beryllium, Chadwick and Goldhaber showed that the neutron mass was between 1.005 and 1.008 atomic mass units, greater than that of the hydrogen atom [28][29]. This indicated that it was theoretically possible for the neutron to decay into a proton and an electron. This was in direct contradiction to Rutherford's proposal that the neutron was a tightly bound state of a proton and an electron.

Initially, beta decay was thought to be a two-body process that would lead to a very narrow band of electron energies. However, continuous electron spectra were observed in nuclear beta decay suggesting a violation of the conservation of energy. In 1930, a solution to this problem was suggested by Wolfgang Pauli [71]. He proposed that beta decay was a three body process to explain the observation of a continuous spectrum. He suggested an additional, neutral particle was ejected from the parent nucleus. Pauli called this particle a neutron however, it was later renamed to neutrino or "little neutral one" in Italian after Chadwick and Goldhaber showed the neutron mass to be inconsistent with the proposed additional particle. In 1934, Fermi first developed his formalism for beta decay. In this formalism, a neutron transforms into a proton while ejecting an electron and a neutrino [38]. It was not until the 1940s that neutron decay would be observed at the Oak Ridge Graphite Reactor [90, 91]. Shortly after at the NRX reactor in Chalk River, Ontario, Robson made what is considered the first measurement of the neutron lifetime [80]. Pauli's proposed neutrino went unconfirmed for more than 20 years until 1956 when Cowan and Reines made the first identification of a neutrino [33]. After these discoveries, it was clear that Pauli was correct and the neutron decays into a proton, electron and anti-neutrino as:

$$n \rightarrow p + e + \bar{\nu_e} + 782\, keV. \tag{1.1}$$

In the nearly 70 years since the detection of the first neutrino the field of nuclear physics has made many strides into understanding the subatomic world. Many other forms of decay have been discovered including: spontaneous fission, proton and neutron emission, and

positron emission, known as beta plus decay. The world of nuclear theory has also seen much advancement. From the starting point of Fermi's theory of beta decay, the Standard Model (SM) and other effective field theories have set a framework to describe nuclei. Still, 100 years after the discovery of the neutron there is plenty we still have to learn about neutron beta decay.

1.2 Theory of Nuclear Beta Decay

In 1934, Fermi published the first theory of nuclear beta decay, which was the first attempt at describing the weak interaction [38]. He modeled it after the electromagnetic interaction as a 4-point interaction similar to the emission of a photon from an excited nucleus as seen in figure 1.1. The proposed matrix element for free neutron beta decay was a pure vector (V) interaction like the electromagnetic interaction and was given by:

$$\mathcal{M}_{Fermi} = G_F \langle u_p | \gamma_\mu | u_n \rangle \langle u_e | \gamma_\mu | u_\nu \rangle, \tag{1.2}$$

where u_p, u_n, u_e and u_ν are the proton, neutron, electron and neutrino spinors, γ_μ is the gamma matrix and G_F is the Fermi coupling constant [38]. In 1936, Gamow and Teller proposed that Lagrangian be extended to include all Lorentz-invariant interactions, this added the scalar (S), pseudoscalar (P), axial-vector (A) and tensor (T) terms to the vector term [43]. The generalized weak interaction matrix element is then given by:

$$\mathcal{M} = G_i \langle u_p | \mathcal{O}_i | u_n \rangle \langle u_e | \mathcal{O}_i | u_\nu \rangle, \tag{1.3}$$

where the operators $\mathcal{O}_i$ are given by the gamma matrices in table 1.1, and G_i is the interaction strength of each term. Two types of decays have been observed. Fermi decay $\Delta J = 0$, where ΔJ is the difference between the initial and final total angular momentum, leaves the leptons in a spin singlet state and is allowed by the scalar and vector currents. Gamow-Teller decay, $\Delta J = \pm 1$, leaves the leptons in a spin triplet and is allowed by the tensor and axial-vector currents. The P interaction is suppressed because neutron beta decay is non-relativistic.

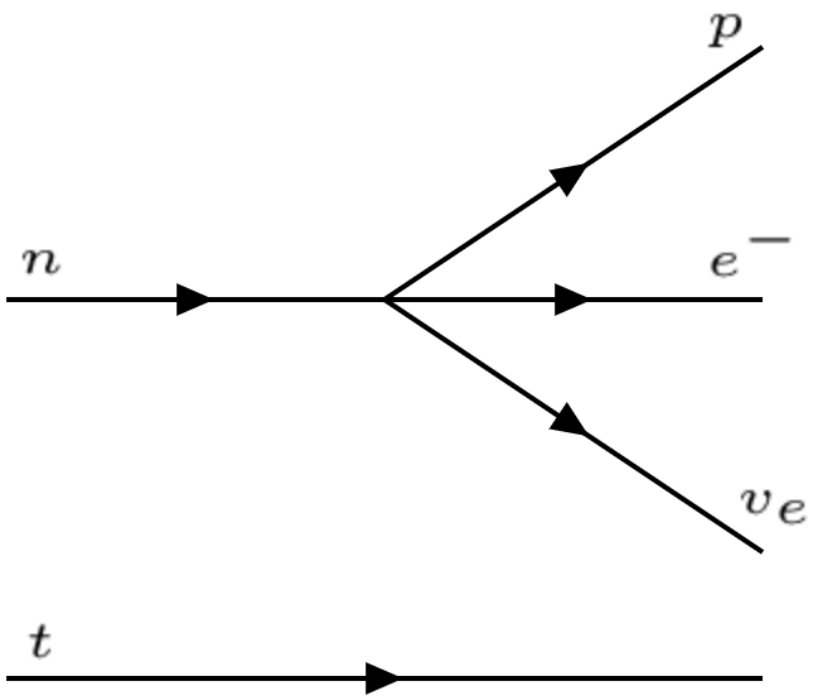

Figure 1.1: Neutron beta decay as described by Fermi's 4-point model.

Table 1.1: Bilinear Covariants

Interaction Type	$\mathcal{O}_i$
Scalar	$\mathcal{O}_S = \mathbb{I}$
Pseudoscalar	$\mathcal{O}_P = \gamma_5$
Vector	$\mathcal{O}_V = \gamma_\mu$
Axial-Vector	$\mathcal{O}_S = \gamma_\mu\gamma_5$
Tensor	$\mathcal{O}_T = \sigma_{\mu\nu} = \frac{i}{2}[\gamma_\mu, \gamma_\nu]$

By the 1950s, a problem with this theory of the weak interaction had developed. Two particles of the same mass, charge, and strangeness, Θ^+ and τ^+, were observed to have different final state parities. The particles decayed with the following reactions:

$$\Theta^+ \rightarrow \pi^+ + \pi^0$$
$$\tau^+ \rightarrow \pi^+ + \pi^+ + \pi^-.$$

The parity of each pion was known to be -1 so the initial parity of the Θ^+ was taken to be +1 and the parity of the τ^+ was taken to be -1. In 1956, Lee and Yang proposed that the weak interaction may not be parity conserving and suggested that the Θ^+ and the τ^+ are the same particle[1]. Shortly thereafter, an experiment done by Wu in collaboration with the Low Temperature Group at the National Bureau of Standards showed that the beta decay electron direction from polarized ^{60}Co was asymmetric [106]. With this and subsequent results [44, 41], it was clear that the weak interaction is parity violating and the theory must account for this.

Evidence from these experiments and others [40, 49] showed that the weak interaction only involves left-handed particles and right-handed antiparticles. Experiments showed that the V and A interactions were responsible for the weak interaction. To date, no evidence for scalar or tensor interactions has been found [52, 94]. In 1958, theorists showed that the particular form of the weak interaction was V-A [39, 96]. Throughout the 1960s and early 1970s the theory continued to be refined [101, 82, 48, 97, 54]. Thanks to their work, the matrix element for the weak interaction can be written as:

$$\mathcal{M} = \frac{G_F V_{ud}}{\sqrt{2}}[g_V \bar{u}_p \gamma_\mu u_n + g_A \bar{u}_p \gamma_\mu \gamma_5 u_n][\bar{u}_e \gamma_\mu (1-\gamma_5) u_\nu)]. \tag{1.4}$$

where V_{ud} is the up-down element from the Cabibbo-Kobayashi-Maskawa (CKM) quark mixing matrix. At the quark level the couplings, g_V and g_A, are identical, but strong interaction effects inside the nucleon can change their observed strength. For neutron beta decay we define $\lambda \equiv \frac{g_A}{g_V}$. Evaluating the neutron beta decay matrix element and integrating

[1]Lee and Yang were correct that the Θ^+ and the τ^+ were the same particle, we now know it as the K^+.

over the kinematic variables, the neutron decay rate at the tree level is given by:

$$\Gamma = \frac{1}{\tau_n} = \frac{f^R m_e^5 c^4}{2\pi^3 \hbar^7} G_F^2 |V_{ud}|^2 (|g_V|^2 + 3|g_A|^2), \tag{1.5}$$

where f^R is a phase space factor and m_e is the electron mass. Using λ, we can rewrite the neutron lifetime as:

$$\tau_n = \frac{2\pi^3 \hbar^7}{m_e^5 c^4 f^R G_F^2 |V_{ud}|^2 (1 + 3|\lambda|^2)} = \frac{5099.34\, s}{|V_{ud}|^2 (1 + 3\lambda^2)(1 + \Delta_R)}. \tag{1.6}$$

Evaluating the expression, we can see the neutron lifetime can be written as a function of V_{ud} and λ as:

$$\tau_n = \frac{5099.34\, s}{|V_{ud}|^2 (1 + 3\lambda^2)(1 + \Delta_R)}, \tag{1.7}$$

where Δ_R is a radiative correction [36, 86].

In general, a description of the weak interaction should include the massive gauge bosons, the charged $W^{\pm}$ and the neutral Z^0. In neutron beta decay, the down quark of the neutron transitions into the up quark of the proton via emission of a virtual W^- boson that promptly decays into an electron and an anti-neutrino as seen in figure 1.2. This leads to two three-particle vertices that must be calculated rather than a single four-particle vertex. The propagation term of this interaction is given by $\frac{1}{M_W^2 - q^2}$ where M_W is the mass of the W^- boson and q is the momentum transfer. At low energies, where $M_W^2 >> q^2$ the propagation term can be treated as solely $\frac{1}{M_W^2}$. The Fermi interaction is an example of an effective field theory. This effective field theory method is relevant here as the W mass ($80.379 \pm 0.012 GeV/c^2$) [74] is much greater than any energy transfer between the initial and final states. In the low energy limit, the coupling is $\frac{G_F}{\sqrt{2}} = \frac{g_w^2}{8 M_W^2}$, where g_w is the weak coupling and the 8 is from SM convention [18].

1.3 Measuring V_{ud} from Neutron Beta Decay

The CKM matrix describes the mixing between the weak and mass eigenstates of quarks [60]. The Standard Model requires the CKM matrix to be unitary, any deviation from

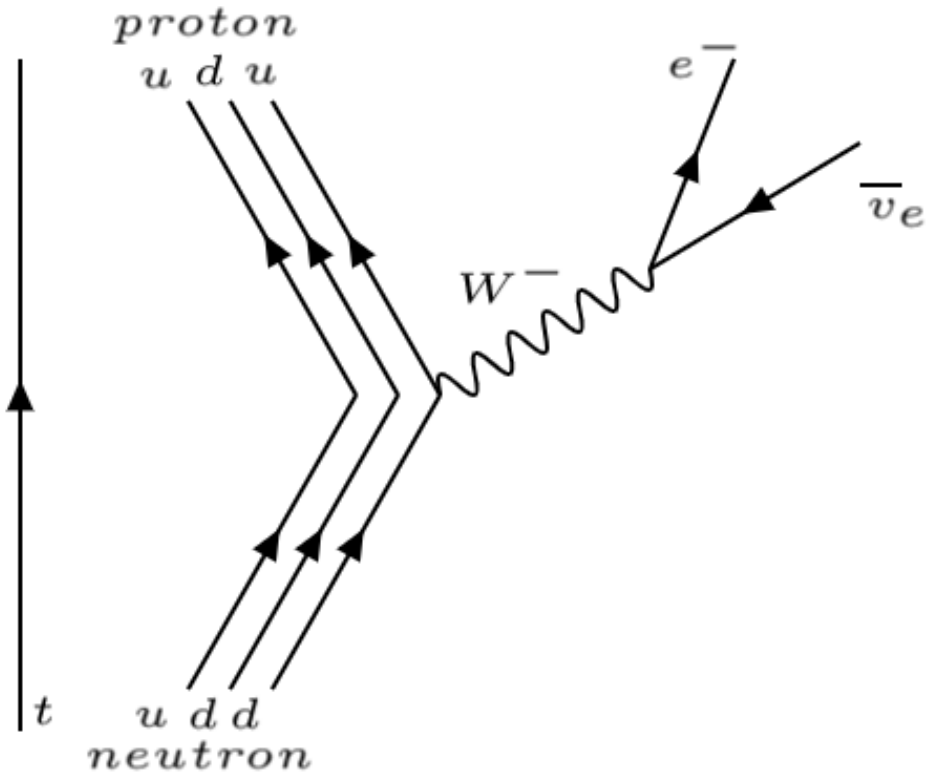

Figure 1.2: Feynman diagram of neutron beta decay showing the constituent quarks and the virtual W^- boson.

unitarity would indicate some kind of beyond the Standard Model (BSM) physics such as a deviation from the V-A nature of the weak interaction or another generation of particles. The CKM matrix elements are not calculable and must be determined by experiment. The most relevant test of CKM unitary for neutron beta decay is sum of the squares of the top row as:

$$\Delta_{CKM} = 1 - |V_{ud}|^2 - |V_{us}|^2 - |V_{ub}|^2, \tag{1.8}$$

where the matrix elements correspond to the mixing between the up quark with the down, strange, and bottom quark respectively and Δ_{CKM} is the deviation from unitarity.

1.3.1 V_{ud} from Superallowed Decay

The current best extraction of V_{ud} is from $0^+ \rightarrow 0^+$ superallowed nuclear decays. These decays are between nuclei that are analogs of spin and parity ($\Delta J = 0$ and parity even) and are pure vector decays. This experimental method attempts to minimize nuclear structure corrections by using nuclei with maximal overlap in the initial and final states. The strength of these decays are measured with an $\mathcal{F}t$ value. This $\mathcal{F}t$ is a function of the energy, half-life and branching ratio of the decay. The $\mathcal{F}t$ value is given by:

$$\mathcal{F}t \equiv ft(1+\delta_r^{'})(1+\delta_{NS}+\delta_C) = \frac{K}{2G_V^2(1+\Delta_R^V)}, \tag{1.9}$$

where G_V is defined as $G_F V_{ud}$, $K = 8120.27648(26) \times 10^{-10}\, GeV^{-4}s$, and $\delta_R^{'}, \delta_{NS}, \delta_C$, and Δ_R^V are the transition dependent radiative, nuclear structure, isospin-symmetry-breaking and universal radiative corrections [53]. Because of conserved vector current hypothesis many pure vector decays may be averaged together to get a more precise measurement of V_{ud}. Rearranging equation 1.9, V_{ud} is given as:

$$|V_{ud}|^2 = \frac{G_V^2}{G_F^2} = \frac{K}{2G_F^2(1+\Delta_R^V)\bar{\mathcal{F}t}}, \tag{1.10}$$

where $\bar{\mathcal{F}t}$ is the average over all $\mathcal{F}t$ values. G_F is well known from muon decay [74] and the $\mathcal{F}t$ values are consistent with one another, confirming the conserved vector current hypothesis, leading to a determination of $V_{ud} = 0.97373 \pm 0.00031$ [53]. This value is actually significantly

lower and somewhat less precise than the previous results. The shift resulted from new calculations of the universal radiative correction that will be covered in more detail later in the chapter. The reduction of precision largely comes from the introduction of a new term in the δ_{NC} correction that, when combined with the previous correction [99], largely does not change the central value but expanded the errors [51].

1.3.2 V_{ud} from Neutron Beta Decay

Extracting V_{ud} from neutron beta decay requires two experimental measurements, τ_n and λ. The measurement of τ_n will be covered extensively later in this work, but in order to measure λ, consider the differential decay rate give in reference [57]. This decay rate parameterizes neutron beta decay as a function of the electron and anti-neutrino energy and momenta as:

$$\frac{dw}{dE_e d\Omega_e d\Omega_\nu} \propto p_e E_e (E_0 - E_e)^2 \times \left[1 + a\frac{\vec{p_e}\cdot\vec{p_\nu}}{E_e E_\nu} + b\frac{m_e}{E_e} + \langle\vec{\sigma_n}\rangle\left(A\frac{\vec{p_e}}{E_e} + B\frac{\vec{p_\nu}}{E_\nu} + D\frac{\vec{p_e}\times\vec{p_\nu}}{E_e E_\nu}\right)\ldots\right], \tag{1.11}$$

where p_e, p_ν, E_e and E_ν are the momenta and energy of the decay electron and anti-neutrino, E_0 is the end point energy of the electron, $\vec{\sigma}_n$ is the neutron spin, and a, b, A, B, and D are the so-called correlation coefficients. Here, we will focus on a and A, the correlations coefficients most commonly used to determine λ. The a and A correlation coefficients are purely a function of λ.

Currently, the most precise method of measuring λ comes from measuring the neutron spin-electron asymmetry, A. The world's most precise measurement of A used the PERKEO III spectrometer at the Institut Laue-Langevin. The experiment used a cold neutron beam that was polarized using a supermirror polarizer. After the beam was polarized, a rotating disk chopper was used to create a pulsed beam. Using a pulsed beam, the neutron bunches were temporarily stored in-flight in the 8 m long spectrometer to avoid edge effects. If a neutron decayed in this magnetic field region, the electron was transported to one of two plastic scintillator detectors upstream or downstream of the decay region. This resulted in a measurement of $A = -0.11955(21)$ and $\lambda = 1.27641(56)$ [65]. A systematically

independent measurement of λ can be made by measuring the electron and anti-neutrino angular correlation, a. The most precise measurement of a is from the aSPECT collaboration at the Institut Laue-Langevin. The experiment measured the electron and anti-neutrino angular correlation by measuring the energy spectrum of the recoiling proton. If the electron and anti-neutrino are emitted in the same direction the proton gains a larger recoil kick rather than if the electron and anti-neutrino are emitted in opposite directions. The neutron beam entered the apparatus in a region of high magnetic field, if the neutron decayed then the protons were trapped by the magnetic field. The protons were guided by the magnetic field and are detected with a spectrometer that is carefully designed to longitudinalize the proton's momentum before they are incident on a silicon drift detector. This resulted in a measurement of $a = -0.10430(84)$ and $\lambda = -1.2677(28)$ [8]. The most recent Particle Data Group (PDG) value for λ using neutron beta decay is $\lambda = -1.2754(13)$ [74], this includes a 2.7 scale factor on the uncertainty because of the non-statistical spread in the measured values. One may note however that the three most precise measurements of λ are in good agreement. Now that λ has been measured, V_{ud} may be calculated by using the neutron lifetime and applying the applicable radiative corrections.

To extract V_{ud} from neutron beta decay one must apply the universal radiative correction, Δ_R^V. This is the dominant correction term in free neutron beta decay and is present in all beta decays, this correction is approximately 2.4%. To extract V_{ud} from nuclear decays one must also apply the transition dependent radiative, isospin-breaking, and nuclear structure dependent corrections. For the measured super-allowed decays, $\delta_R^{'}$ varies between 1.4% and 1.7%, δ_C varies from 0.18% to 1.7% and δ_{NC} varies from 0.02% to 0.4%. Therefore, neutron beta decay provides a cleaner measurement with fewer theoretical corrections. However, the current experimental precision of neutron beta decay experiments are worse than the theoretical corrections.

1.3.3 Status of CKM Unitarity

As recently as 2019, the PDG overview of the first row of the CKM matrix found good agreement with unitarity [14].

$$\Delta_{CKM2019} = 1 - |V_{ud}|^2 - |V_{us}|^2 - |V_{ub}|^2 = 0.0006(5)$$

The results included in this determination used the radiative correction $\Delta_V^R = 0.02361(38)$ [64]. The reasonable agreement with unitarity was seen as another confirmation of the Standard Model and placed constraints on BSM physics. However in 2019, a new treatment of the universal radiative correction was published that reduced the error bars by approximately 40 % but shifted the value of the correction significantly. The new universal radiative correction is $\Delta_R^V = 0.02467(22)$ [86], a shift of approximately $3\,\sigma$. This new calculation directly affects the extraction of V_{ud} from both nuclear and neutron decay and had a significant effect on the consistency with unitarity. This new correction shifted the value of V_{ud} lower for both the nuclear and neutron decays and lead to significant tension with unitarity in the 2020 PDG [15].

$$\Delta_{CKM2020} = 1 - |V_{ud}|^2 - |V_{us}|^2 - |V_{ub}|^2 = 0.0015(5)$$

At present, due to the increased errors in the latest determination of V_{ud} because of δ_{NS}, the disagreement with unitarity is not as large. While the central value of V_{ud} did not significantly change, the error was expanded by approximately a factor of 2. The most current check of the top row of the CKM matrix shows a $\approx 2\,\sigma$ tension with predicted unitarity.

$$\Delta_{CKM2021} = 1 - |V_{ud}|^2 - |V_{us}|^2 - |V_{ub}|^2 = 0.0015(7)$$

This determination uses V_{ud} from superallowed decays. As mentioned earlier, neutron decay provides a somewhat cleaner, but less precise, determination of V_{ud}. One can also measure V_{ud} using pion decays, though very small branching ratios make this experiment difficult and

not competitive. The currently accepted values for V_{ud} are:

$$\begin{aligned} V_{ud} &= 0.97373(31) \text{ (superallowed decays) [53]} \\ V_{ud} &= 0.9737(9) \text{ (neutron decay) [16]} \\ V_{ud} &= 0.9749(21) \text{ (pion decay) [78]}, \end{aligned} \tag{1.12}$$

where the error in the evaluation for neutron decay includes a scale factor for both τ_n and λ due to inconsistencies in the data.

In order to understand the precision required for neutron beta decay experiments, we can expand the uncertainty of V_{ud} as:

$$\begin{aligned} \frac{\delta(|V_{ud}|^2)}{|V_{ud}|^2} = \Bigg[&\left(\frac{\delta K}{K}\right)^2 + \left(2\frac{\delta G_F}{G_F}\right)^2 + \left(\frac{\delta(1+\Delta_R^V)}{1+\Delta_R^V}\right)^2 \\ &+ \left(\frac{\delta f(1+\delta_R')}{f(1+\delta_R')}\right)^2 + \left(\frac{\delta\tau_n}{\tau_n}\right)^2 + \left(\frac{6\lambda\delta\lambda}{1+3\lambda^2}\right)^2 \Bigg]^{1/2} \text{[13]}, \end{aligned} \tag{1.13}$$

where $\frac{\delta K}{K}$ and $\frac{\delta G_F}{G_F}$ are negligible, $\frac{\delta(1+\Delta_R^V)}{1+\Delta_R^V} = 2.15 \times 10^{-4}$, $\frac{\delta f(1+\delta_R')}{f(1+\delta_R')} = 5.25 \times 10^{-5}$ [103]. and $\lambda = 1.27641(56)$. Inserting these values and collecting terms, equation 1.13 becomes:

$$\frac{\delta(|V_{ud}|^2)}{|V_{ud}|^2} \sim \left[4.885 \times 10^{-8} + 1.69 \cdot (\delta\lambda)^2 + \left(\frac{\delta\tau_n}{\tau_n}\right)^2\right]^{1/2}, \tag{1.14}$$

where the first term on the right is the collection of uncertainties from theory corrections. If one takes the error on V_{ud} from superallowed decays and simplifies equation 1.14, one can see that to have a competitive determination of V_{ud} from neutron beta decay

$$1.69 \cdot (\delta\lambda)^2 + \left(\frac{\delta\tau_n}{\tau_n}\right)^2 < 1.77 \times 10^{-7}. \tag{1.15}$$

Using the single most precise measurement of τ_n [50] and λ [65], the left side of equation 1.15 is 4.75×10^{-7}, not competitive with superallowed decays. To be competitive with the

current uncertainty on V_{ud} the neutron physics community must strive for a measurement of τ_n to ≈ 0.2 s uncertainly and λ to $\delta\lambda \approx 2 \times 10^{-4}$ relative uncertainly.

Until now we have focused solely on the V_{ud} element of the CKM matrix because that element dominates the test of unitarity. $|V_{ud}|^2$ makes up $\approx 95\%$ of the squares of the top row with $|V_{us}|^2$ constituting $\approx 5\%$ and $|V_{ub}|^2$ contributing a negligible fraction at $\approx 0.002\%$. V_{us} is typically determined in one of three ways, using kaon, hyperon, or tau decays. The most precise method for determining V_{us} is with kaon decays. Historically $K \to \pi e \nu_e$ was solely used to determine V_{us} because of large errors in the corrections of $K \to \pi \mu \nu_\mu$. Since the mid 2000s the form factors have been determined precisely enough for both decay types to be used. There are five kaon decay channels evaluated for the world data [4]. The currently accepted values for V_{us} are:

$$\begin{aligned} V_{us} &= 0.2243(8) \text{ (kaon decays) [16]} \\ V_{us} &= 0.2250(27) \text{ (hyperon decays) [24]} \\ V_{us} &= 0.2221(13) \text{ (tau decays) [2]}, \end{aligned} \tag{1.16}$$

where only the value from kaon decay is used for test of the first row of the CKM matrix.

1.4 Neutron Beta Decay and Big Bang Nucleosynthesis

The neutron lifetime is an important input parameter in Big Bang Nucleosynthesis models that predict the abundance of light (H, He and Li) nuclei in the early universe. The models use an input of the ratio of the neutrons to protons when these light elements start to form. The early universe is characterized by the temperature, T. After the Big Bang, the early universe was extremely hot, during this period the temperature was high enough that protons

and neutrons were in equilibrium with the following reactions:

$$n + e^+ \leftrightarrow p + \bar{\nu}_e \tag{1.17}$$
$$p + e^- \leftrightarrow n + \nu_e.$$

As the hot, early universe began to cool, the neutron to proton ratio was in thermal equilibrium as given by the Maxwell-Boltzmann distribution:

$$\frac{n}{p} \propto e^{\frac{-\Delta_m}{T}},$$

where Δ_m is the mass difference between the proton and the neutron. At approximately 1 s after the Big Bang (T $\approx$ 1 MeV) this interaction stops being the dominant process that determines the neutron to proton ratio. This so called "nucleon freeze-out" leaves the neutron to proton ratio at $\approx \frac{1}{6}$. However, the universe does not cool enough so that multiple nucleons can bind into nuclei until $\approx 200\,s$ after the Big Bang. During this period between 1 s and 200 s, the dominant factor in the neutron to proton ratio is the neutron lifetime as seen in figure 1.3. At the time when nucleosynthesis starts the neutron to proton ratio is $\approx \frac{1}{7}$, but the neutron lifetime gives the largest uncertainty[2] to this ratio for nucleosynthesis calculations [34, 32, 75]. Currently, measurements of early universe light element abundance are less precise than the theoretical predictions, but as measurements improve, the uncertainty in the neutron lifetime will have a larger impact in theoretical predictions.

1.5 Neutron Lifetime Measurement Methods

There are multiple different techniques for measuring the neutron lifetime. This is important because it allows for independent measurements of the neutron lifetime with differing systematic uncertainties. An agreement between the different experimental techniques would give confidence to the measurements. The two most mature experimental techniques are

[2]The individual uncertainties of the most precise neutron lifetime measurements are competitive with uncertainties from other inputs into nucleosynthesis models. The major uncertainty in the input comes from the difference in measured neutron lifetimes from the two major experimental techniques.

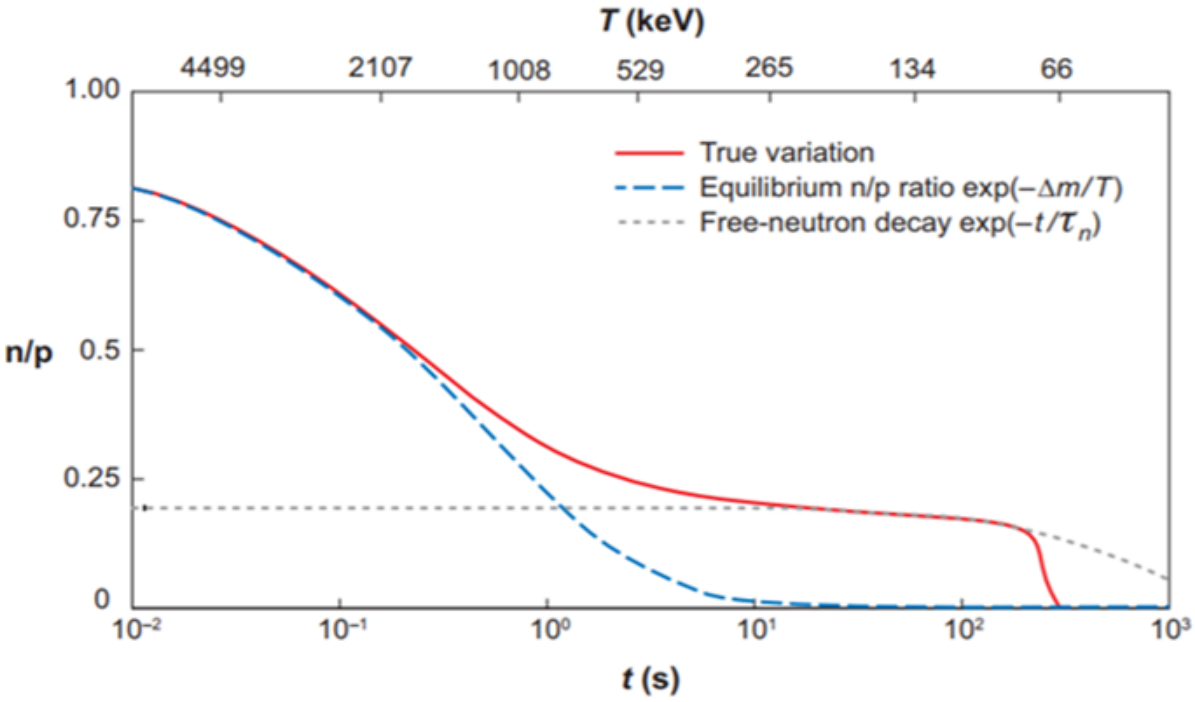

Figure 1.3: Variation of the neutron to proton ratio as a function of time and temperature in the early universe. The influence of the neutron lifetime is highlighted by the gray dashed line, taken from reference [88].

known as the "bottle" and "beam" methods. The bottle method traps ultracold neutrons (UCNs) in a combination of gravitational, material or magnetic traps and counts the number of neutrons that remain after a given holding time. The beam method uses a neutron beam and simultaneously measures the neutron fluence and the rate of the neutron decay products, either the proton or electron. A third type of experiment is currently ongoing that uses a time projection chamber. This experiment also uses a cold neutron beam but measures delayed protons from the $n(^3He,^3 H)p$ reaction to determine the neutron rate and measures scintillation light generated from decay electrons for the decay rate. Over the past decade, the bottle experiments have dominated the landscape. According to the PDG, six new neutron lifetime results using the bottle method were published in the last 10 years compared to one results using the beam method. One neutron lifetime result with large uncertainties has also been published but is not included in the PDG average. There has also been recent work done using space-based measurements of the neutron lifetime as discussed in 1.5.3, these measurements also have large uncertainties and are not included in the PDG average.

1.5.1 Bottle Storage

All bottle type experiments store extremely low energy neutrons. These UCNs have kinetic energies $\approx$ 100 neV, which corresponds to velocities of $\approx$ 1 m/s. On the earth's surface, UCNs have a gravitational potential energy of roughly 100 neV/m, therefore a UCN can be gravitationally trapped in reasonably sized vessels. The Fermi effective potential of many materials are $>$ 100 neV, so for a carefully chosen material, UCNs can be totally reflected upon interaction with the surface. The magnitude of the neutron magnetic moment is $\approx$ 60 neV/T, so the $\boldsymbol{\mu} \cdot \mathbf{B}$ potential in a large, inhomogeneous magnetic field is sufficient to reflect and trap UCNs. With a clever combination of materials and geometry UCNs can be easily trapped in these "bottles" for 1000s of seconds, longer than the neutron lifetime. Traditionally, UCN bottles used a combination of vertical confinement by gravity and radial confinement using material walls. These interactions with the material walls historically have caused additional neutron losses which lead to large systematic corrections. Some modern experiments have used a combination of gravitational and magnetic traps, however, the magnetic interaction is spin dependent. Because of this, UCNs must be kept in a single

polarization state while in the trapping region to avoid excess losses. These magnetic traps effectively eliminate interactions with materials and thus far these types of experiments have smaller corrections.

To carry out a neutron lifetime experiment using the storage method, an initial number of neutrons, N_0 are loaded into a confinement container. After a known storage time, Δt_1, the remaining neutrons are counted. The process is then repeated with a second storage time, Δt_2, and the remaining number of neutrons are counted again. Assuming that neutron beta decay is the only loss mechanism, the neutron lifetime can then be determined as:

$$\tau_n = \frac{\Delta t_2 - \Delta t_1}{ln(N_1/N_2)}, \tag{1.18}$$

where N_1 and N_2 are the number of remaining neutrons after each holding time. Taking the relative ratio of two measurement cycles allows for many major systematic effects to cancel, simplifying the amount of systematic tests that are needed. In reality, the measured lifetime is a combination of all loss mechanisms of the bottle plus the neutron lifetime. Common loss mechanisms include: inelastic scattering, neutron absorption, and depolarization. Interactions with the wall of the bottle can lead to inelastic scattering that can give the neutron enough energy to the escape the gravitational trap, wall interactions also have some probability for neutron absorption depending of the wall material. In magnetic bottles, field inhomogeneities can cause depolarization which causes the neutron to escape through the magnetic potential. Taking into account these effects the corresponding measured storage lifetime is:

$$\frac{1}{\tau_{storage}} = \frac{1}{\tau_n} + \frac{1}{\tau_{scat}} + \frac{1}{\tau_{abs}} + \frac{1}{\tau_{depol}} + \cdots, \tag{1.19}$$

where each τ corresponds to the particular lifetime of each interaction separately. For many experiments, the difference between $\tau_{storage}$ and τ_n was tens or even > 100 s. These large corrections must be precisely known to have confidence they are applied correctly. The world's most precise measurement of the neutron lifetime is from the UCNτ experiment. This experiment traps neutrons using a magnetic UCN trap which decreases the size of these loss mechanisms. This was the first experiment of its kind to have storage loss corrections less

than the quoted uncertainty for the result [70, 50]. The current world's best measurement using this method is $\tau_n = 877.75 \pm 0.28\,^{+0.22}_{-016}$ s from the UCNτ collaboration [50].

1.5.2 In-Beam Decay

This method measures the neutron decay rate by counting both neutrons and one of the neutron beta decay products, the protons or electrons, using a collimated cold neutron beam. Most of these types of experiments detect the decay proton since it is low energy and much easier to confine with reasonable electric and magnetic fields. These experiments are absolute counting experiments which means that the detection efficiency of both the proton and neutron detector must be accurately known. This method is further complicated because the neutron density in the decay region must be measured, not the neutron number. A neutron is more likely to decay if it has a lower velocity in the decay region, thus, the decay probability is proportional to $1/v$ where v is the velocity of each neutron. In order to avoid an unnecessary systemic effect related to v, the typical neutron detection system for this type of experiment has a detection efficiency that is also proportional to $1/v$. Another complication in this type of experiment is measuring the proton decay volume. The decay rate is proportional to the decay volume, so the neutron beam profile and decay length, L must be accurately known. The neutron lifetime can be calculated as:

$$\tau_n = \frac{L}{v_o}\frac{\dot{N}_n}{\dot{N}_p}\frac{\epsilon_p}{\epsilon_o}, \tag{1.20}$$

where v_o is the thermal neutron reference velocity, $\dot{N}_n$ and $\dot{N}_p$ are the measured neutron and proton event rates and ϵ_o and ϵ_p are neutron and proton the detection efficiencies. The current world's best measurement using this method is $\tau_n = 887.7 \pm 1.2 \pm 1.9$ s from the BL1 collaboration [108]. As this work (BL2) is an experiment of this type, Chapter 2 will cover this method in greater detail.

1.5.3 Other Measurement Techniques

While the beam and storage methods have historically been the most common types of neutron lifetime experiments, in recent years there have been efforts to make systematically independent measurements using other techniques. One of those experiments is currently on going at J-PARC in Japan. It aims to measure the neutron flux and decay rate simultaneously using a time projection chamber. The experiment uses a polarized, pulsed neutron beam in a He and CO_2 gas time projection chamber (TPC). When a neutron decays in the TPC, the decay electron creates an ionization track which may be detected with a multi-wire proportional chamber (MWPC). A -9000 V drift voltage is supplied to the bottom of the TPC so the charge distribution of a particle track may be projected onto the MWPC at the top of the TPC. The gas of the TPC is sensitive to charged particle tracks but not γ-rays, so the background is suppressed. A small admixture of ^{3}He is added to the TPC gas in order to detect neutrons. The neutron flux is determined using the neutron capture process, $^3He(n,p)^3H$. Since this is a two body process, the outgoing proton and hydrogen have fixed energies that can looked for using TPC tracks. The neutron beam is pulsed so that the detection rate has a specific time structure that can be used to reject backgrounds. The pulsed beam also reduces edge effects from the boundaries of the TPC. The current published value using this method is $\tau_n = 898 \pm 10\,^{+15}_{-18}$ s [55]. Thus far, this method has not shown the competitive precision as the other more established methods but further improvements in statistics and systematics are expected. The proposed improvements in reference [55] hope to reduce the systematic uncertainty to ≈ 2 s.

Another novel approach to measuring the neutron lifetime uses space based spectrometers, measuring the neutron flux from planetary bodies. Neutrons are generated from planetary surfaces or atmospheres by spallation when high energy cosmic rays impact the planets. These spallation neutrons are created with energies > 1 MeV but some portion of them are scattered by the surface material or atmosphere of the body. This results in neutrons with energies ranging from 1 eV to 500 keV for epithermal neutrons and < 1 eV for thermalized neutrons. For planetary bodies the size of the moon or larger, thermal neutrons are gravitationally bound with flight times that are on the order of the neutron

lifetime [62]. The feasibility of this technique was demonstrated by a group of scientists using NASA's MESSENGER spacecraft [105] and further refined by the same group using the Lunar Prospector (LP) Neutron Spectrometer [104]. The initial neutron flux from the body's surface is heavily dependent on the body's elemental composition. The first measurement of this type was done using data from flybys of Venus and Mercury. Uncertainty in the composition of the planets was the leading uncertainty in that measurement's precision. However, the Moon's surface is well understood, so using data from LP greatly reduced this uncertainty. The LP's neutron spectrometer consisted of two gas proportional counters filled with ^{3}He, one of these detectors was covered with cadmium to shield it from thermal neutron contributions. The event rate was determined using the difference of the unshielded detector and the Cd covered detector as a method of background subtraction. Background events from the spacecraft itself are significant and must also be subtracted from the data. The background rate and spectral shape were determined during the spacecraft's approach to the Moon, when the spacecraft was at a greater altitude than possible trapped neutron trajectories. The neutron flux is dependent on the altitude of the detectors above the body's surface. At higher altitude it is more likely that a neutron has decayed before reaching the detectors so the neutron flux is lower. Using the elliptical orbit of the spacecraft, the neutron rate can be measured as a function of altitude. When the detector rate is compared to neutron production models of the planet, a neutron lifetime can be calculated. The current most precise measurement of the neutron lifetime using a space based experiment is $\tau_n = 887 \pm 14\,^{+7}_{-3}$ s [104].

1.5.4 Status of the Neutron Lifetime

In 2005, when the BL1 experiment published its value of the neutron lifetime, there was good agreement between all types of neutron lifetime experiments. Later that year, a new storage type measurement was published by Serebrov et al that was in significant disagreement with the accepted value [87]. This caused a reanalysis of other storage type measurements which lead to either withdrawal of the measurement or an added systematic correction that lowered the. In 2010, Pichlmaier et al [77] published a new storage method result that was in agreement with the lower value found by reanalyzed storage measurements.

This was the beginning of the ongoing "neutron lifetime puzzle." Since 2010, multiple storage type measurement have published lifetime values that are significantly lower than the accepted value from 2005. No new data has been published using the in-beam method but a new systematic study was carried out with the BL1 data that significantly decreased the uncertainty of the measurement, but did not find a new significant correction. This leads us to the current day where there is $\approx 4\sigma$ discrepancy between the weighted average of the storage type measurements and the most precise in-beam measurement. The ongoing BL2 experiment aims to address this puzzle by making the first precision measurement of the neutron lifetime using the in-beam method in over a decade as well as searching for previously unaccounted for systematic effects. A summary of the neutron lifetime puzzle can be seen in figure 1.4.

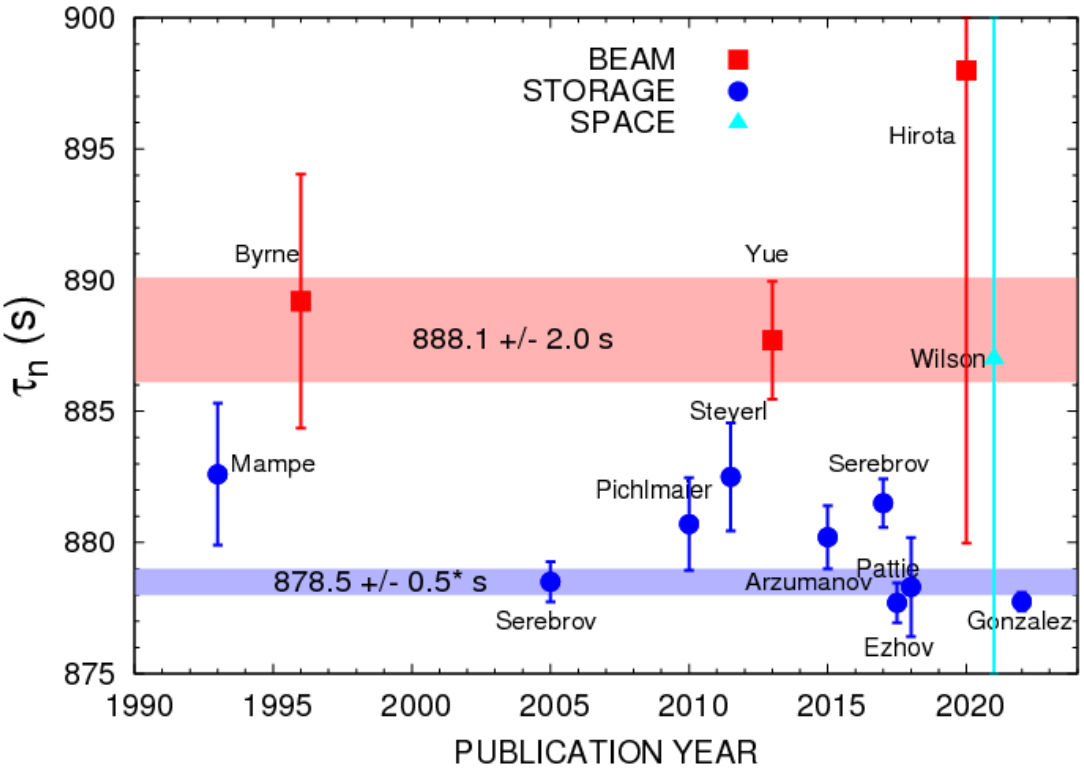

Figure 1.4: Neutron Lifetime vs Year, highlighting the difference between in-beam and storage type measurements. Data include any measurement included in the PDG neutron lifetime average any time between 2018 and 2021. Data also includes the most recent published value from the ongoing TPC measurement at J-PARC and a recent space based measurement. [21, 63, 87, 77, 6, 88, 108, 55, 70, 95, 5, 37, 62, 50]

Chapter 2

Measuring the Neutron Lifetime at NIST Using the In-Beam Method

2.1 Overview and Challenges

The in-beam neutron lifetime technique requires the measurement of three main values. Precision measurements are needed for the proton event rate, the neutron fluence rate, and the trapping volume. Each of these areas has its own unique challenges and technical difficulties. The general difficulties in this measurement technique have been covered previously [22, 21]. For the rest of this paper, with the exception of chapter 3, the techniques discussed will be only those that apply specifically the BL2 neutron lifetime measurement at the National Institute of Standards and Technology (NIST).

An illustration of the experimental setup can be seen in figure 2.1. The experiment consists of a collimated neutron beam, incident from the left in figure 2.1, a superconducting solenoid operating 4.6 T, a solid state silicon charged particle detector, a segmented electrode proton trap and an array of four silicon charged particle detectors surrounding a thin ^{6}LiF deposit. When the neutron beam enters the trapping region, one of two processes can occur. If a neutron decays in the trapping region, the proton is confined radially by the 4.6 T magnetic field and axially by a +800 V (nominal) potential on the upstream (door) and downstream (mirror) sections of the electrode trap. The proton trap is activated for a predefined, finite amount of time before the door electrodes are grounded and the protons

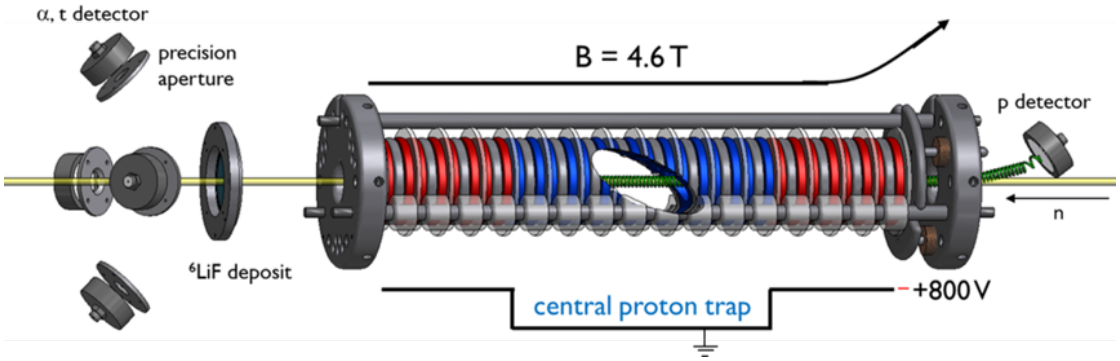

Figure 2.1: An illustration of the BL2 experimental apparatus showing the proton detector, electrode trapping region, and the $1/v$ neutron fluence detectors. The red electrodes on the right side of the trap are the door, and the red electrodes on the left side of the trap are the mirror. The central electrodes in blue are the trapping region.

follow the magnetic field lines and are accelerated to the proton detector. The detected proton rate is given by:

$$\dot{N}_p = \tau_n^{-1} \epsilon_p L \int_A da I(v) \frac{1}{v}, \tag{2.1}$$

where τ_n is the neutron lifetime, L is the length of the trapping region, A is the area of the neutron beam, v is the neutron velocity, $I(v)$ is the neutron velocity dependent fluence rate, and ϵ_p is the detection efficiency of the proton detector. If the neutron does not decay, then it continues until it is incident on a ^{6}LiF deposit where it has a small probability of being captured. If the neutron is captured, the resulting 7Li immediately decays into a triton and and alpha particle. The array of silicon detectors surrounding the deposit then detect these decay products with a known efficiency. If the neutron is not captured, it continues downstream into a beamstop. The detected neutron event rate is given by:

$$\dot{N}_{\alpha+t} = \epsilon_0 v_0 \int_A da I(v) \frac{1}{v}, \tag{2.2}$$

where ϵ_0 is the neutron detection efficiency and, following a usual convention in neutron physics, v_0 is the thermal neutron velocity ($v_0 = 2200$ m/s) for which the neutron detection efficiency is defined. The integrals of the previous equations are identical, given the assumptions that the neutron velocities do not change between the trapping region and the neutron detector, and the neutron detection efficiency is exactly proportional to 1/v. Relating equations 2.1 and 2.2 we have the neutron lifetime given as:

$$\tau_n = \frac{L}{\dot{N}_p} \frac{\dot{N}_{\alpha+t}}{\epsilon_0} \frac{\epsilon_p}{v_0}. \tag{2.3}$$

There are three major challenges about this type of neutron lifetime measurement: 1) the relatively long neutron lifetime means that decay rate and subsequent proton rate is low with respect to background rates; 2) the trapping potential of the decay volume must be accurately measured; 3) the dependency of the decay rate on the neutron velocity means that the density of neutrons in the decay volume is needed and not the neutron number. Additionally, significant care must be taken to understand the detection efficiency of the proton and neutron detectors.

2.2 Experimental Method and Apparatus

2.2.1 Proton Counting

The absolute proton rate is difficult to measure for a multitude of reasons, including the low signal to background rate due to the relatively long lifetime of the neutron, and the very low decay proton energy. In order to decrease the rate of random background events, protons are not allowed to travel freely to the proton detector as soon as they are born. Instead, decay protons are trapped for a finite amount of time before being released and sent to the detector. Because of the periodic release of the protons, the protons may only arrive at the detector in a finite time window, which produces a significant background reduction. This trapping technique was first proposed in the late 1980s and has been used successfully in other experiments in the past [19, 67]. The energy of the decay protons is another reason the proton rate is difficult to determine. The maximum kinetic energy the decay protons can have is 751 eV, which is far too low for solid state silicon detectors to detect. In order for the protons to have enough energy to be detected, they are accelerated with an electric potential between -25 kV and -35 kV. The proton detectors used are commercially available silicon semiconductor charged particle detectors. These detectors have low noise, low leakage current, and thin deadlayers. Two detector types are used, a Passivated Implanted Planar Silicon (PIPS) detector, which has a SiO_2 deadlayer, and a depleted silicon surface barrier (SB) with a gold deadlayer. These detectors are radiatively cooled to reduce noise and have high detection efficiencies for protons with energies 20 keV or higher.

2.2.2 Proton Trap

Ideally, the proton trapping region would consist of a perfectly uniform magnetic field and a perfect square well electric potential high enough to completely trap all energies of decay protons. If this were the case, the length of the trapping region, L, would be perfectly well defined and all protons born in the trapping region would be trapped with 100 % efficiency. However, a perfect square well potential is not physically possible, therefore L is not easily defined. Because of the shape of the electric potential, there is a region adjacent to the door

and mirror where the potential is between the nominal voltage and ground. This section is call the "end region," and decay protons are not trapped with 100 % efficiency in that region. In the end region, the electrostatic potential is such that it is above ground, but not high enough to trap all energy decay protons. For this reason, the proton trap is segmented, and the trapping length is varied during the data taking. Because the individual electrodes are carefully manufactured and assembled, the end region, L_{end}, for each trapping length is nominally the same. This makes the proton trapping length, L, easier to determine as only the difference in trapping length between two or more trap lengths is needed to determine the neutron lifetime. Using the segmented electrode trap the neutron lifetime relation from equation 2.3 becomes:

$$\frac{\dot{N}_p}{\dot{N}_{\alpha+t}} = \tau_n^{-1} \left(\frac{\epsilon_p}{\epsilon_o \nu_o} \right) (nl + L_{end}), \tag{2.4}$$

where l is the length of a single electrode, n is the number of electrodes and L_{end} is unknown. It can be seen from the previous equation that when $\dot{N}_p/\dot{N}_{\alpha+t}$ is fit as a function of the trap length, the lifetime is proportional to the slope of that fit and L_{end} is proportional to the intercept of the line and not needed to measure the neutron lifetime.

The BL2 experiment has two proton traps available for use. The "Mark II" trap is the same trap that was used in the BL1 experiment and has 16 electrodes. The "Mark III," which was built specifically for the BL2 experiment and will be detailed below, has 12 electrodes. The conducting segments of each electrode trap were manufactured from fused quartz and coated with a thin conducting layer of gold, spacer pieces for the Mark II trap were also made from fused quartz but left uncoated. The trap is assembled and measured at room temperature using a coordinate measuring machine. The dimensions were measured to a precision of $\pm 5\,\mu$m. Fused quartz is used because the thermal contraction between room temperature and 4 K is small. Changes in the measured dimensions when at equilibrium in the cold magnet bore are approximately 0.01% [100]. The Mark II trap has electrodes that are nominally 18.6 mm in length and spacers that are 3 mm in length. The total length of the Mark II trap electrodes is 341.6 mm, with a maximum trapping length of approximately 216 mm. As can be seen in figure 2.2, there is significant amount of hardware necessary for

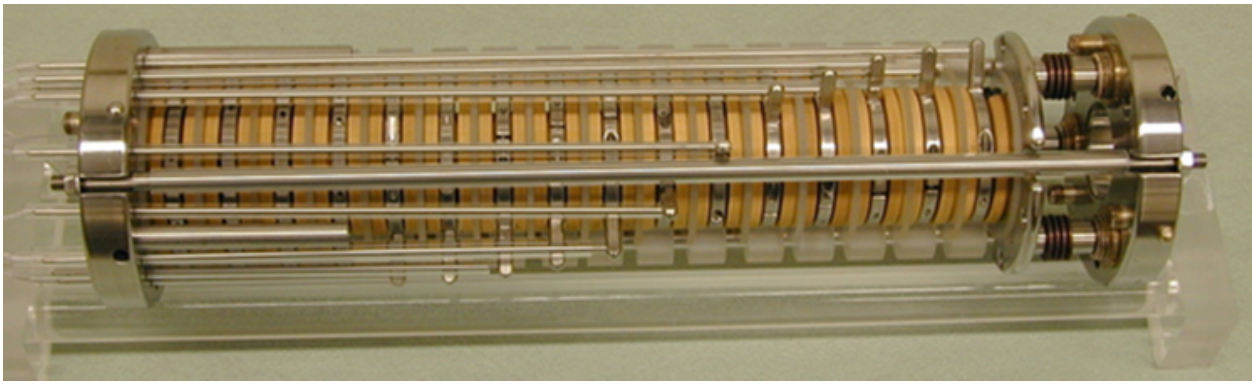

Figure 2.2: Photo of the Mark II trap before being placed in the magnet bore.

holding the electrodes and spaces together on the upstream side of the Mark II trap assembly that reduces the possible trapping length.

2.2.3 Mark III Proton Trap

Mark III Proton Trap Design

Currently all of the data taking for BL2 has been done with the Mark II electrode trap. The Mark II trap has 16 different electrodes, 3 of which are used for both the door and mirror which leaves up to 10 electrodes used for the trapping region. Specifics regarding the Mark II trap have been detailed elsewhere [67]. In January 2021, the decision was made that all the systematic tests that could be reasonably accomplished with the Mark II proton trap had been done and it was time to transition to make a new independent measurement of the neutron lifetime in the most optimized configuration. The Mark III proton trap was designed as an incremental improvement over the Mark II proton trap. There were two major design changes, the first was the trapping electrodes in the Mark III trap are separated by a single quartz sphere instead of quartz spacer disks. This has three advantages, two of which should improve the vacuum inside of the trapping region. Since there is open space between the faces of the trapping electrodes, any residual gas inside the trapping region now has a semi-direct path to the ultra-cold inner wall of the 4 K magnet bore. The second benefit of this trap design is there are now fewer places where virtual leaks can occur. The previous trap design of many disks pressed together had the potential for virtual leaks that could occur into the trapping region. Both of these design benefits should decrease the likelihood for any variations in the local vacuum conditions of the trapping region. The third benefit of the quartz sphere is that it makes the dimensions of the Mark III trap much easier to measure with the coordinate measuring machine. The second design change was lowering the number of trapping electrodes from 16 to 12. The length of the trapping electrodes was also increased slightly so that only two electrodes will be used for the door and mirror regions instead of three. This allows data to be taken at the same number of unique trapping lengths but shifts the entire trapping region slightly upstream. Moving the trapping region slightly upstream is beneficial because the magnetic field uniformity is worse in the downstream region. The

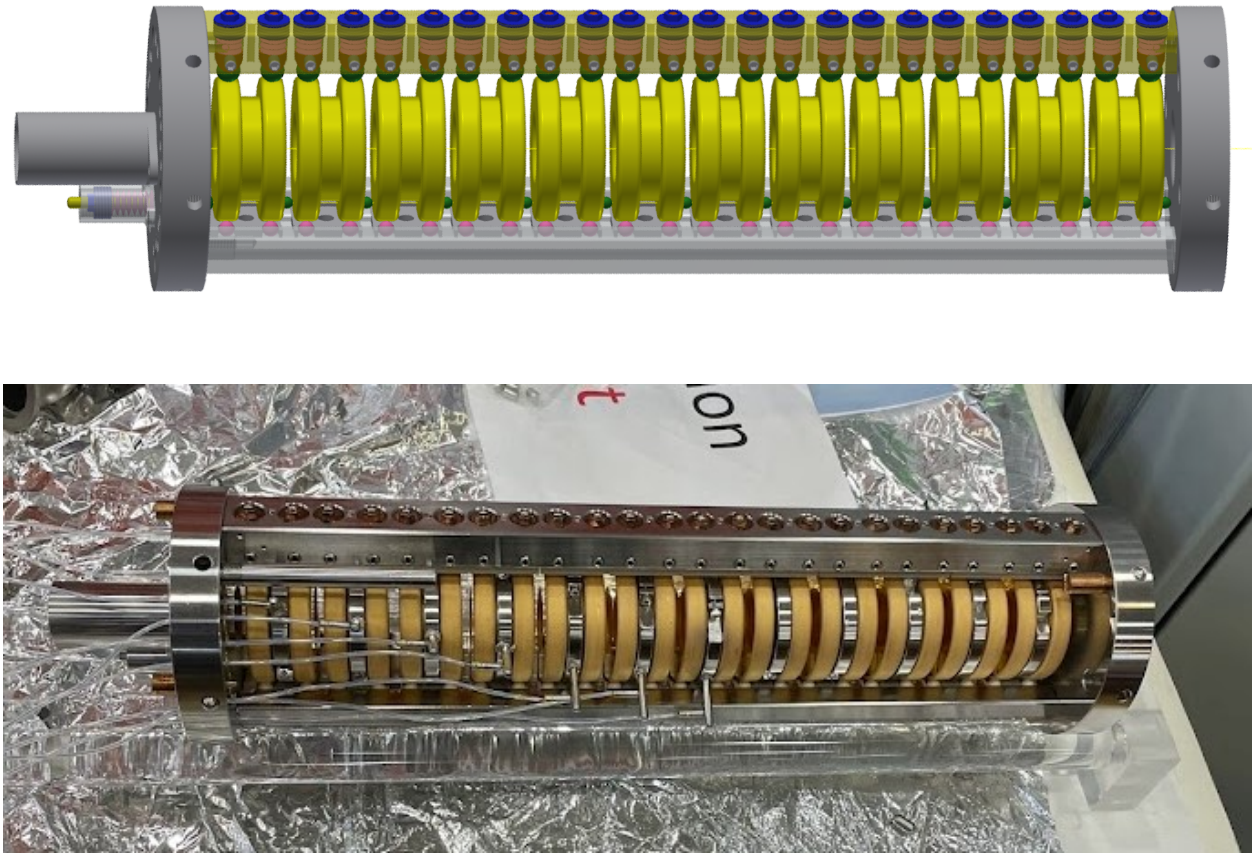

Figure 2.3: The top figure shows an assembly of the Mark III trap design where the separating quartz spheres can be seen in pink and green. The bottom figure shows a photo of the Mark III just prior to being installed in the magnet bore with all electrical connectors attached.

Mark III proton trap will allow data to be taken at seven unique trapping lengths while decreasing the magnetic field non-uniformity correction to the neutron lifetime. The Mark III trap has electrodes that are nominally 26.6 mm in length and gaps that are 4.8 mm in length. The total length of the Mark III trap electrodes is 372 mm, with a maximum trapping length of approximately 251.2 mm. A drawing and picture of the Mark III trap can be seen in figure 2.3

Mark III Proton Trap Installation and Alignment

To ensure the transport of all trapped protons to the detector, the proton trap must be aligned to better than a millimeter with respect to the neutron beam center. To do this, crosshairs are placed in the upstream and downstream ports of the trap, a theodolite is then used to check the alignment with various beam markers around the apparatus. The Mark III trap is first inserted into the magnet bore with the cross hairs in the upstream position. Using a theodolite, the upstream crosshairs are compared to beam center. Both ends of the trap have 3 "feet" that can be adjusted using setscrews that hold it in place in the bore. The feet on the upstream section of the trap are adjusted so that the crosshairs align with beam center to better than $0.5\,mm$. The downstream crosshairs is then placed in the trap and the same procedure is followed. The axial position of the trap must be accurately known in order to make the magnetic field nonuniformity correction. Since there are no hard stops inside the magnet bore, a small block, called the "trap positioning piece," was designed to accurately and repeatably position the trap. It is not required that the trap be in a specific location, only that the location of the trap is accurately known. For the Mark III trap, the trap needed to be positioned so that the downstream edge of the trap frame is approximately 1" from the downstream end of the magnet bore. To do this, an aluminium block was machined so that it could be placed against one of the convenient flat surfaces around the magnet bore and extend 1" into the magnet bore. The back plate of the Mark III trap could then be slid into place against the block for consistent and repeatable positioning, see figure 2.4 for a picture of the Mark III being positioned using this piece. After the alignment of the upstream crosshairs is verified, a single foot on each end is loosened, the trap is pulled out and the upstream crosshairs are removed. The trap is then reinserted into the bore using

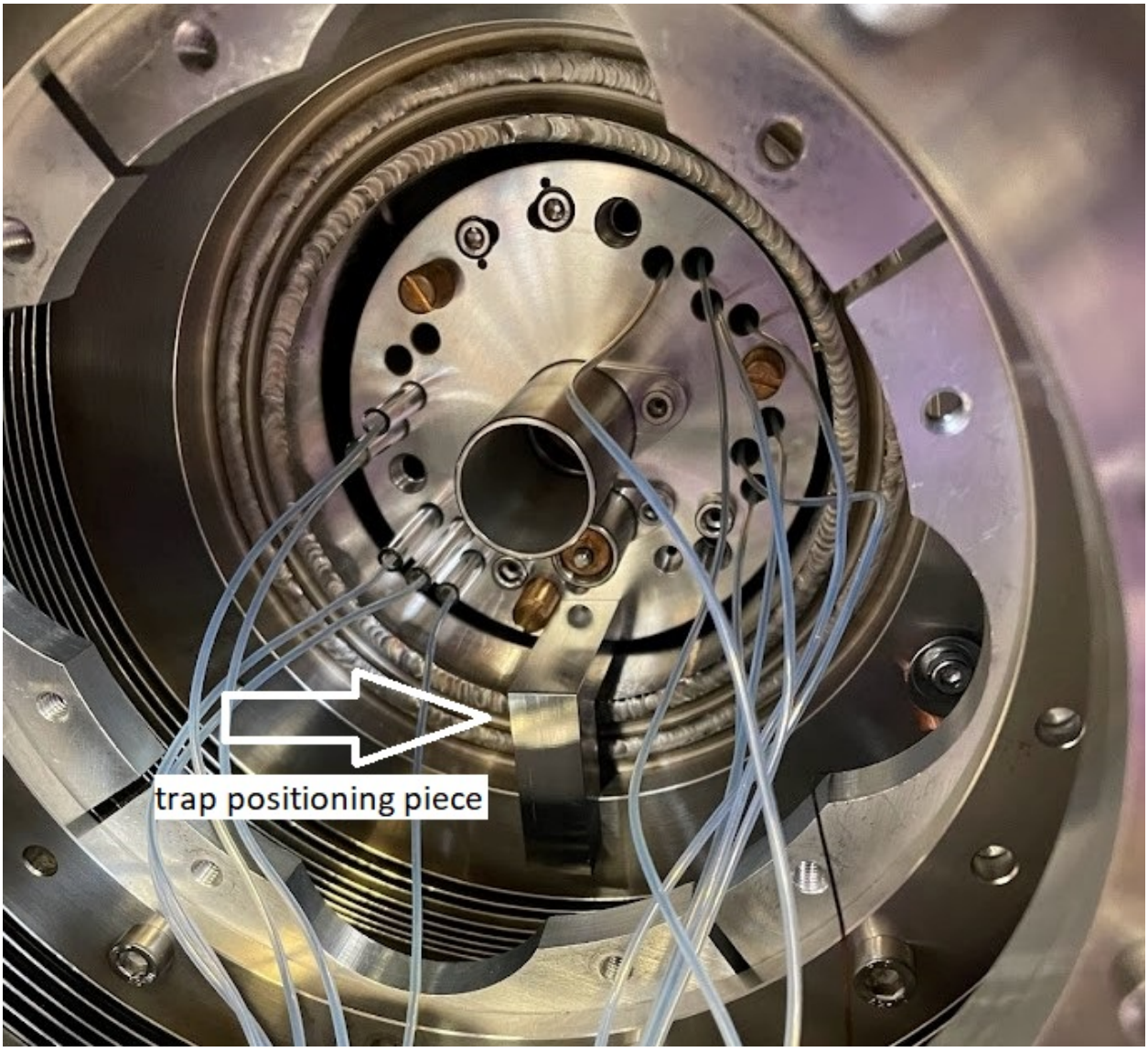

Figure 2.4: Photo of downstream end of the Mark III trap in the magnet bore with the trap positioning piece in place.

the trap positioning piece and the feet are re-tightened. The accessible downstream section is once more checked with the crosshairs before closing the magnet bore vacuum.

2.2.4 Neutron Counting

In addition to counting the absolute number of trapped protons, the absolute neutron fluence must also be determined. The density of neutrons in the trapping region is determined by measuring the decays from the $^6Li(n,t)^4He$ reaction. The total product count rate depends on the neutron fluence, the solid angle of the detector array, the neutron capture cross section, and the deposit areal density. The detector set up consists of an array of four silicon charged particle detectors. These detectors are arranged in such a way that the total solid angle of all four detectors is not sensitive to small movements in the beam position. A schematic of the detectors can be seen in figure 2.5, and a contour plot of the solid angle dependence on beam position can be seen in figure 2.6. A detector's solid angle is defined by a precision machined aperture that is slightly smaller than the detector active area so that detector edge effects can be neglected. The tritons and the alphas from the ^7Li decay have energies 2.72 MeV and 2.07 MeV, respectively, so they are easily detected by the silicon detectors without the need for additional acceleration potentials. The target consists of a thin single crystal silicon wafer with an evaporated deposit of ^6LiF. The deposit is made thin enough so that the neutron beam attenuation and the energy loss of the tritons and alphas are negligible. ^6Li has a neutron cross section that is known to 0.3 % from the evaluated nuclear data files [17]. For cold neutrons the energy dependence is well known and follows closely to a pure $1/v$ curve. This allows for a handy cancellation of neutron wavelength dependent affects throughout the experiment. The absorption of neutrons in the ^6LiF deposit is sensitive to the neutron wavelength distribution and deposit areal density. In BL1, this caused the largest correction to the neutron lifetime [67]. BL2 has remeasured the neutron wavelength distribution and plans to take data with multiple ^6LiF deposit thicknesses, it is expected that this correction will be cut in half. Determining the neutron fluence monitor efficiency, ϵ_0, is a critical part of the experiment and was the largest source of uncertainty in BL1 the experiment. Figure 2.1 shows the final corrections and uncertainties for the BL1 experiment.

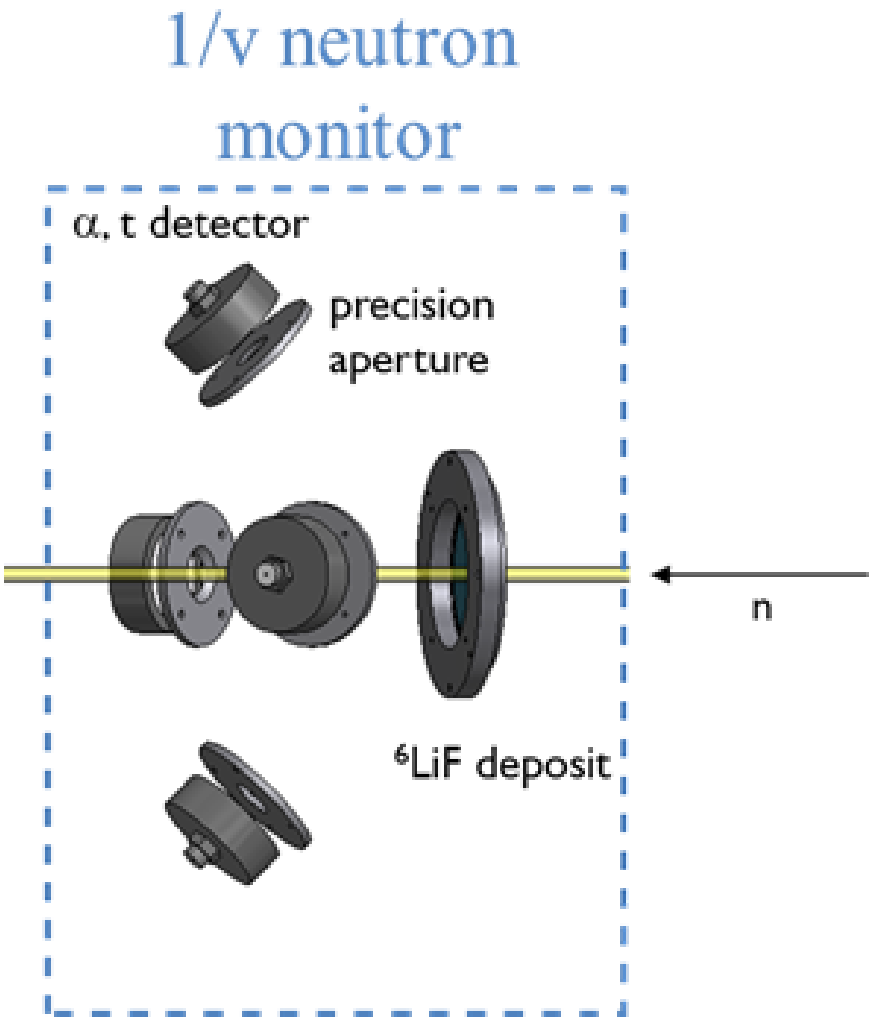

Figure 2.5: A schematic of the $1/v$ neutron fluence monitor showing the ^6Li deposit and surrounding detectors.

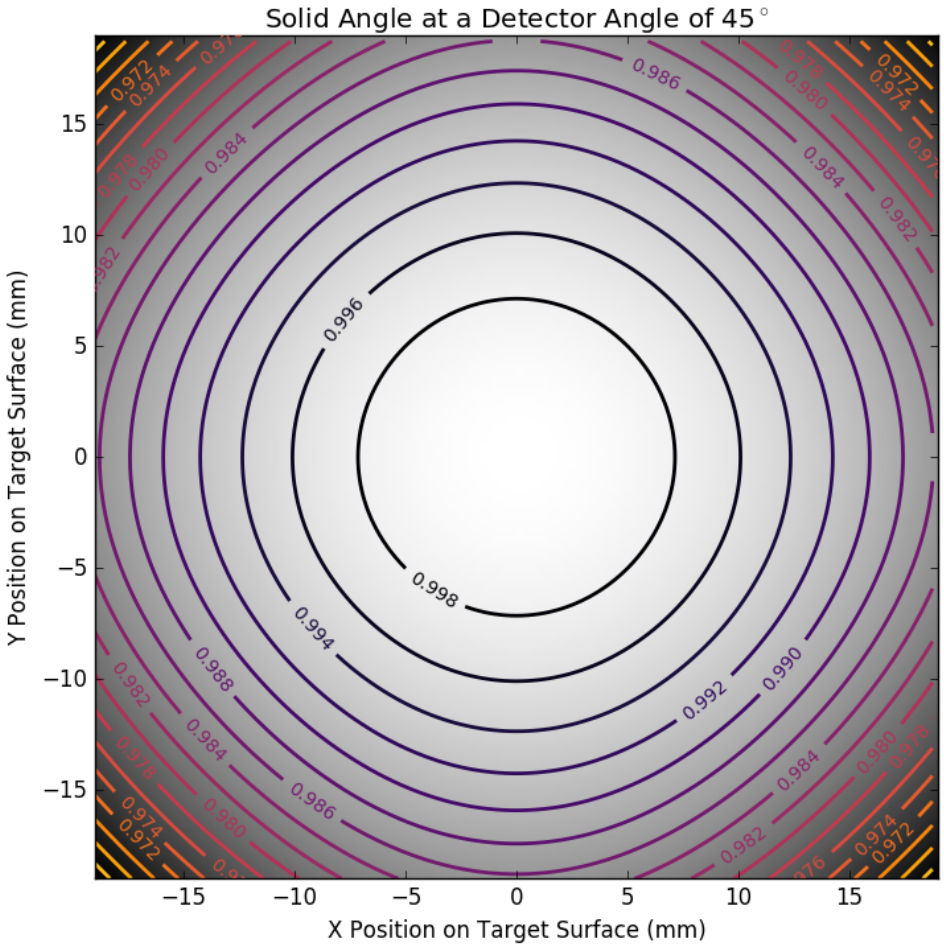

Figure 2.6: Contour plot of the relative change in solid angle subtended by the four precision apertures in the 1/v neutron fluence monitor taken from reference [3].

Table 2.1: Final Corrections and uncertainties for the BL1 experiment, taken from reference [67].

Source of Correction	Correction (s)	Uncertainty (s)
^{6}LiF deposit areal density		2.2
^{6}Li cross section		1.2
Neutron detector solid angle		1.0
Absorption of neutrons by ^{6}Li	+5.4	0.8
Neutron beam profile and detector solid angle	+1.3	0.1
Neutron beam profile and ^{6}Li deposit shape	−1.7	0.1
Neutron beam halo	−1.0	1.0
Absorption of neutrons by Si substrate	+1.3	0.1
Scattering of neutrons by Si substrate	−0.2	0.5
Trap nonlinearity	−5.3	0.8
Proton backscatter calculation		0.4
Neutron counting dead time	+0.1	0.1
Proton counting statistics		1.2
Neutron counting statistics		0.1
Total	−0.1	3.4

One can note the the total uncertainty due to statistics was 1.2 s, the uncertainty due to systematics was 3.2 s, and the uncertainty associated with ϵ_0 was 2.7 s.

Improving this determination and decreasing the uncertainty associated with it was a crucial factor in the viability of BL2. In BL1, ϵ_0 was defined as:

$$\epsilon_0 = \frac{\sigma_0}{4\pi} \int \int \Omega(x,y)\rho(x,y)\phi(x,y)dxdy, \tag{2.5}$$

where σ_0 is the ^6Li neutron capture cross section at thermal neutron velocity ($v_0 = 2200\,m/s$), $\Omega(x,y)$ is the neutron flux monitor detector solid angle, $\rho(x,y)$ is the areal mass density distribution of the ^6Li deposit, and $\phi(x,y)$ is the areal density of the neutron beam at the deposit location. The detector array solid angle was measured in two ways. First, a coordinate measuring machine measured the precision aperture diameters and the distance to the center of the deposit. Second, a calibrated alpha source was placed in the array and the rate was measured in all four detectors. The solid angle was then calculated as the measured rate divided by the total rate of the calibrated source. These two measurements agreed to better than 0.1 % and had an uncertainty of 0.1%. The ^6LiF deposits were specially made for the experiment by the Institute of Reference Materials and Measurements in Belgium, by evaporation onto a set of rotating silicon wafers. For a detailed description of the process see references [72][73]. The areal densities of the deposits were determined using a thermal neutron beam, and the mass was determined using isotope dilution mass spectroscopy. The areal mass density was determined to 0.25 %. The determination of the areal mass density was the single largest uncertainty in the BL1 experiment, accounting for 2.2 s of the total 3.2 s systematic uncertainty in the final result. In order to circumvent the necessity to measure the constituent parts of ϵ_0, a device called "Alpha-Gamma" was created to independently calibrate the neutron flux monitor [46]. Using Alpha-Gamma a new calibration of the neutron flux monitor was determined with an uncertainly of 0.5 s, a factor of five improvement over the previous determination, this was the subject of a previous publication and UT Ph.D. thesis [108, 107]. A detailed description of the ongoing use of the Alpha-Gamma device can be found in chapter 5. Decreasing the neutron flux monitor calibration to an 0.5 s

uncertainty made it no longer the leading systematic uncertainly from the previous result and prompted the proposal of the BL2 experiment.

2.2.5 Proton Trapping Cycle

The proton trapping cycle has three distinct configurations: trapping mode, counting mode, and flushing mode. The trap spends the vast majority of its time in trapping mode. In this mode, the door and the mirror electrodes are both kept at +800 V (nom.) and the central trapping electrodes are grounded. In this mode, any proton born in the central region is trapped with 100% efficiency. After a nominal trapping time, the trap then is switched to counting mode. In counting mode, the door electrodes are grounded and a small gradient potential is placed on the central trapping electrodes while the mirror remains at +800 V. The small gradient potential, called the "ramp", forces protons that have low axial kinetic energies to exit the trap. If the ramp was not applied, protons with low axial kinetic energy could spend an indefinite amount of time in the trapping region and never reach the proton detector. High axial kinetic energy protons arrive at the proton detector almost immediately. Therefore there is some spread in the length of time it takes for protons of different energies to arrive at the proton detector. The larger the ramp potential, the smaller this time difference becomes. All protons that leave the trapping region adiabatically follow the magnetic field lines to the proton detector. The field includes a 9.5° bend in the magnetic field lines so the proton detector can be offset from the neutron beam. Anytime there is a change in the trapping configuration the DAQ sends a signal to three switcher modules that very quickly change the voltage on each trapping electrode. These switcher modules are two voltage output modules with the capability to switch between the voltages in $\approx 10\,ns$. When counting mode is started, the DAQ begins digitizing the detector signal. This allows for the suppression of background events because the detector only needs to be active when trapped protons are able to hit the detector. Depending on the trapping time, this suppression factor is between 15 and 500. The detector is activated $47.6\mu s$ before counting mode is started.

Counting mode is active for $76\,\mu s$, long enough for all protons to leave the trap even with a minimal ramp potential. $123.6\,\mu s$ after the detector is activated flushing mode begins. In flushing mode, the door and the mirror electrodes have a small, -0.5 V, negative potential

applied to them and the central trapping electrodes are grounded. This prevents other changed particles, namely electrons, from being trapped in the door and mirror regions during the trapping and counting cycle and improves trap stability. After another $30\,\mu s$, ($153.6\,\mu s$ after detector activation), flushing mode ends and the whole trapping cycle begins again. The detector is active for a total of $204.8\,\mu s$ per trapping cycle. For the first $47.6\,\mu s$ and last $51.2\,\mu s$ of the detector activation the trap is in the trapping configuration with the door and the mirror at + 800 V (nom.). This means there is $106\,\mu s$ of fixed time when the manipulations occur in each trapping cycle. A full trapping cycle is actually the nominal trapping time (e.g. 10 ms) plus $200\,\mu s$. This means that the trapping mode for any trapping cycle is the nominal trapping time plus $94\,\mu s$. If we take a 10 ms trap time for example, that means trapping mode is activated for $10,094\,\mu s$ and neutrons are being counting for $10,200\,\mu s$. The difference in these two numbers must be added as a correction to the $\dot{N}_p/\dot{N}_{\alpha+t}$ ratio and this ratio changes for different trapping times. In BL1, only trapping times of 5 ms and 10 ms were achieved. The vast majority of data was taken at 10 ms as the apparatus was highly unstable at longer trapping times. In BL2, stable proton trapping has now been achieved over a much broader range and data has been taken between 3 and 100 ms. This means the neutron to proton counting time difference ranges between a 0.1% and a 3.4% correction to the proton rate but this correction is precisely known. Shorter or longer trapping time have advantages and disadvantages. The shorter the trapping time the less likely it is that multiple trapped protons are in the trap for any given trap cycle. This decreases the multiple proton correction, but it also increases the amount of background that needs to be subtracted. The longer the trap time, the more likely it is to have to multiple trapped protons leading to a larger multiple proton correction but leads to a smaller background subtraction. The ability to take data at multiple trapping times allows for a check of the analysis background subtraction and multiple proton correction as well.

Chapter 3

Experimental Improvements to the In-Beam Measurement Technique

The BL2 experiment includes many of the same apparatus components of the original BL1 experiment but with additional upgrades made. The same 5 T superconducting solenoidal magnet, 1/v neutron fluence monitor, and quasi-Penning electrostatic proton trap are used, however the apparatus is located on the new, high flux NG-C beamline [89] and upgrades have been made to other areas of the experiment. These include: better optimized proton transport, better signal to background and signal to noise ratios, improved neutron flux calibration, better energy and timing resolution using an improved preamp and modernized analysis techniques. In the sections below I will outline the upgrades made to the apparatus in detail.

3.1 Absolute Neutron Fluence Calibration

The neutron fluence monitor that is used in the BL2 experiment uses the same hardware as the BL1 experiment, but the way in which the neutron detection efficiency is determined is significantly improved. Previously, in BL1, the determination of the neutron counting efficiency, ϵ_0, was the largest single uncertainty in the neutron lifetime. The total combined uncertainty associated with ϵ_0 was $\approx 2.7\,s$. Each contribution to ϵ_0 in equation 2.5 was individually measured so the uncertainties of those measurements are compounded in the

final result. Another issue with this determination is that it uses the input of the ^6Li neutron capture cross section. This relies on other measurements for extrapolation of the cross section to cold neutron energies because there is little data in this energy regime. This method also potentially requires ϵ_0 to be updated periodically as new measurements of the neutron capture cross section are made. As a result, a device was developed that was designed and built to directly calibrate the neutron flux monitor without respect to the lithium cross section and relies significantly less on the physical shape of the ^6Li deposit and neutron beam. This device reduced the uncertainly of ϵ_0 by a factor of 5. A detailed description of this device, called Alpha-Gamma, may be read in chapter 5. Another improvement from BL1, is that BL2 plans to take the majority of its production data with a thinner ^6Li deposit. The neutron capture cross section in the energy regime used in this experiment is far away from any resonances so it is nearly $1/v$ in the limit that the capture material is very thin. Using a thinner ^6Li deposit leads to a smaller correction due to the deviation of neutron absorption from the $1/v$ law.

3.2 Magnetic Field Non-Uniformity

In BL1, the largest correction to the lifetime was caused by the non-uniformity of the magnetic field in the proton trapping region. Each decay proton is born with a specific electrostatic and magnetic pseudo-potential. A proton is trapped if its kinetic energy plus its total potential energy is less than the maximum trapping potential (nominally 800 V). The magnetic pseudo-potential decreases when magnitude of the field decreases, changing the potential of the end region of the trapping region. If a proton is born at a position of higher magnetic field and the door/mirror is placed in a region of lower magnetic field, the trapping probability decreases. This is analogous to a magnetic mirror, but with the opposite effect. For a more detailed description of non-uniformity of the magnetic field see reference [67]. Because of the magnetic field non-uniformity in the trapping region, the trapping probability is slightly different at each trapping length and requires a correction. A large portion of the data in BL1 was taken at the maximum trap length, 10 electrodes. It was determined after the fact that the drop off in the magnetic field in this region was larger

than anticipated, leading to a large correction to the neutron lifetime. BL2 improves on this in two ways. First, when using the Mark II trap, lifetime data is no longer taken with 10 electrodes. Second, the Mark III trap was designed so that the proton trapping region avoids this area of non-uniformity. The Mark III trap has been installed as discussed in section 2.2, and it is planned for the majority of production lifetime data to be taken with this trap.

3.3 Neutron Flux and Collimation

In order to achieve the precision goals of this experiment more than 99.9% of trapped protons must be transported to the detector active area. Therefore, the largest extent of the neutron beam in the trapping region must be sufficiently small such that the protons following the magnetic field lines to the detector fall inside the active region of the detector. Extensive neutron transport and collimation simulations were done so that these requirements are met. In BL1, beam images were taken at several places along the neutron beam to verify the extent of the beam. Previously, dysprosium foils were used as the imaging method, neutrons capture on the Dy foil causing it to become activated. The activated foil is then placed on a film that can be read with an image reader, and beta decay electrons from the Dy foil expose the image film. It was estimated that the uncertainty in the image reader was 0.5 mm [67]. In the years since these beam images were taken, the group's understanding of this imaging method has improved. It is now believed that the bleeding or smearing out of the image film was underestimated in BL1, and the neutron beam extent was not as large as previously believed. With modern neutron imaging technology such as a neutron camera, beam imaging can be more accurately done in BL2 and there will be no such worry about the extent of the neutron beam spot. To give further confidence in the proton transport efficiency to the detector active area, two detector sizes, $300\,mm^2$ and $600\,mm^2$, have been used. This allows for a comparison between the proton rates with two detector sizes, if the detector is not well aligned then the proton rate will increase with the $600\,mm^2$ detector because it is less sensitive to alignment. It is planned for most production lifetime data to be taken with a $600\,mm^2$ detector. With better imaging technology and the larger detector

size, the correction for protons missing the active region of the detector will be negligible in BL2.

3.4 Cold Bore Isolation

One of the major questions about the in-beam method is losses out of the proton trap. In BL1, data was taken almost exclusively at 10 ms trapping time because of stability issues with the apparatus. In general, when attempting to take data at any other trapping time, the detector would be bombarded with high energy pulses that corresponded in time to the voltage manipulations of the trap electrodes. This meant that no trap loss systematic test could be done by changing the trapping time and comparing the lifetime values. In BL2, with improved detector and electronic isolation, data was taken at trapping times ranging from 3 to 20 ms. However, when taking data at 30 ms the same behavior was observed where the detector would be overwhelmed by high energy pulses and kill the detector. It was hypothesized that the coupling between the 4 K bore of the magnet and the warm vacuum sections could be the cause of this instability. To isolate the cold bore vacuum section from the rest of the apparatus, two thin perfect crystal Si window mounts were designed. These mounts were placed at the closest possible point to the bore itself with the idea being this would decrease the pressure in the bore and produce a more stable trap. The mounts were made out of windowed gate values where the typical glass window was replaced with a very thin Si wafer to minimize neutron scattering. Installing the windows in gate valves allowed the windows to be opened or closed in situ to test repeatability. The Si window upstream of the magnet has a diameter of 23 mm and a thickness of 160 μm; the Si window downstream of the magnet has a diameter of 44 mm and a thickness of 200 μm. It was immediately seen that the vacuum quality was better in the proton vacuum region with the windows in place. With the windows installed data has been taken between 3 and 100 ms without a single incident of instability. 100 ms is approximately the longest trapping time that is reasonable for data taking because of the pile up associated with multiple protons in the trap. It was also demonstrated that the instability returns when the windows are in their open position. These new windows give BL2 the ability to take data over a wide range of trapping times

and will allow for previously inaccessible systemic tests of trap losses to be done. A detailed discussion of the findings of these systematic tests can be found in section 6.5.

3.5 Data Stream Digitization

In BL1, the proton data stream was a single channel from a single detector. The raw preamp pulse was sent through a spectroscopy amplifier (specamp) so that the output pulse of a proton signal was Gaussian. This was turned into list mode data where the maximum energy and the time bin of the maximum energy was recorded, but the waveform was not digitized. This limited the ability to tailor the analysis to specific systemic tests or monitor data quality checks such as noise stability. In BL2, there are two proton data stream channels, still from a single detector. The raw preamp waveform as well as the specamp signal are now digitized with the use of a GaGe card digitizer [42]. This digitization allows for a more modernized analysis approach. The raw preamp waveforms may be analyzed with a variety of different filters that can be tailored to specific goals, for example, energy resolution or precise timing information. The specific utilization of the new analysis methods will be discussed in section 4.3.

Chapter 4

Analysis Techniques

These sections will detail the analysis methods used to determine the neutron and proton rates and discuss analysis techniques new to BL2. The optimization and benchmarking of these new techniques will be discussed as well as the advantages of these techniques over previously used methods. How the neutron lifetime is determined using these analysis methods will also be discussed.

4.1 Determination of the Neutron Rate

The neutron lifetime is a function of the ratio of the proton and neutron rates. In addition to the proton rate, described below, one must simultaneously determine the neutron density in the trapping volume. The total neutron-induced event rate depends on the neutron fluence, the total solid angle of the four detectors, the areal density of the ^6LiF foil, and the neutron capture cross section. The absolute number density of neutrons in the trapping volume is determined by measuring the products of the neutron capture reaction $^6Li(n,t)^4He$ with four solid state silicon detectors. The total rate of the measured reaction products is proportional to the total fluence of neutrons, not the total number. At cold neutron energies ($\lambda_n \approx 3\,\text{Å}$), the neutron capture cross section of ^6Li is energy independent to better than 0.01 % [11]. Therefore, just like for the proton trap, the probability of an event is proportional to $1/v$. The detector array consists of four solid state silicon detectors that are positioned in such a way that the solid angle subtended by the detectors is insensitive to any change in the source

position to first order [79, 30]. The detector array can be seen in figure 2.5 and the contour plot of the total solid angle can be seen in figure 2.6. The solid angle of the four detectors is precisely defined by precision-machined apertures placed directly in front of the detectors. The reaction products of the neutron capture reaction have energies of 2-3 MeV, making them easily detectable and well separated from the noise. In BL1, it was necessary for the neutron counting efficiency, ϵ_0, to be calculated. Included in this calculation is the neutron capture cross section. In addition to introducing extra uncertainty into the calculation, this also introduces the possibility that the final determination of the neutron counting efficiency may need to be updated as new measurements of the cross section are made. Instead, we are now able to measure the neutron counting efficiency directly without reference to the neutron capture cross section using Alpha-Gamma, which will be discussed in chapter 5.

The ^6Li targets consist of a thin wafer ($\approx 400\,\mu m$) of single crystal silicon with an evaporated coating of ^6LiF. These targets were made with three different areal densities of ^6Li, nominally 20, 30, and 40 $\mu g/cm^2$ [72, 73]. Data have been taken with two 40 $\mu g/cm^2$ deposits and is planned to be taken with a 30 $\mu g/cm^2$ deposit. These deposits are thin enough that the neutron fluence is only slightly attenuated, and the reaction products do not have significant energy loss getting out of the deposit. It is planned that data will be taken with the two different thicknesses so that the deviation from a perfect $1/v$ dependence can be independently measured.

The signals from the four detectors are sent through a single body CAEN 4-channel preamplifier. From there the signals are sent to four individual NIM spectroscopy amplifiers. Because the energy difference of the reaction products is large compared to the detector noise, the two particle peaks are well separated from each other and from the noise. Because the peaks are well separated and easily identifiable, no waveform analysis is necessary. Each shaped signal is sent to a dual window single channel analyzer (SCA). The dual window SCAs allow thresholds to be set for both the low and high side of two separate windows. This allows for four individual thresholds to be set for each detector; a total of 16 thresholds overall. Each SCA counts any pulse that is above the energy threshold, therefore four tallies are sent to DAQ per detector for every run, we will label these thresholds as 1-4, in increasing energy. The thresholds are carefully set so that the difference between the count rates of

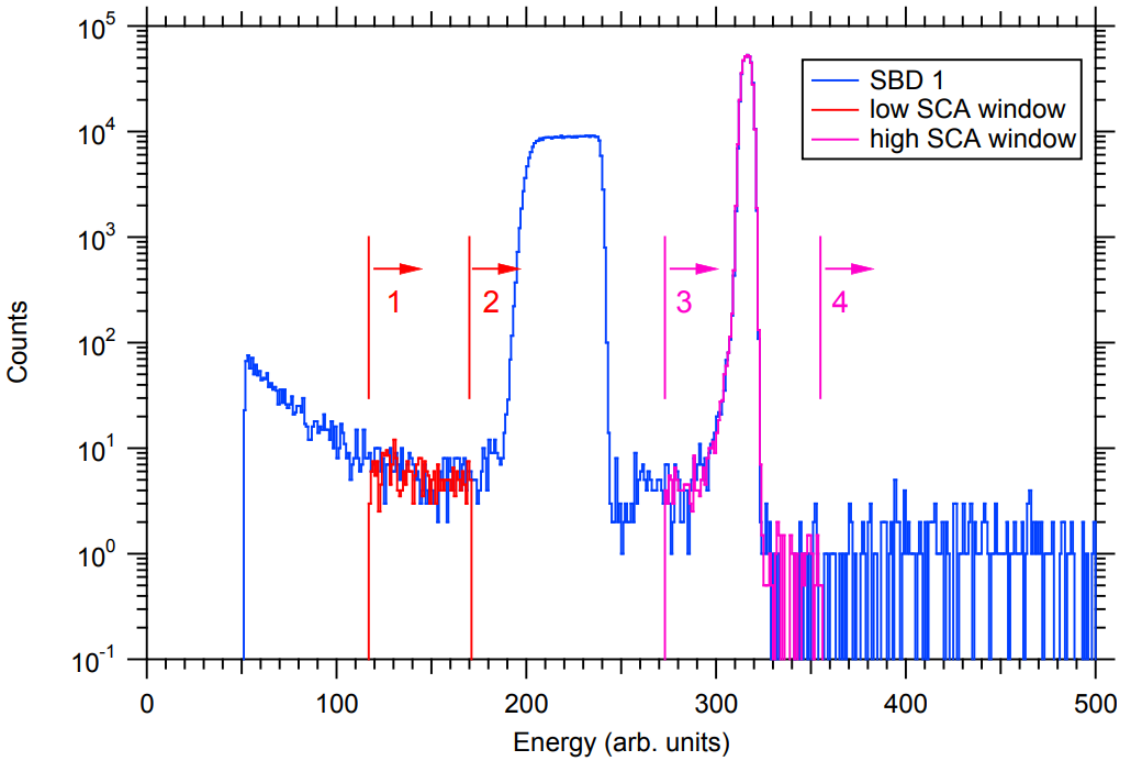

Figure 4.1: Example of the energy spectrum of the reaction products from $^6Li(n,t)^4He$ in the $1/v$ neutron fluence monitor with the SCA thresholds overlaid.

two of the windows gives the total number of events. Thresholds 1 and 2 are both set below the lowest energy alpha events. The counts from these two thresholds give a handle on the noise and background rates. Threshold 3 is set in-between the two signal peaks and threshold 4 is above the highest energy triton events. With these thresholds, the number of triton events is determined by the difference in the counts above threshold 3 and the counts above threshold 4, and the number of alpha events is determined by the difference in the counts above threshold 2 and the counts above threshold 3. Background rates are also monitored by looking at the difference in counts between threshold 2 and threshold 1 as well as looking at the counts above threshold 4 alone for any change in the high energy background. An example of the neutron fluence monitor energy spectrum with the location of the SCA thresholds overlaid can be seen in figure 4.1. For every run in a series, 16 integer counts (4 per detector) are recorded by the DAQ in a binary format. Using this data the neutron beam fluence can be determined and many diagnostics can be checked. The total event rate of alphas plus tritons in the fluence monitor per run, $N_{(\alpha+t)r}$, which is proportional to the total beam fluence, is calculated by first reading in the binary data file from the DAQ and exporting it into a text file. This text file consists of 16 columns of integers, one for each threshold from the SCAs, and has rows equal to the number of runs, an example of this file can been seen in appendix A. Using this file, the total event rate in all four detectors is calculated by:

$$N_{(\alpha+t)r} = \sum_{i=1}^{4}(T_{3i} - T_{4i}) + (T_{2i} - T_{3i}) = \sum_{i=1}^{4}(T_{2i} - T_{4i}), \tag{4.1}$$

where i is indexed for the 4 detectors and T_x corresponds to the threshold of that label. As can be seen from figure 4.1, the signal to background rate in the detectors is better than 1000 to 1, this means the background subtraction is small and not critical for the uncertainty goal of the experiment. However, the vast majority of the low energy events in the spectrum are neutron beam induced. Which means it is not possible to do a beam-on, beam-off background subtraction. This means that the background subtraction must be done using only the threshold values. The background rate is low enough so that it is not necessary to do this background subtraction for day to day data taking, but the final background subtraction method still needs to be developed for final analysis.

Additionally, a good test of the quality of the energy spectrum is the ratio of the alpha and triton counts. If there is no noise, this ratio should be identically = 1, this ratio is calculated as:

$$R_{\alpha/t} = \frac{T_2 - T_3}{T_3 - T_4}. \tag{4.2}$$

With every series that is taken this ratio is checked and used a metric of the goodness of the noise levels of the spectrum. If there is extra low energy noise that starts to intrude into the alpha energy range, this ratio becomes > 1. The detectors are independent of each other so this check must be made for all detectors. For every series, a set of four plots are created using the above prescription for the alpha and triton counts. $R_{\alpha/t}$ is plotted as a function of run number and fit to a constant. An example of this can be seen in figure 4.2. The deviation from 1 is then calculated, and if the fit value is more than two sigma from 1, the series is flagged. If the deviation from 1 is greater than 3 sigma, data taking is normally stopped immediately and steps are taken to resolve noise issues. Once the neutron counting efficiency is determined using Alpha-Gamma, calculating the neutron fluence per run is then straightforward. The efficiency is determined in such a way that the total neutron fluence is a multiplicative factor on $\dot{N}_{\alpha+t}$ [3].

4.2 Determination of the Proton Rate

The most analysis intensive portion of the experiment is the determination of the proton rate. During every trapping cycle, the proton detector signal is recorded, and because this is an absolute counting experiment, a determination must be made whether a proton is present or not. Depending on the trapping time, upwards of 10^7 events must be examined per day. In addition to making a determination on every trap opening, numerous corrections must be made to account for the proton detection efficiency being slightly less than 100 %. In the sections below I will detail how the determination of each trap opening is made, see chapter 6 for details corresponding to corrections made to the proton rate.

The proton detector electronics chain is made up of a single crystal Si detector and a low noise preamplifier made specifically for this experiment. The output of the preamp is sent via a fiber optic cable into a NIM module and split into two parallel signals. The first

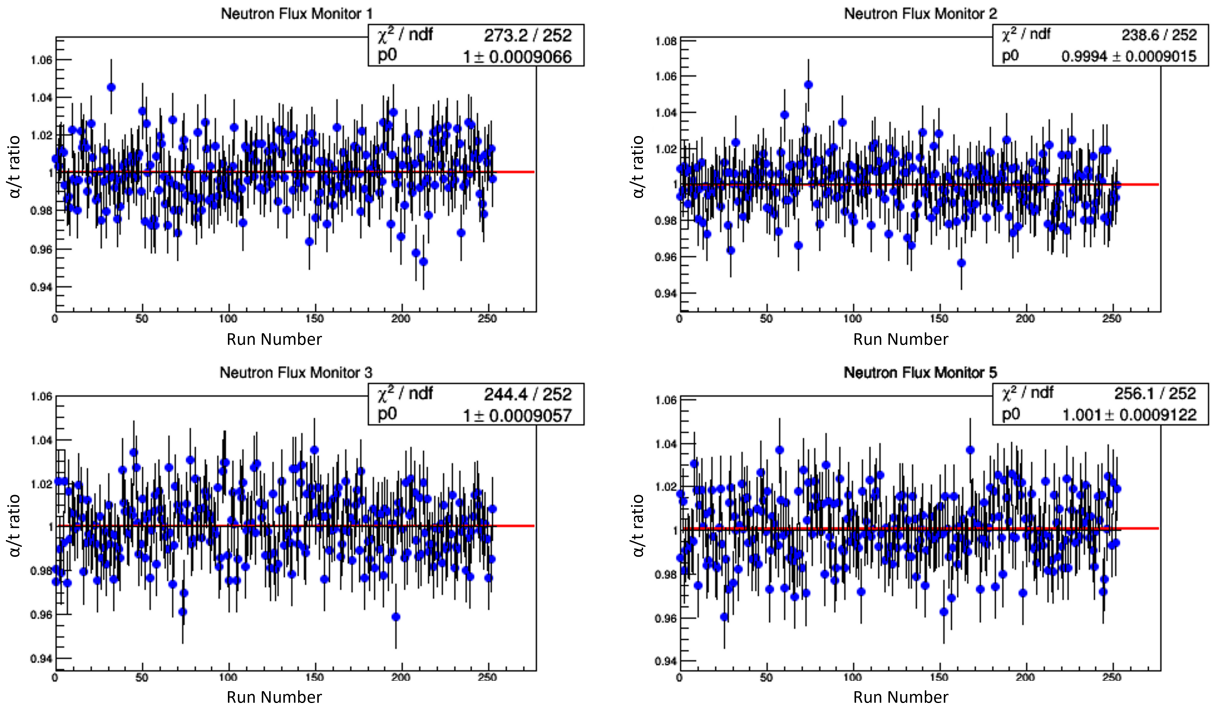

Figure 4.2: Example of $R_{\alpha/t}$ ratios for each detector vs run number, fit to a constant. These plots are typically color coded by deviation from 1. Blue: within two σ of 1, yellow: between two and three σ away from 1, red: more than three σ away from 1.

signal is untouched and sent directly into a GaGe digitizer before being recorded by the DAQ computer. The second signal is sent into a specamp NIM module, this acts as a Gaussian filter and transforms the output of the preamp into a smooth Gaussian pulse. This pulse is then also sent to the GaGe digitizer before being recorded by the DAQ. For every trap opening the DAQ saves these two waveforms as 2,048 shorts and writes them to a binary file for each run. Therefore, each run consists of 20,000 waveforms, two for each of the 10,000 trap openings. To reduce the computation time necessary for detailed analysis, the DAQ has a software energy threshold. This threshold can easily be adjusted and is set so that it filters out most of the no-proton trap openings while allowing all proton events above the noise to be written into a separate file. To do this, the DAQ generates a simple energy spectrum using the maximum value of the specamp output. After a few runs, there are enough counts so that a rough spectrum may be seen. The threshold is adjusted so that it is lower than the noise wall while cutting out most of the noise peak. The noise is dominated by the detector capacitance so this threshold must only be reset when the detector is changed. Because this is just a measure used to save computation time, this threshold is always set conservatively to insure that no proton events are missed. After each run, the DAQ sends the waveforms that had energy above threshold to a remote server that is used for data storage and analysis.

The data is saved in binary files to minimize storage requirements. The data files consist of 2,048 time bins for each waveform plus a time stamp that corresponds to which trap opening the waveforms is from. Each time bin entry is a signed short integer that requires 2 bytes per bin, each time stamp is a double requiring 8 bytes. For a single waveform, 2,048 shorts plus 1 double is saved. For each trap opening two waveforms, the preamp and the specamp plus a time stamp for each is saved. Therefore, the file format for a single trap opening is:

```
double (8 bytes) - time stamp of specamp (channel 1)
short  (2 bytes) - time bin 0 for specamp
...
short  (2 bytes) - time bin 2047 for specamp
double (8 bytes) - time stamp of preamp (channel 2)
short  (2 bytes) - time bin 0 for preamp
```

```
...
short  (2 bytes) - time bin 2047 for preamp
```

for a total of 8,208 bytes per trap opening. As previously mentioned, the DAQ saves two proton data files per run, one with all trap openings recorded (s_XXXX_r_XXXXXX_5.dat) and one with only the waveforms above threshold (s_XXXX_r_XXXXXX_1.dat), where the X's are an index of the series and run respectively. The s_XXXX_r_XXXXXX_5.dat files are identically 82080000 bytes ($\approx$ 82 MB) for every run, these files are only kept locally and are not sent to the remote server to save hard disk space and resources. The s_XXXX_r_XXXXXX_1.dat files are sent to the remote server for further analysis, depending on the trapping time these files range in size from $<$ 1 to 8 MB per run. Almost exclusively, the analysis methods below are done on these s_XXXX_r_XXXXXX_1.dat files.

As mentioned in section 3.5, the digitization of the proton waveforms allows for more sophisticated analysis techniques to be used than in previous in-beam experiments. In principle, the analysis for this type of experiment is simple. The energy and the arrival time of the proton must be determined but neither needs to determined with extreme precision. In BL1, the Gaussian shaped specamp pulse was exclusively used for analysis. The maximum of this waveform and the time bin where this maximum occurred was saved and a simple signal on, signal off background subtraction was done, taking advantage of the known proton arrival time window. The difficulty of determining the proton rate comes from the absolute counting nature of the experiment. A determination must be made for each trap opening if there was a proton present or not. Because of this, it is important that the analysis method has good noise rejection and is robust over a wide range of signal energies and types. Previously, it was not possible to tailor the analysis technique, adapt the filter parameters to changing experimental conditions, or have any absolute timing information. A new analysis method has been developed that uses a finite impulse response software filter on the raw preamp waveform. The specific filter used is a trapezoidal filter that has been shown to have advantages for high resolution applications [58]. Below I will detail the development, implementation, advantages, and results achieved using this filter to analyze the BL2 data.

4.3 Trapezoid Filter

A trapezoid finite response filter is applied to the raw preamplifier to extract the proton energy and arrival time. A detailed derivation and discussion of the trapezoid and other filters can be found in reference [58]. A trapezoid filter is ideal for extracting the energy in circumstances where the rise time of the waveform is short and the exponential decay time is long. For this experiment, the rise time of a proton is $< 0.4\,\mu s$ and the decay time of the exponential tail is $> 50\,\mu s$. The trapezoidal output is generated by convolving the trapezoid shaper impulse response with the raw preamplifier waveform. In practice, it is computationally expensive to preform this convolution with every single waveform generated. A mathematically identical recursion relation exists for discrete data [58], this is used in place of the trapezoid shaper impulse response. This analysis uses the recursion relation; however, for simplicity, an example will be shown using the convolution. If $h(t)$ is the trapezoid shaper impulse response:

$$h(t) = \begin{cases} \tau_{decay} + t; & t < \tau_{rise} \\ \tau_{rise}; & \tau_{rise} \leq t < \tau_{rise} + \tau_{top} \\ 2 \cdot \tau_{rise} + \tau_{top} - \tau_{decay} - t; & \tau_{rise} + \tau_{top} \leq t < 2 \cdot \tau_{rise} + \tau_{top} \\ 0; & t \leq 2 \cdot \tau_{rise} + \tau_{top} \end{cases} \tag{4.3}$$

where t is a time bin, τ_{decay} is the decay time of the exponential tail of the preamp waveform, τ_{rise} is the length of the trapezoid legs, and τ_{top} is the length of the trapezoid top. If $v(t)$ is the raw preamp waveform then $s(t)$, the output of the trapezoid filter is given by:

$$s(t) = \frac{1}{\tau_{rise}\tau_{decay}} \sum_{k=1}^{length} v(k)h(k-t), \tag{4.4}$$

where *length* is the total length of the discrete waveform. For an example of the exact recursion relation used in the analysis, see appendix B. The trapezoid shaper impulse response can be seen in figure 4.3 with an example of the output of the trapezoid filter

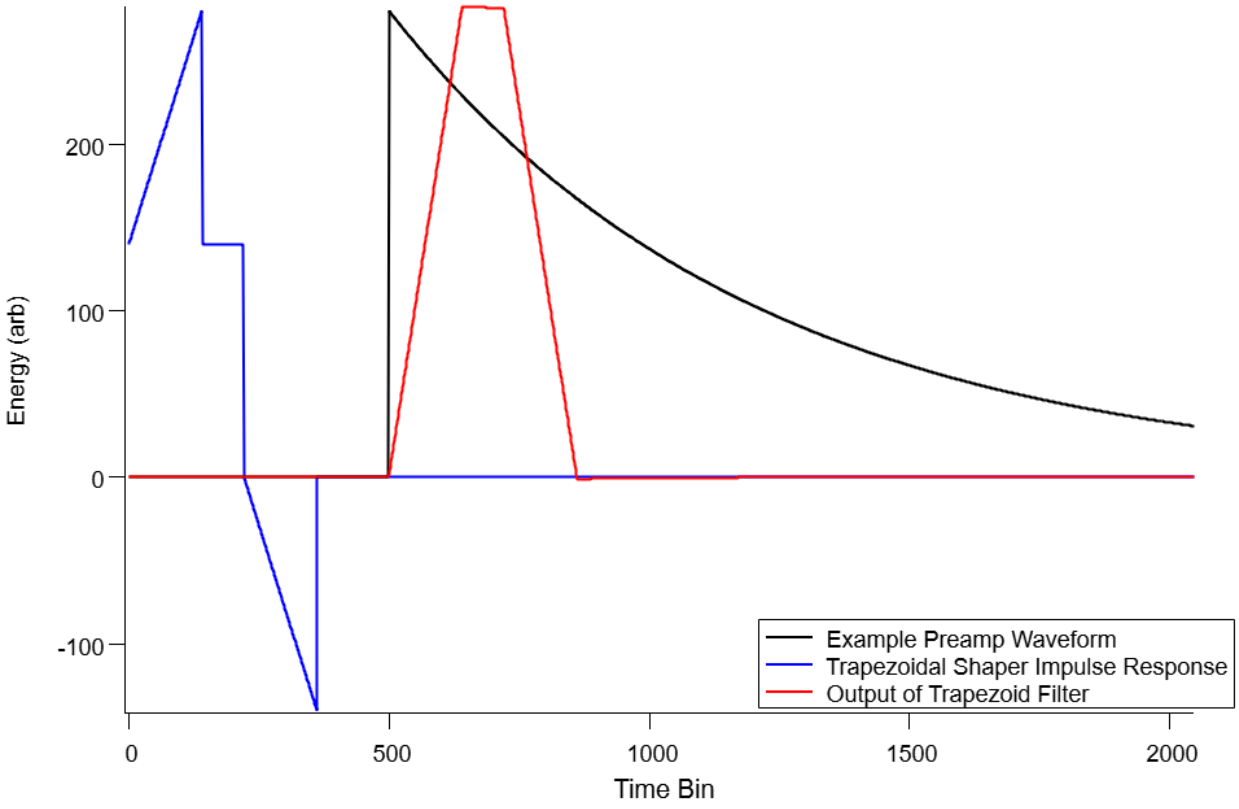

Figure 4.3: Example of the trap filter convolution on a generated preamp waveform.

for a perfect preamp waveform. The output of the trapezoid filter for a perfect preamp waveform with Gaussian noise added can be seen in figure 4.4.

The trapezoid output has many useful features. It increases the signal to noise of each waveform while not distorting the original energy and arrival time of the preamp waveform. If the correct parameters are used it also has a unique shape that can be used for pulse shape analysis, the two legs of the trapezoid should be equal in magnitude but with opposite slopes and the top of the trapezoid should be flat. If the decay time parameter of the trapezoid filter is slightly mismatched from the real decay time of any waveform, this can lead to an unflat top. To avoid biasing the energy extraction from this effect, the midpoint of the top of the trapezoid is used instead of the maximum of $s(t)$. This is done by first finding the maximum of the output trapezoid, $s(t_{max})$ and then finding times $s(t_1)$ and $s(t_2)$ with the requirement that:

$$s(t_1) \leq 0.7 \cdot s(t_{max}) \leq s(t_1 + 1)$$
$$s(t_2) \geq 0.7 \cdot s(t_{max}) \geq s(t_2 + 1).$$

The corresponding midpoint time is calculated by $t(mid) = \frac{t_1+t_2}{2}$, then the energy extracted from the trapezoid filter is $s(t_{mid})$. As an example of how using the midpoint makes the energy extraction more robust, let's consider the cases shown in figure 4.5. Assume there are three example preamp waveforms of the same energy, one with the assumed correct fall time, $\tau_{preamp} = \tau_{decay}$ and the other two with a fall time of $\pm\, 5\%\ \tau_{preamp}$. The trapezoid filter is then applied to these three waveforms resulting in three output trapezoids that should all have the same energy. As seen in figure 4.5, the input energy of the example preamp waveforms are all 280. If one were to naively take the maximum point of the output trapezoid filters one would see a deviation of as much as 1 % from the input energy. However, if one applies the midpoint method described above, the extracted energies are within 0.05% of the input energy. A summary of the energies extracted using these two methods can be seen in table 4.1. Using the midpoint of $s(t)$ for the extracted energy also gives more noise suppression than using the maximum. If the maximum of the waveform were used, the extracted energy is more sensitive to single noise spikes.

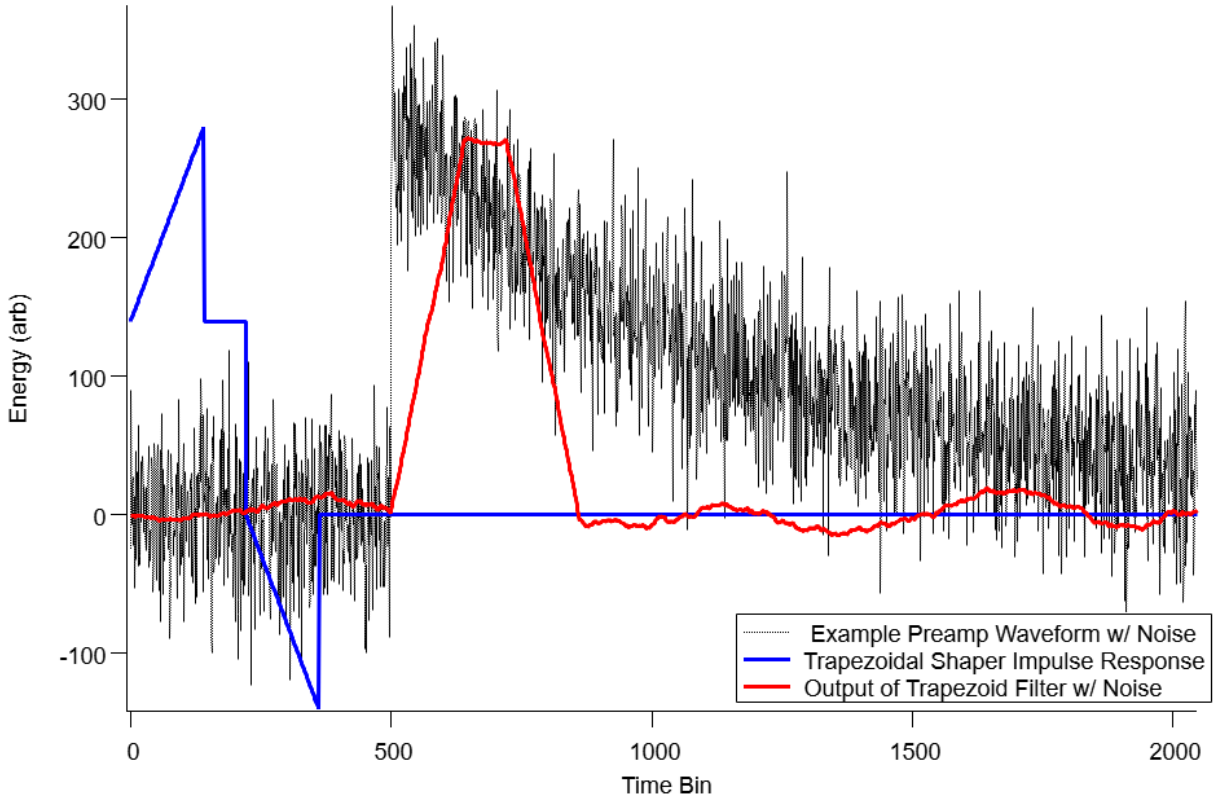

Figure 4.4: Example of the trap filter convolution on a generated preamp waveform with typical noise added.

Table 4.1: Comparison of extracted energy from the trapezoid filter for waveforms with varying exponential decay times. The consistency of the extracted energy shows advantage of using the trapezoid output midpoint rather than the maximum.

Fall Time	$s(t_{max})$	t_1	t_2	t_{mid}	$s(t_{mid})$
700	280.39	598	762	680	280.06
735	281.31	599	765	682	280.04
665	282.71	598	759	679	280.11

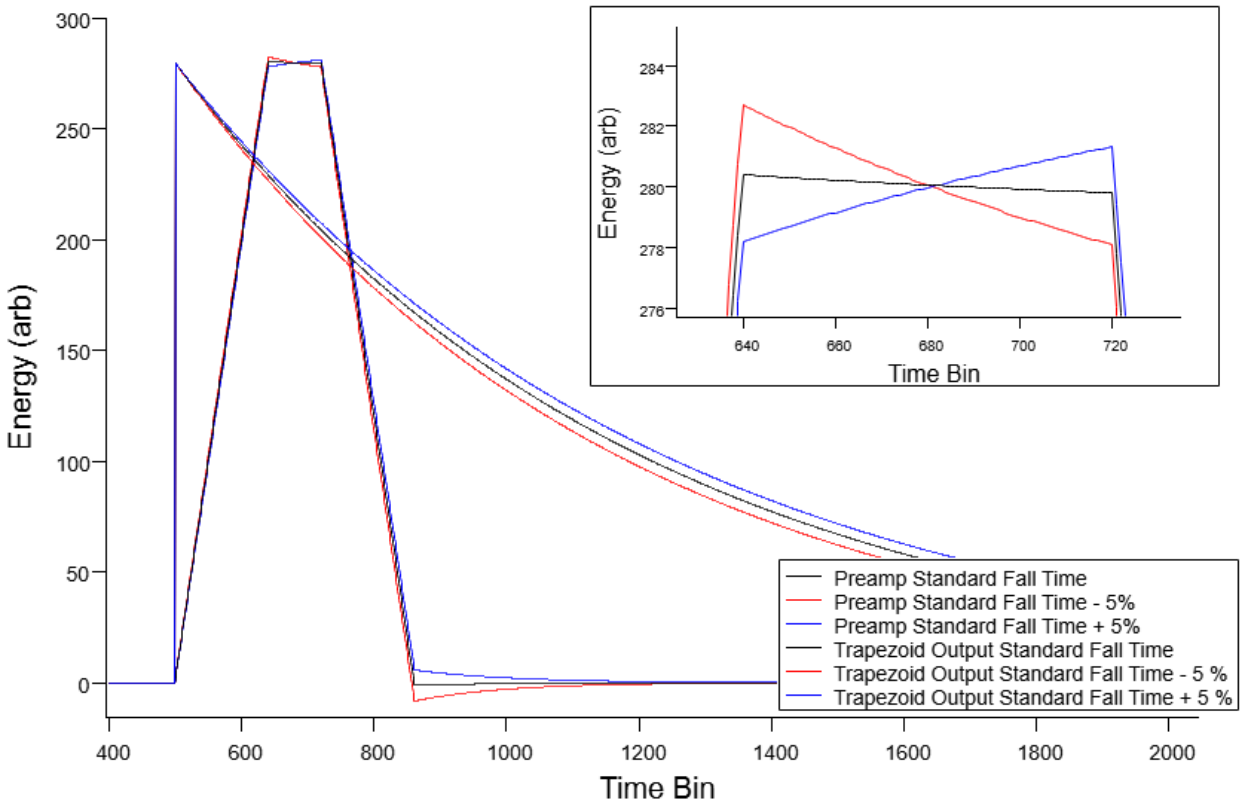

Figure 4.5: Example of the dependence of the output trapezoid filter on the fall time of the preamp waveform.

The trapezoid filter can also be used for pulse shape discrimination. One expects that if the decay time is well known, then the shape of $s(t)$ is symmetric. This means that the two legs of the trapezoid will have the same magnitude slope. These legs can be independently fit to a linear function and if $v(t)$ is well understood, the fits will be equal in magnitude but with opposite sign. This procedure has been used to verify that the chosen τ_{decay} fits the data well. On a waveform by waveform basis this can also be used to significantly increase signal to background. One can choose waveforms that have legs with slopes in good agreement and tops that are flat. Depending on how strictly the requirements are chosen this can functionally eliminate all noise waveforms from the data. While this is not a useful prescription for lifetime data taking because the precise efficiency of the cuts is not known, it can be useful for systematic tests where relative rates are being compared. If relative rates are being compared, then the cut efficiency does not need to be known, only that it is constant for similar data. Using the trapezoid filter allows the analysis to be tailored to the specific needs of the tests being run. If lifetime data is being taken, then the trapezoid filter increases the energy resolution and noise suppression compared to the traditional methods. The trapezoid filter also allows for an absolute extraction of the arrival time of the events, which was not previously possible. If systematic tests are being done, the trapezoid filter can be used for pulse shape analysis to significantly increase the signal to background ratio. In the sections below I will discuss how the trapezoid parameters were optimized, how the new analysis methods were benchmarked and how the analysis is used to determine τ_n.

4.3.1 Parameter Optimization

The output trapezoid shape depends on a number of parameters. To obtain a flat top, using the correct decay time is crucial. The decay time parameter must be set equal to the decay time of the exponential tail of the preamp waveform. Since the decay constant of the waveform is almost solely a function of the electronics chain, it is not necessary for the decay parameter to be adjusted for different detectors. Several different methods were used to determine the correct decay time parameter. The first method was fitting every preamp waveform before applying the trapezoid filter. This was done to try to account for any drifts in the electronics. There were two main problems with this method: 1) fitting each

waveform increased the analysis time, and 2) difficulty in fitting to imperfect pulses. If a waveform had a baseline oscillation or multiple events separated in time, the fit could either fail or fit to a nonsensical value. Using the fit value for each waveform lead to an increased peak width in the proton energy spectrum and was abandoned. Another method that was tried was creating an average of many "good" waveforms so that noise was averaged out and a "perfect" proton waveform was generated. However, because protons can arrive in a time window much larger than the rise time of the waveform, the generated perfect proton waveform had a softened leading edge that did not do a good job representing the data. It is possible to only choose proton events that arrive in a very narrow time window to alleviate this issue, however this significantly decreases the usable event rate. In the end, a parameter scan was done over a wide range of decay parameters to optimize the energy resolution of the proton energy spectrum.

To determine the optimal trapezoid filter parameters, a scan was done over the τ_{top}, τ_{rise}, and τ_{decay} parameters. Figure 4.6 shows a two dimensional scan over τ_{top} and τ_{rise} where a larger value on the color scale is proportional to better energy resolution. The energy resolution was determined by fitting a Gaussian to the single proton energy peak and taking the ratio of the peak position and the width of the peak. The ideal energy resolution occurs with a zero length top [59], but this neglects real effects like waveform noise, pileup events, and the finite risetime resulting in ballistic deficit. Ballistic deficit occurs because charge liberated inside the detector is all collected by the cathode and the anode of the detector over a finite period of time. Because charge collection does not occur instantaneously, some charge will have dissipated before it is collected. The difference in the amplitude of the output waveform with the finite shaping time and one that would have been produced with an infinite shaping time is the ballistic deficit. Typically, a correction would be needed for a precision energy spectrum to be made. Because the ballistic deficit should be similar for all waveforms and accurate energy information is not required for a counting experiment, we can focus solely on the energy resolution of the proton energy spectrum.

Something unique to this experimental method is the control over the arrival time of events. The control over the trapping potential causes trapped protons to arrive at the detector in a small, finite time window, but this also means all trapped protons hit the

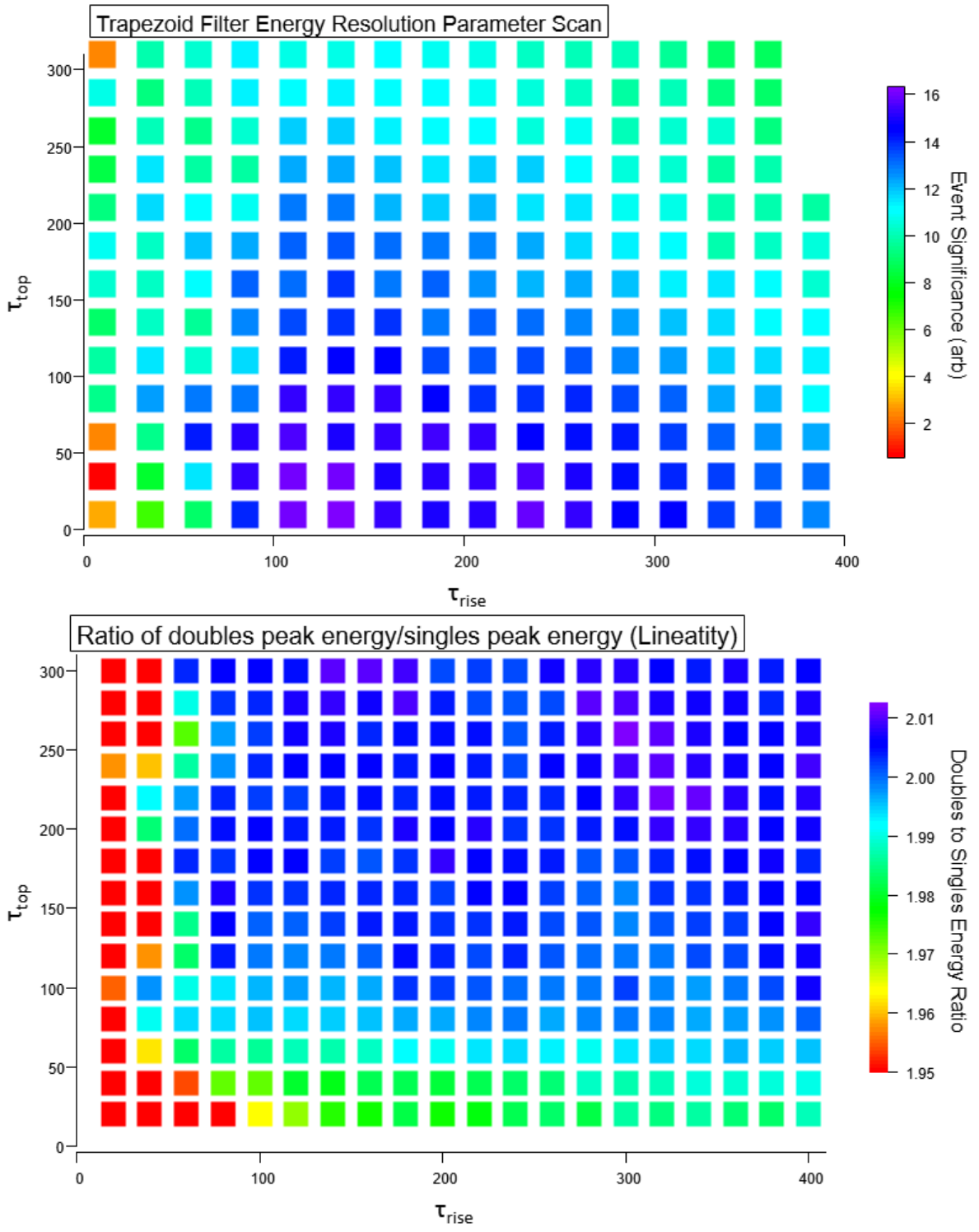

Figure 4.6: Heat map of a trapezoid filter parameter scan. Top: color scale is proportional to energy resolution, bottom: color scale is the ratio of the extracted energy of double proton and single proton events.

detector in that time window. For all trapping times there is a significant probability that multiple protons may be trapped in any single trapping cycle. Because of this, pileup, when multiple protons hit the detector at similar times, must be handled appropriately. If multiple protons arrive at the detector, the time separation depends on the ramp voltage. In general, this time separation ranges from 0 to 20 μs. Even the maximal time separation between protons from the same trapping cycle causes the proton waveforms to significantly overlap. Because of this, the top parameter of the trapezoid filter must be long enough to fully integrate this type of event. Figure 4.6 shows the energy resolution for only single proton waveforms, thus it does not suffer from having too short of a top parameter. If single proton events were the sole data type in the experiment the optimization would be rather straightforward. However, the top parameter must be long enough to integrate time separated proton events while having the highest energy resolution possible.

To optimize the trapezoid filter parameters, parameter scans were done to increase energy resolution, test linearity and test biases in extracting the energy and arrival time of the protons. The top parameter must be long enough to integrate time separated proton events while having the highest energy resolution possible. As can be seen in figure 4.6, the theoretical prediction that the energy resolution is maximized with a triangular filter ($\tau_{top} = 0$) is valid. One can see that after τ_{rise} is greater than 60 time bins, the energy resolution is best when $\tau_{top} = 0$ and smoothly becomes worse as τ_{top} is increased. However, because the analysis must be able to identify multiple proton events that have different arrival times, an increased top length effectively increases the integration time of the filter making it more robust. While the energy resolution is maximized with a zero length top for single proton events, the energy resolution decreases when multiple proton events are analyzed. To account for this, a similar parameter scan was done looking at the energy resolution and linearity of multiple proton events. One would expect that multiple protons in the trap can be treated as independent. Therefore two trapped protons will deposit, on average, double the energy as a single proton event. To test this, the ratio of the single and double proton energy peaks is plotted on the color axis for a parameter scan. As can be seen in the second plot of figure 4.6, when either τ_{rise} or τ_{top} is too short the ratio of the two energies deviates from the expected ratio of 2. It can be seen that generally the linearity is

better when the trapezoid parameters are long, but this decreases the energy resolution. This means there is no obvious optimized set of trapezoid filter parameters in all scenarios. The optimized parameters were chosen so that the top parameter could be long enough so that the double proton energy would be within 1 % of the expected value while still retaining as much energy resolution as possible. The chosen optimized parameters for energy extraction were $\tau_{top} = 80$ and $\tau_{rise} = 140$. The filter using these parameters will be called the "energy optimized trapezoid filter" denoted by $S_E(t)$. Figure 4.7 shows a comparison of a proton energy spectrum from BL1 (red) and BL2 (black). In addition to the reduction in the noise, one can see the proton peak widths are significantly narrower using $S_E(t)$ to extract the proton energy.

4.3.2 Analysis Benchmarking with Pseudodata

Pseudodata was generated to mimic the output signal of the preamp with the goal of benchmarking the new trapezoid filter analysis. The pseudodata was generated by first analyzing high quality data and making probability density functions (PDFs) out of the energy and timing spectra histograms. Then, these PDFs were used as input files for the energy and time of a model function to mimic the preamp waveforms. To generate each pseudo waveform a random energy and arrival time is chosen from the two PDFs. The pseudo waveforms are generated using:

$$V_{out}(t) = A\left(\frac{t}{\tau}\right)^{j} e^{\frac{-t}{\tau}}, \tag{4.5}$$

where τ is the fixed fall time of the decaying exponential, j is proportional to the rise time, A is a scaling factor to match the energy, and t is the time bin ranging from 0 to 2047. For a single proton this generates a perfect pulse where the energy and time are exactly known before any noise is added to the waveform. To further mimic the real lifetime data, Gaussian distributed noise is added on top of this perfect pulse. To get the correct distribution of noise, the root mean square (RMS) of real, pure noise waveforms is calculated on a waveform by waveform basis. The RMS of each waveform is then histogrammed so that a distribution of noise spectrum is generated. To apply this noise spectrum to the pseudodata

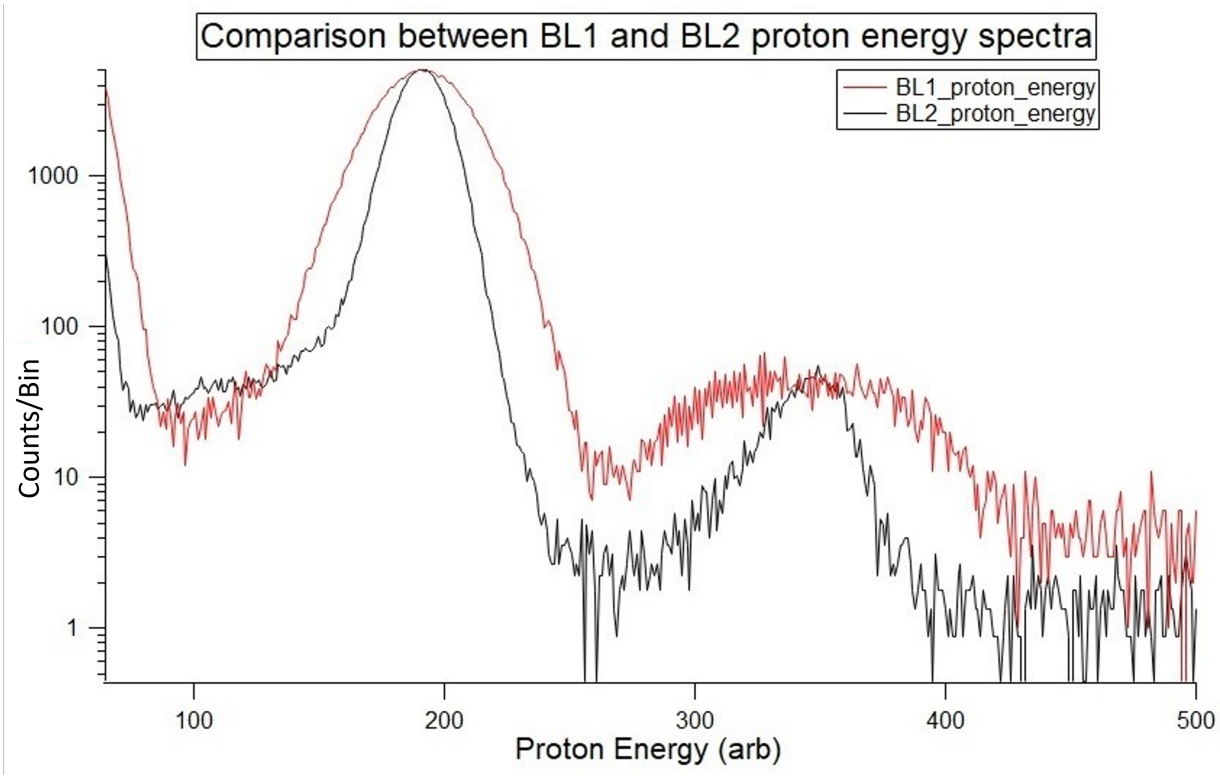

Figure 4.7: Comparison of analyzed energy spectra for similar detector types with the standard BL1 (red) and the optimized trapezoid filter analysis (black), normalized to the peak value.

waveforms a Gaussian noise function is used with input parameters taken from the fitted noise distribution histogram. This way of generating pseudodata can be used to create a wide range of waveforms that mimic most (if not all) possibilities of real data. This includes single and multiple proton events, pure noise events, and a variety of background events including high energy electron and cosmic events as well as combinations of protons and background events in the same waveform. Appendix C shows examples of the types of pseudodata that were created.

The purpose of generating this pseudodata was two-fold. First, the pseudodata was used to check the optimized parameters of the trapezoid filter. This is useful because the energy and arrival time of each individual waveform is known beforehand so an absolute comparison on a waveform by waveform basis can be made. In addition to optimizing the energy resolution by minimizing peak widths, one is also able to check for systematic biases that could result in misidentification of events, this is only possible with pseudodata. Checks of the proton arrival time are particularly difficult with real data because of the low signal to noise ratio and no known value for the sharp rise time of the preamp proton pulses. Additionally, the shape of the timing spectra is not fit by any regular function. Therefore, it is not possible to run a parameter scan that minimizes some width parameter. Instead, a comparison to pseudodata is used for an absolute comparison to the arrival time of events. Because of the fixed risetime of both the pseudodata generation and the trapezoid filter, absolute comparisons are easily made.

Using this type of comparison, a parameter scan can be done to see what effect the risetime and top length have on the accuracy of arrival time extraction. Figure 4.8 shows a comparison between a short (20 time bins) and a long (180 time bins) risetime parameter trapezoid filter with a zero length top. This shows there is very little dependence on the risetime length to the arrival time extraction as long as the appropriate risetime offset is accounted for. This allows for the choice of risetime to be driven by other factors, including noise suppression and the buffer length required to have a proper energy or time extraction. The buffer length is caused because the shaper impulse response needs to fully integrate a time bin before the energy or time can be fully reconstructed. Therefore the buffer length is $2\tau_{rise} + \tau_{top}$. Only time bins within this value of either end of the waveform are considered to

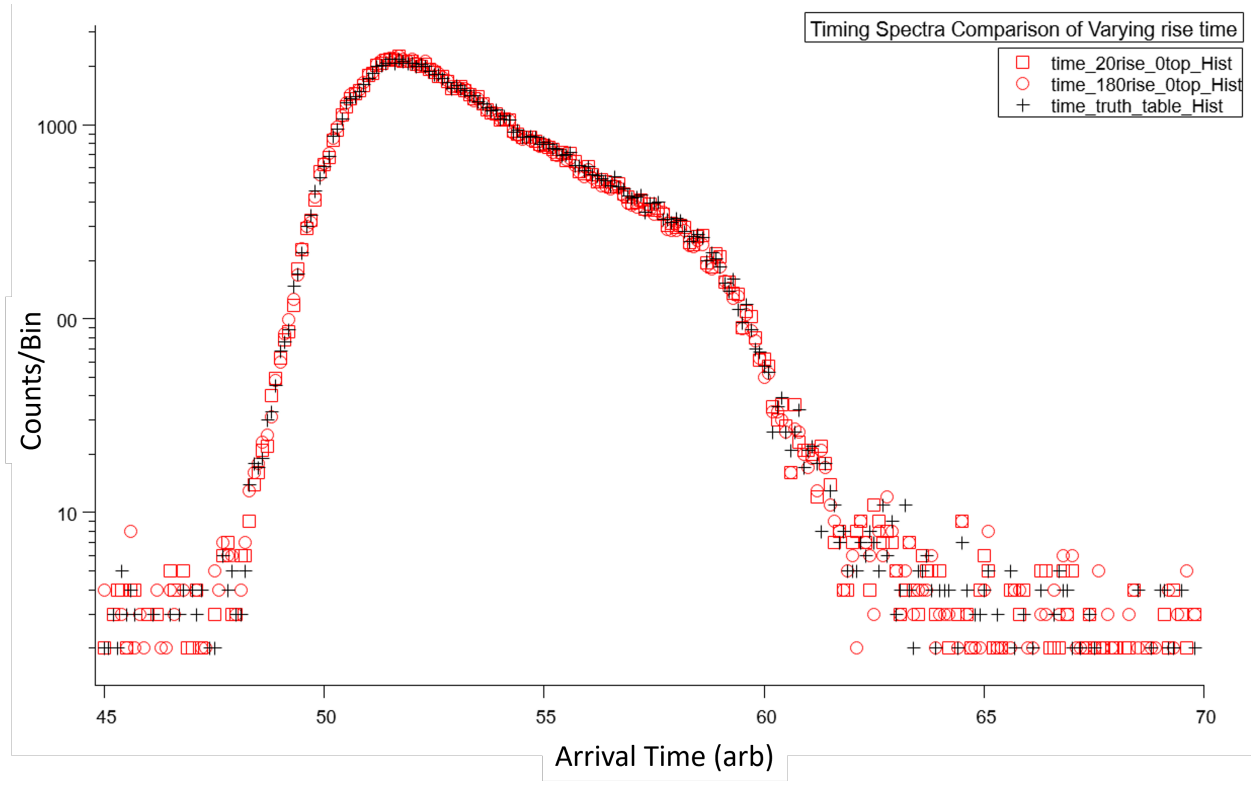

Figure 4.8: Comparison of the extracted arrival time with pseudodata for a $\tau_{rise} = 20$ and a $\tau_{rise} = 180$ trapezoid filter.

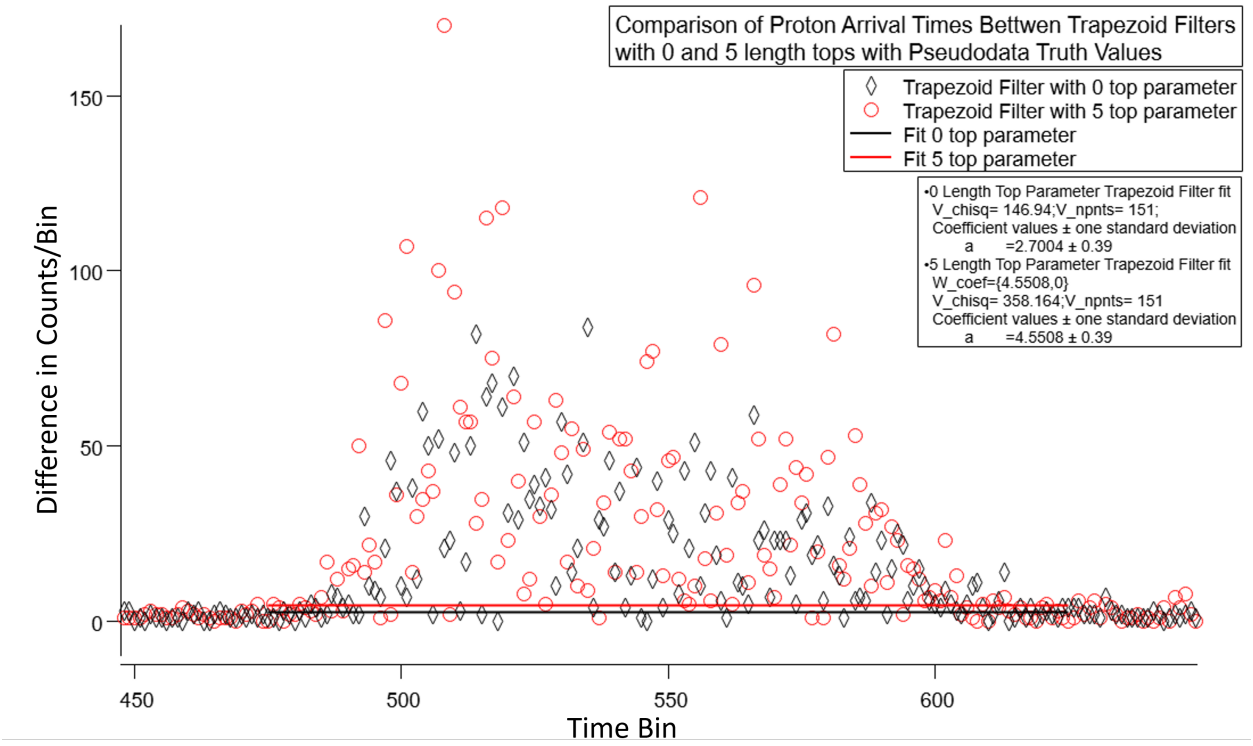

Figure 4.9: Absolute difference between pseudodata arrival time compared with a $\tau_{top} = 0$ and a $\tau_{top} = 5$ trapezoid filter, showing larger error when the top parameter is increased.

be good points. Figure 4.9 shows a comparison between the extracted arrival time between filters with $\tau_{top} = 0$ and $\tau_{top} = 5$. Increasing the top length of the trapezoid filter slightly increases the width of the arrival time peak, and leads to a larger difference in the extracted arrival time when compared to pseudodata. For precise timing information, the chosen optimized parameters were $\tau_{top} = 0$ and $\tau_{rise} = 60$, the filter using these parameters will be refereed to as the "short trapezoid filter" denoted by $S_s(t)$. Figure 4.10 shows a comparison of the extracted timing spectrum histogram with the optimized filter parameters compared to the known pseudodata values.

Using a zero top length trapezoid filter is useful for comparison to simulated timing spectra because it allows for the most accurate extraction of the arrival time and the narrowest peak width. This absolute comparison allows for a benchmark of the simulation that was not previously possible with other hardware filters.

4.3.3 Multiple Proton Rate Correction

The proton detector has sufficiently linearity over the relevant energy range such that the deposited energy in the detector can be treated as directly proportional to the incident energy of the proton. Because the decay protons are born with such low energy and the energy resolution of silicon detectors is much worse than the proton's initial energy, we can also assume that all deposited energy in the detector is from the acceleration potential applied to the detector, typically -25 kV to -35 kV. Also, because of the large volume of the proton trap, if multiple protons are trapped at the same time we can assume these protons are completely independent. Therefore, if multiple protons are trapped in the same trapping cycle, they will independently interact with the proton detector, depositing the same amount of energy as a single trapped proton. Therefore, on average, multiple protons events have an integer multiple of energy deposited in the proton detector, i.e. two protons deposit twice as much energy as a single proton. There is a non-negligible probability that multiple protons are trapped in the same trapping cycle, regardless of the trapping time. The multiple proton correction depends on the trapping time and can be as large as a 10% correction to the proton rate. Using the newly developed analysis techniques, this correction can be made in two different ways.

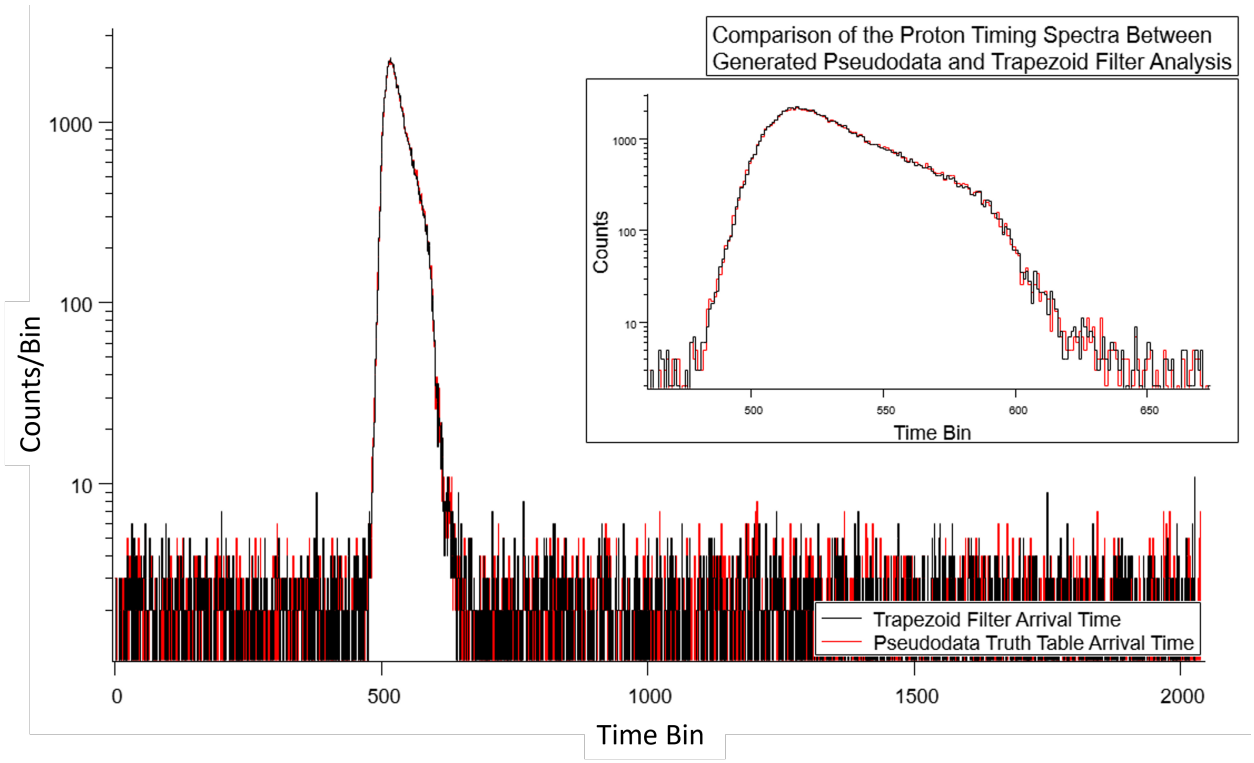

Figure 4.10: Comparison of $\tau_{top} = 0$ trapezoid filter with pseudodata arrival time.

Poisson Statistical Correction

Previous analyses accounted for multiple trapped protons by applying a Poisson statistical correction to the proton rate. Because the trapping time is fixed, the number of trap openings is fixed, and the decay probability is constant in time; the number of protons in the trap follows a Poisson distribution. The proton rate is determined by treating each trap opening as either having an event or being empty, where an event can be any number of protons. With a suitable background subtraction, the probability of there being an event, $P(1+)$, in the trap is calculated by dividing by the number of trap openings over a run. The simplest way to correct for multiple proton events is to start with the probability of having zero events in the trap, $P(0)$. $P(0)$ can be easily determined by $P(0) = 1 - P(1+)$. Then, using the general Poisson distribution equation, the probability of having k protons in a given trapping cycle is given by:

$$P(k) = \frac{\lambda^k e^{-\lambda}}{k!}, \tag{4.6}$$

where λ is the average number of protons in the trap. We see that $P(0) = \lambda^0 e^{-\lambda}$ and therefore

$$\lambda = -ln(P(0)). \tag{4.7}$$

As an example, a typical run has 10,000 trap openings, and out of those approximately 300 have an event. Using this Poisson method, we can see that $P(0) = 0.97$. Using equation 4.7, $\lambda = -ln(0.97) \approx 0.03046$ protons per trap opening. When multiplied by the number of trap openings we see that the 300 events corresponds to about 304.6 protons in the trap, approximately a 1.5 % difference. Because of the poor energy resolution and rudimentary trigger systems, this was the only way the multiple proton correction could be applied in previous experiments.

Individual Particle Identification

Taking advantage of the optimized trapezoid filter, $S_E(t)$, with significantly improved energy resolution, a new method for determining the multiple proton event correction can be used. With only a 4 keV FWHM energy resolution, the trapezoid filter analysis has the ability to distinguish multiple proton events on a waveform by waveform basis. As mentioned above,

multiple proton events deposit integer multiples of the single proton energy in the proton detector. With this energy resolution and deposited energies $> 15\,keV$ after accounting for energy loss through the deadlayer, the overlap of multiple (as many as four protons in the trap have been observed using this method) proton peaks are small in all apparatus configurations. As seen in figure 4.11, all protons peaks are well separated and easily distinguishable. Energy windows are made around each proton peak and multiple events can be counted individually. Here we can see the valley between the singles and doubles peak drops to just a few counts per bin over a small range of bins compared to > 1000 counts per bin at the maximum of the singles peak over a much wider range of bins. Using this, we can place a bound on the misidentified multiple events of $< 0.1\%$ of the whole spectrum. Given that the multiple proton events correction to the neutron lifetime is on the order of 20 s, the misidentification of multiples must be known to approximately 1%. During data analysis, both the multiple proton identification and Poisson statistics methods are employed. This gives a cross check of the correction, but good agreement between the two methods also lends credence to the Poisson method that has been used for analysis in the past.

4.4 Analysis Method for Determining the Neutron Lifetime

Using the two optimized trapezoid filters, the energy and the arrival time for each proton signal is determined. The energy is determined by using the energy optimized trapezoid filter and finding the midpoint of the output waveform, $S_E(t_{mid})$, using the method above. The arrival time of the proton, t_{arr}, is found by taking the time bin of the maximum value from the output of the short trapezoid filter, $S_S(t)$. This same process is applied for each waveform in the s_XXXX_r_XXXXXX_1.dat files. Using these two values, three basic plots are generated. A proton energy histogram, a proton arrival time histogram and a 2-dimensional histogram of proton energy and arrival time. An example of these three plots can be seen in figures 4.11, 4.12, and 4.13. Using these plots, several analysis windows are determined. As can be seen in figure 4.12, the protons arrive promptly when the door opens and all of the

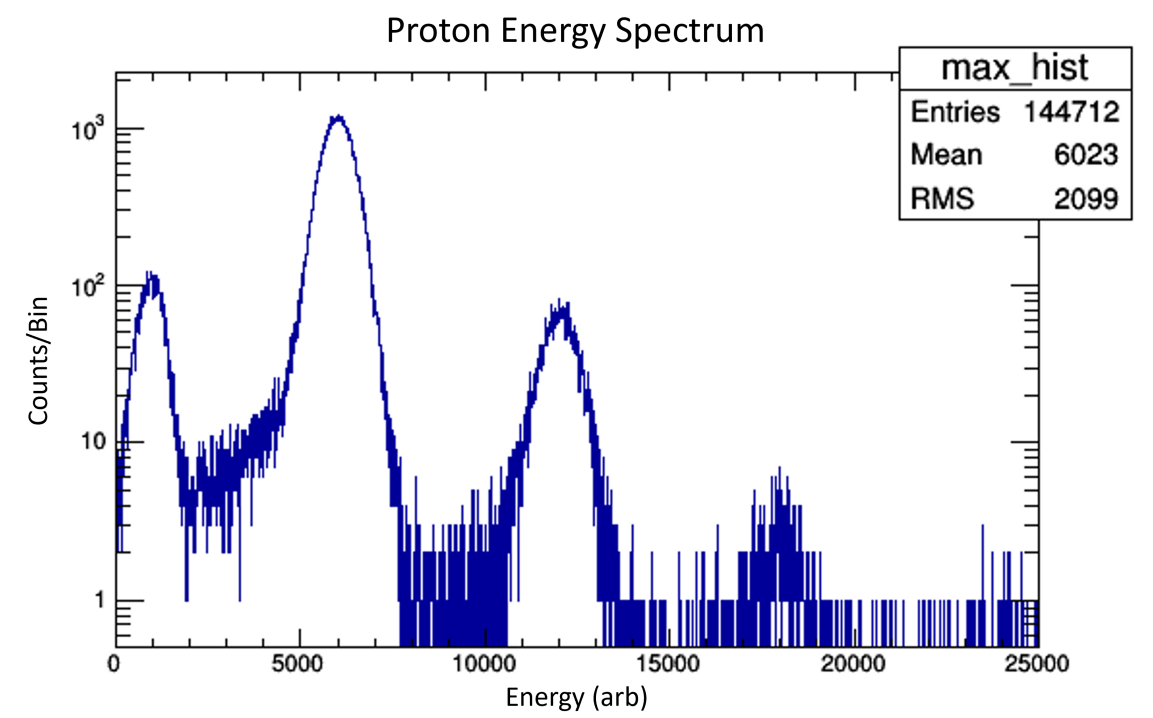

Figure 4.11: Example of proton energy spectrum, peaks from left to right: noise, single trapped proton, two trapped protons, three trapped protons, four trapped protons.

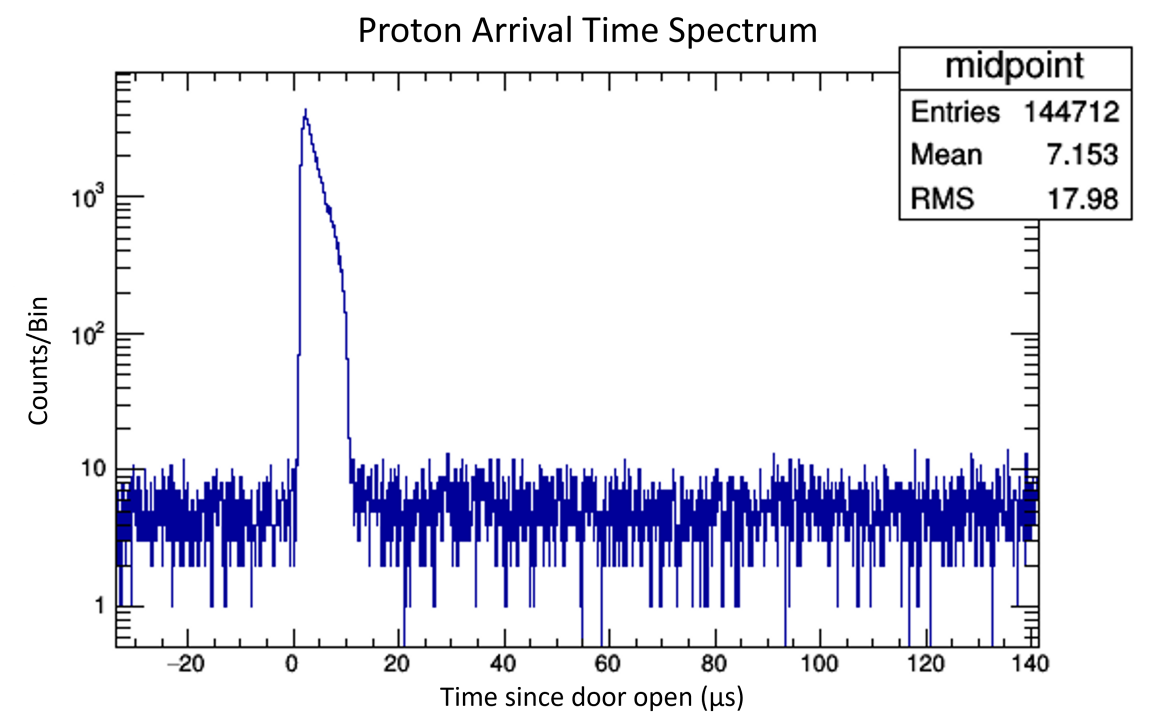

Figure 4.12: Example of proton timing spectrum, showing the narrow arrival time of trapped protons.

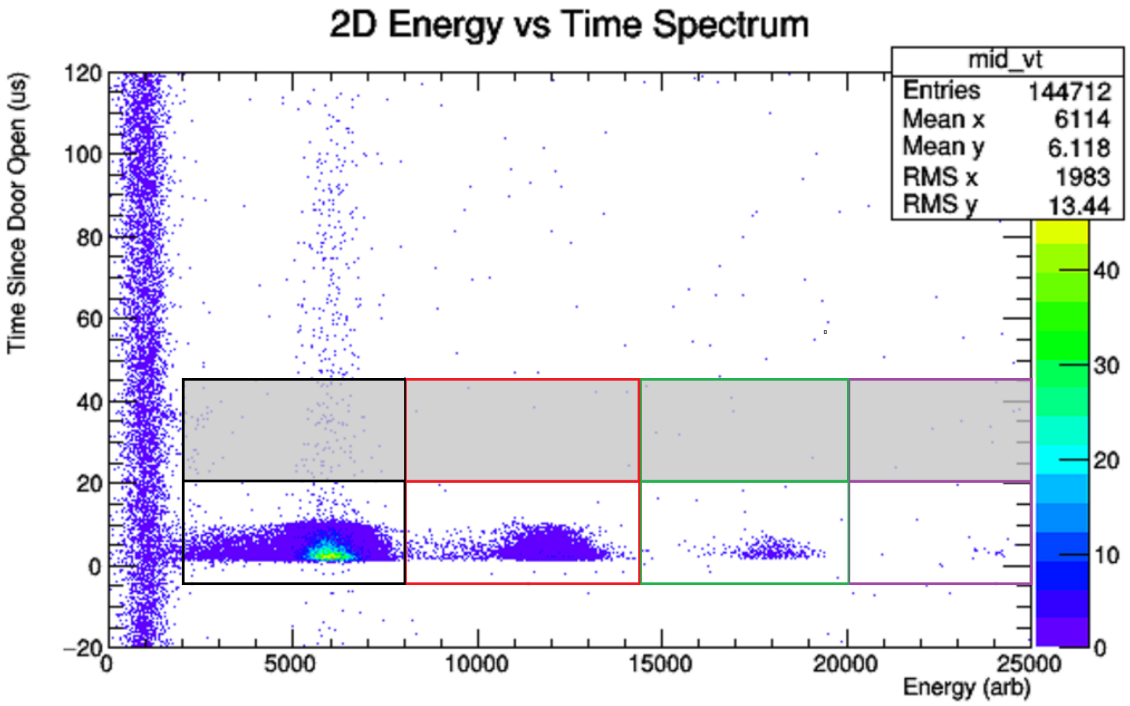

Figure 4.13: Example of a 2D histogram of proton energy vs arrival time. The windows show the analysis energy range for single (black), double (red), triple (green) and quadruple (purple) proton events. The accompanying analysis background subtraction energy windows are shown with the same colors, shaded with gray.

trapped protons arrive at the detector in about 10 μs. Different ramp voltages can change the amount of time the protons take to arrive at the detector, for small ramp voltages this can take up to 20 μs. Similarly to how the DAQ software threshold is set conservatively, the proton arrival time window is also set wider than the true proton arrival time windows and a background subtraction is done later to account for extra noise events. For simplicity, we will take the proton arrival to be -5 μs to 20 μs from when the door opened. Next, the proton energy threshold and energy windows must be determined. Using the proton energy spectra as seen in figure 4.11, the proton threshold is taken to be just higher than the noise wall, around 2,000 in this example. Then, multiple proton energy windows are determined. In this example, we see proton peaks for up to four trapped protons. The proton energy spectra shape is not symmetric, it is expected that the high energy side of a proton peak should be Gaussian while the low energy side has a tail from detector effects. For this reason, the multiple proton widows are taken to include the lower energy side of each peak. In this example, the single proton window would be approximately 2,000 to 8,000, the double proton window 8,000 to 14,500, the triple proton window 14,500 to 20,000 and the quadruple proton window 20,000 to 26,000. Using these energy windows, a comparison can be made between the Poisson statistical correction for multiple protons and individual multiple proton identification. To account for noise and background events, similar windows are used for background subtraction outside of the proton arrival time windows, as can be seen in figure 4.12. Typically, the background subtraction window is taken to be the same width as the proton arrival time windows, and placed adjacent to it. In this example, the background subtraction window would be from 20 μs to 45 μs after the door opens. If the background subtraction time window is a different width than the proton arrival time window, a multiplicative factor is necessary for the background subtraction. Figure 4.13 shows these analysis windows overlaid on the 2D proton energy and arrival time histogram.

After these windows have been defined, two parallel analyses take place, one using the Poisson statistical correction and the other identifying multiple proton events individually. For the Poisson method, the total number of events above threshold in the proton arrival window are counted, $N(Poi)_{pro}$. The number of events above threshold in the background subtraction window as also counted as $N(Poi)_{back}$. Then, a single background subtraction

is done and we are left with the total number of events above threshold,

$$N(Poi) = N(Poi)_{pro} - N(Poi)_{back}. \tag{4.8}$$

Next the probability of an event per trap opening is calculated as:

$$P(1+) = N(Poi)/10,000, \tag{4.9}$$

where 10,000 is the number of trap openings per run. As previously mentioned, the analysis is simplified by using $P(0)$ rather than $P(1+)$, $P(0) = 1 - P(1+)$. The average number of protons per trap opening is given by equation 4.7, where λ is calculated independently for each run for a check of systemic drifts. The total number of trapped protons per run is then given by:

$$N(Poi)_r = \lambda \cdot 10,000, \tag{4.10}$$

where r is an index for each run.

To get the total number of protons per run by identifying multiple protons individually, the counts in all proton energy windows must be tallied. For simplicity I will explain how this is done with only single and double proton events. In general, the analysis is done for up to four proton events. The total number of events in the proton arrival time window and the single proton window is given by, $N_1(Multi)_{pro}$ while the total number of events in the same time window and the doubles energy range is given by $N_2(Multi)_{pro}$. Similarly, the background data are taken during the timing window previously defined, but now each energy window has a separate background subtraction. The number of events in the two background subtraction windows are given by $N_1(Multi)_{back}$ and $N_2(Multi)_{back}$ respectively. Therefore, the total number of background subtracted events in each energy window is given as:

$$N_i(Multi) = N_i(Multi)_{pro} - N_i(Multi)_{back}, \tag{4.11}$$

where i is the index for each proton energy window. Since $N_i(Multi)$ is the number of background subtracted events in the arrival time window, not the number of trapped protons, a multiplicative factor is necessary to accurately count the total number of trapped protons.

Accounting for all energy windows, the total number of trapped protons for a run is given as:

$$N(Multi)_r = 1 \cdot N_1(Multi) + 2 \cdot N_2(Multi) + 3 \cdot N_3(Multi) + 4 \cdot N_4(Multi) \ldots, \quad (4.12)$$

where the multiplicative factors are for the number of protons that would be trapped in each energy window. In principle, this summation should extend to infinity but, in practice, with all trapping times used, the total number of events in the 5+ trapped proton energy windows has been consistent with background rates and can be neglected.

Now that the protons per run have been determined, the neutrons per run must be similarly determined. Using the method described in section 4.1, the total number of events per run in the $1/v$ neutron fluence monitor, $N_{(\alpha+t)r}$ are determined. As discussed in section 2.1, the neutron lifetime, τ_n is inversely proportional to the ratio of the proton and neutron rates, $\dot{N}_p/\dot{N}_{\alpha+t}$. Therefore, we must transition from events per run to events per time. To do this we must correct for the difference in the proton trapping time and the neutron detection time. As discussed in section 2.2, this correction is dependent on the trapping time, and for this example we will focus on a nominal 10 ms trapping time. Since there are 10,000 trap openings per run and the proton trapping time is 10,094 μs and the neutron detection time is 10,200 μs per cycle, the proton and neutron event rates are given as:

$$\dot{N}_p(Multi) = \frac{N(Multi)_r}{100.94\,s} \quad (4.13)$$

$$\dot{N}_p(Poi) = \frac{N(Multi)_r}{100.94\,s} \quad (4.14)$$

$$\dot{N}_{\alpha+t} = \frac{N_{(\alpha+t)r}}{102.0\,s}. \quad (4.15)$$

These rates are the total detected event rates, which must be corrected by the detection efficiency for each detector.

With the proton and neutron rates now determined, we can obtain the neutron lifetime by plotting $\dot{N}_p/\dot{N}_{\alpha+t}$ as a function of the length of the trapping region. An example of this plot can be seen in figure 4.14. In chapter 5, I will discuss how the neutron detection efficiency is

determined using the Alpha-Gamma device. We cannot determine the neutron lifetime from the slope of equation 2.4 without this efficiency. For quick checks of the neutron lifetime during data taking we can calculate the neutron lifetime similarly to how it was determined in BL1 [67]. Using this method, the neutron lifetime is given by:

$$\tau_n = \frac{M}{2\Omega\sigma v\rho_t N_a m}, \tag{4.16}$$

where M is the atomic weight of ^6Li, Ω is the measured solid angle subtended by the $1/v$ neutron detectors, σ is the neutron capture cross section on ^6Li at defined thermal velocity, v, ρ_t is the areal density of the Li deposit, N_A is Avogadro's number and m is the slope of the lifetime fit as seen in figure 4.14.

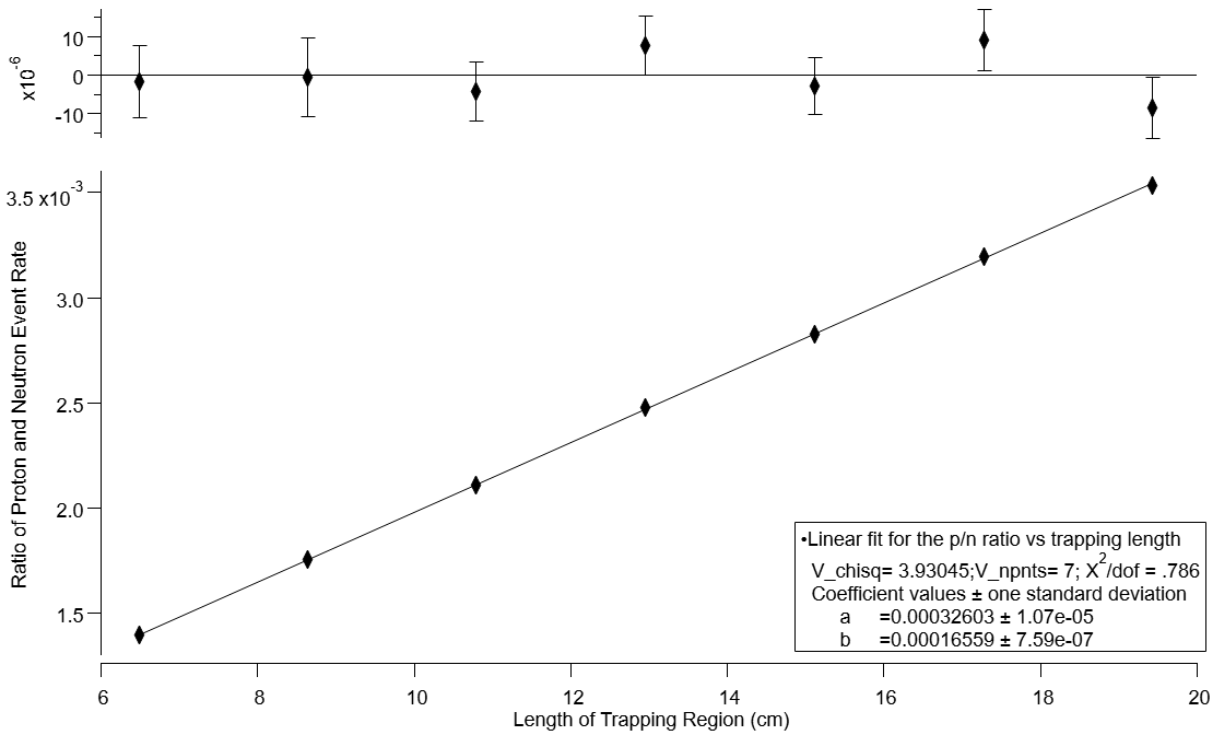

Figure 4.14: Typical neutron lifetime fit showing $\frac{\dot{N}_p}{\dot{N}_{\alpha+t}}$ as a function of trapping length, as in equation 2.4.

Chapter 5

The Precise Determination of Neutron Fluence Using the Alpha-Gamma Technique

The Alpha-Gamma device is used to calibrate the ^6Li deposits used in the $1/v$ neutron fluence monitor. In this chapter, I will discuss this calibration and how the device can also be used to measure neutron capture cross sections at very low energies. The apparatus consists of a practically identical copy of the neutron fluence monitor that is on the BL2 apparatus. This Alpha-Gamma (AG) fluence monitor (FM) is placed upstream of the AG device on the NG-6m beamline at the NCNR. The AG device consists of two HPGe gamma detectors, a Si solid state alpha detector and a target holder placed in the neutron beam. A drawing of the detector arrangements can be seen in figure 5.1.

5.1 The Alpha-Gamma Technique and Apparatus

The Alpha-Gamma technique relies on the neutron capture reaction of 10-Boron, $^{10}B(n,\alpha)^7Li$. The reaction has two relevant branching ratios, one leaves the ^7Li in an excited state, $^7Li^*$, and the other does not. For our purposes the de-excitation occurs immediately, and emits a 478 keV gamma ray [46, 61]. Therefore, the two relevant reactions are an alpha-only reaction

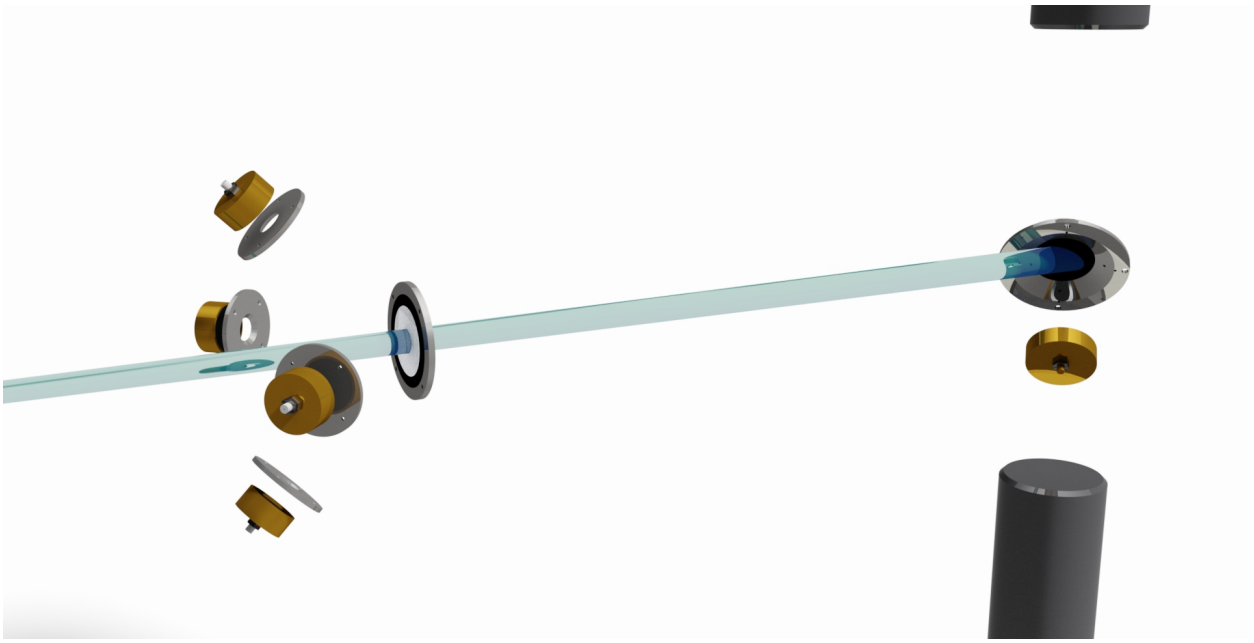

Figure 5.1: Drawing of the Alpha-Gamma device and the FM installed upstream.

(branching ratio b_α= 6.3%),

$$n + {}^{10}B \rightarrow {}^{7}Li(1,015\,keV) + \alpha(1,776\,keV), \tag{5.1}$$

and an alpha+gamma reaction (branching ratio $b_{\alpha\gamma} = 93.7\%$),

$$n + {}^{10}B \rightarrow {}^{7}Li^{*} + \alpha \rightarrow {}^{7}Li(840\,keV) + \gamma(478\,keV) + \alpha(1,472\,keV). \tag{5.2}$$

In the alpha only reaction, the decay products are produced isotropically but in the alpha+gamma reaction, the recoiling ^7Li nucleus has $\frac{v}{c} = 0.016$ which causes a slight anisotropy in the gamma distribution. The total neutron flux is determined using a calibrated gamma detector array. The calibration is performed using a series of high precision transfer calibrations which will be explained below.

The FM calibration has four main parts: (1) the calibration of an alpha source, (2) the measurement of the AG alpha detector efficiency, (3) the measurement of the AG gamma detector efficiency, and (4) the measurement of the neutron flux. (1) The calibration starts with the measurement of a $^{241}Am\,\alpha$ source in a precision machined counting stack (figure 5.2) [35]. The counting stack has three main components: a source holder for repeatable placement of the source, a Si charged particle detector with precision machined aperture, and precision machined spacers to change the distance between the source and the detector. Because of the precision machined components, the solid angle of the detector with respect to the source location is known to better than 0.05%. Using the known solid angle, Ω_{stack}, and the measured α rate in the detector, $r_\alpha(stack)$, the source activity, $R_\alpha(Am)$ is calculated as:

$$R_\alpha(Am) = \frac{r_\alpha(stack)}{\Omega_\alpha(stack)}. \tag{5.3}$$

(2) The ^{241}Am source is then transferred to the AG device where the α rate, $r_\alpha(Am)$ is measured with another Si charged particle detector with a precision aperture as seen in figure 5.2. With the known activity of the source, the efficiency of the AG alpha detector, ϵ_α, is calculated by:

$$\epsilon_\alpha = \frac{r_\alpha(Am)}{R_\alpha(Am).} \tag{5.4}$$

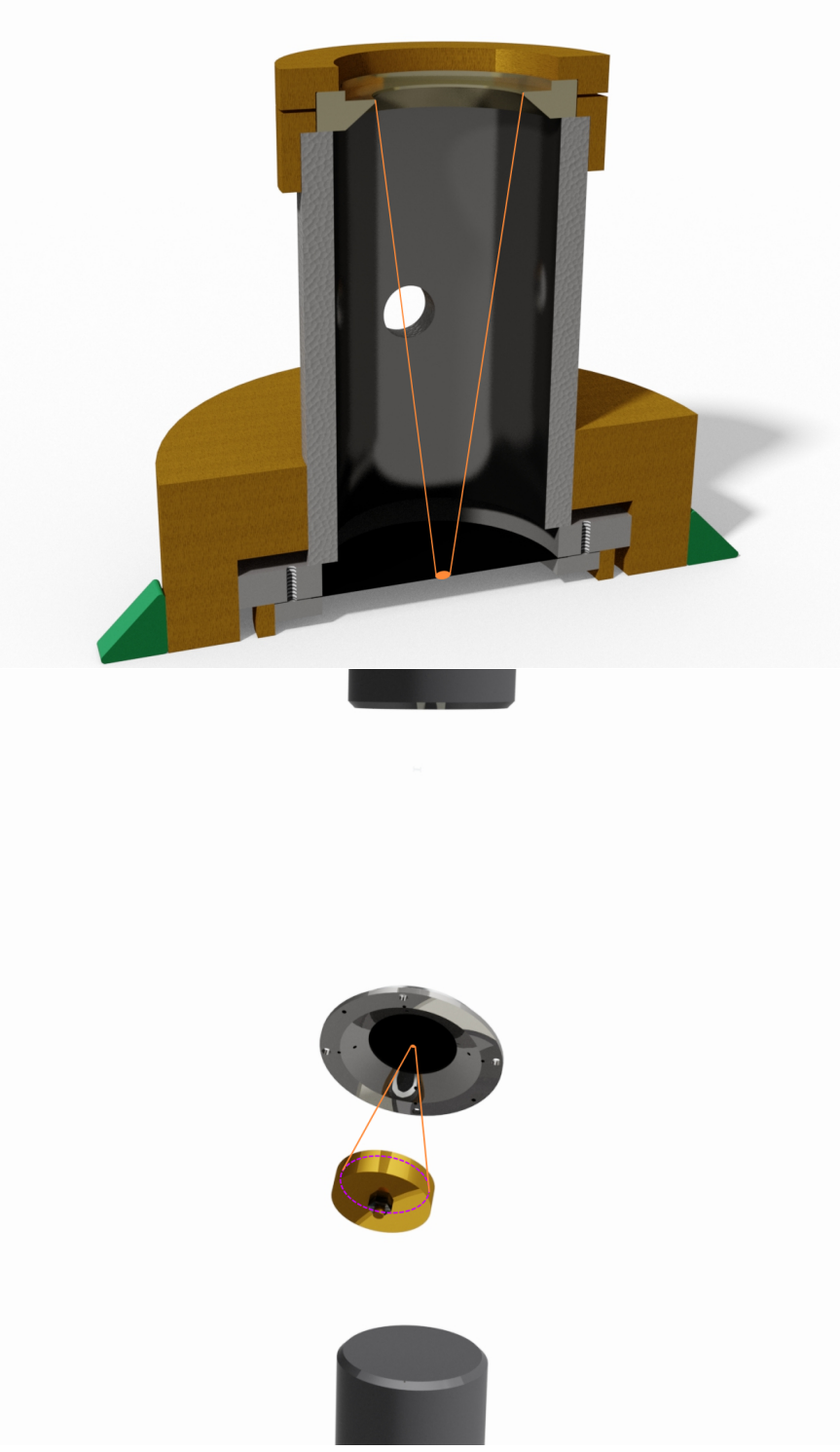

Figure 5.2: Top: assembly of the precision counting stack, traces show the solid angle subtended by the detector, used to measure $R_\alpha(Am)$. Bottom: drawing the Alpha-Gamma device with the ^{241}Am source installed in the holder, traces show the solid angle subtended by the Alpha-Gamma alpha detector, used to measure ϵ_α.

(3) The ^{241}Am is then removed and a "thin" $^{10}B_4C$ foil is then placed in the target holder of the AG device (figure 5.3). The ^{10}B capture cross section is very large for cold neutrons, 10,580 barns for 5 Å neutrons. Therefore, the thin foil is only $\approx 25\,\mu g/cm^2$ of ^{10}B, which is thin enough to cause little attenuation of the alphas from the decay process. With the thin ^{10}B foil in place, the ≈ 5 Å monochromatic neutron beam is turned on and the absorption rate in the thin foil, R, is then determined by:

$$R = \frac{r_\alpha}{\epsilon_\alpha} = r_\alpha \frac{R_\alpha(Am)}{r_\alpha(Am)}. \tag{5.5}$$

With the neutron beam on, there is now a gamma rate from the $^7Li^*$. The measured gamma rate with the thin foil is defined as:

$$r_\gamma(thin) = \epsilon_\gamma b_{\alpha\gamma} R. \tag{5.6}$$

From this we can determine the gamma detector efficiency, ϵ_γ, as:

$$\epsilon_\gamma = \frac{r_\gamma(thin)}{b_\alpha\gamma} \frac{r_\alpha(Am)}{r_\alpha} \frac{1}{R_\alpha(Am)}. \tag{5.7}$$

(4) To determine the total neutron flux, a "thick" ^{10}B target is placed in the AG device (figure 5.3). Because of the large neutron capture cross section of boron, only a few tenths of a millimeter of boron is needed to stop all but a negligible fraction of neutrons from the beam. The total neutron fluence, $\dot{n}_{AG}$ is then determined as:

$$\dot{n}_{AG} = r_\gamma(thick)\epsilon_\gamma \tag{5.8}$$

where $r_\gamma(thick)$ is the measured rate in the gamma detector array with the thick ^{10}B deposit.

The quantities above have been defined with certain assumptions. One is that the detection efficiency in the AG alpha detector is the same for the ≈ 5 MeV alphas from the ^{241}Am decay and the ≈ 2 MeV alphas from the ^{11}B decay. The other assumption is that there is no attenuation in the thin boron deposit for the alpha particles and in the thick boron deposit for the gamma rays. In reality, the attenuation of the gamma rays in the thick boron deposit is about 1-2 %. This is one of the largest corrections in the determination of the $1/v$

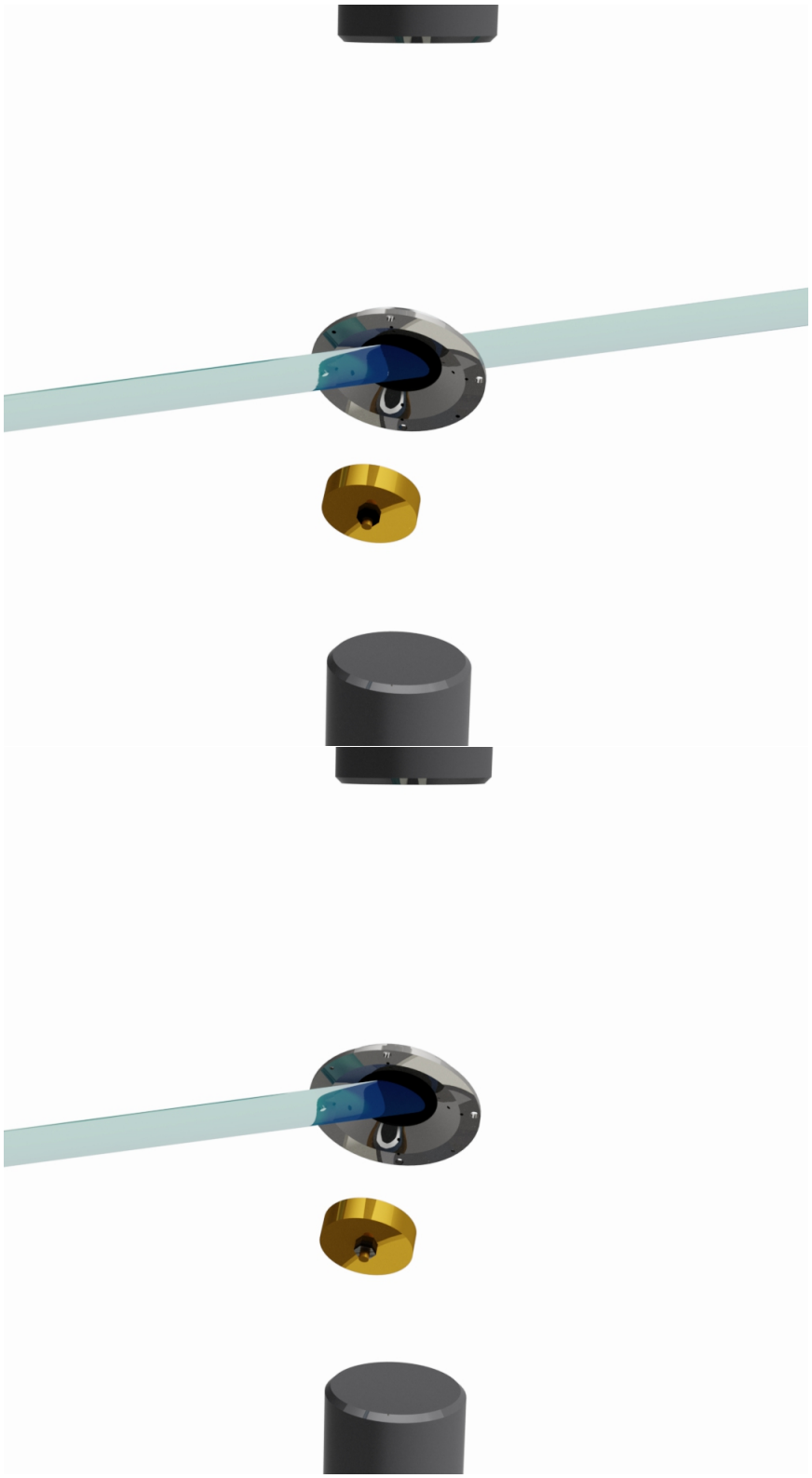

Figure 5.3: Top: drawing the Alpha-Gamma device with the thin boron deposit installed and the neutron beam in blue, used to measure ϵ_γ. Bottom: drawing of the Alpha-Gamma device with the thick boron deposit installed and the neutron beam in blue, used to measure r_γ.

neutron detector efficiency. For a more detailed discussion of assumptions and corrections made in determining the gamma detection efficiency, see the dissertation of Andrew Yue [107].

Because the cross section is $1/v$ dependent, it is important to make this measurement with a monochromatic neutron beam. For this reason, the experiment is done on the NG-6m beamline at the NCNR [31]. The NG-6m beamline has a pyrolytic graphite monochromator placed in the beam to Bragg reflect neutrons of approximately 0.496 nm ($\approx$ 5 Å) in wavelength. The reflected beam is then sent through a beryllium block that is cooled to 77 K by a liquid nitrogen bath. This block filters out higher order Bragg reflections from the graphite monochromator. To measure the neutron wavelength on NG-6m, λ_{6m}, a perfect silicon crystal is placed in the beam just before the $1/v$ neutron monitor. When the crystal is placed at the correct angle, θ_B, the Bragg conditions are met. The crystal reflects the neutrons at a known angle where ^3He proportional counters are placed to track the reflected neutron rate. With the approximate neutron wavelength known from the graphite monochromator, the approximate Bragg angle can be determined with

$$n\lambda_{6m} = 2dsin\theta_B, \tag{5.9}$$

where n is the diffraction order, and d is the lattice spacing of the Si crystal. Using the approximate Bragg angle, the Si is then rotated over the appropriate range (typically 2-3 degrees from the center of the Bragg peak) so that a peak may be fit. An example of this scan may be seen in figure 5.4, taken from reference [107]. From this scan, θ_B was determined to be $52.279° \pm 0.017°$, which corresponds to $E_n = 3.3155 \pm 0.0016\, meV$.

5.2 Absolute Neutron Fluence Calibration

As discussed in section 2.2, the determination of the $1/v$ neutron fluence monitor efficiency, ϵ_0, was the limiting systematic uncertainty in the BL1 result. With the use of the AG device, an independent, absolute calibration of the $1/v$ neutron fluence monitor is now possible without reliance on the ^6Li neutron capture cross section. To extract ϵ_0, once

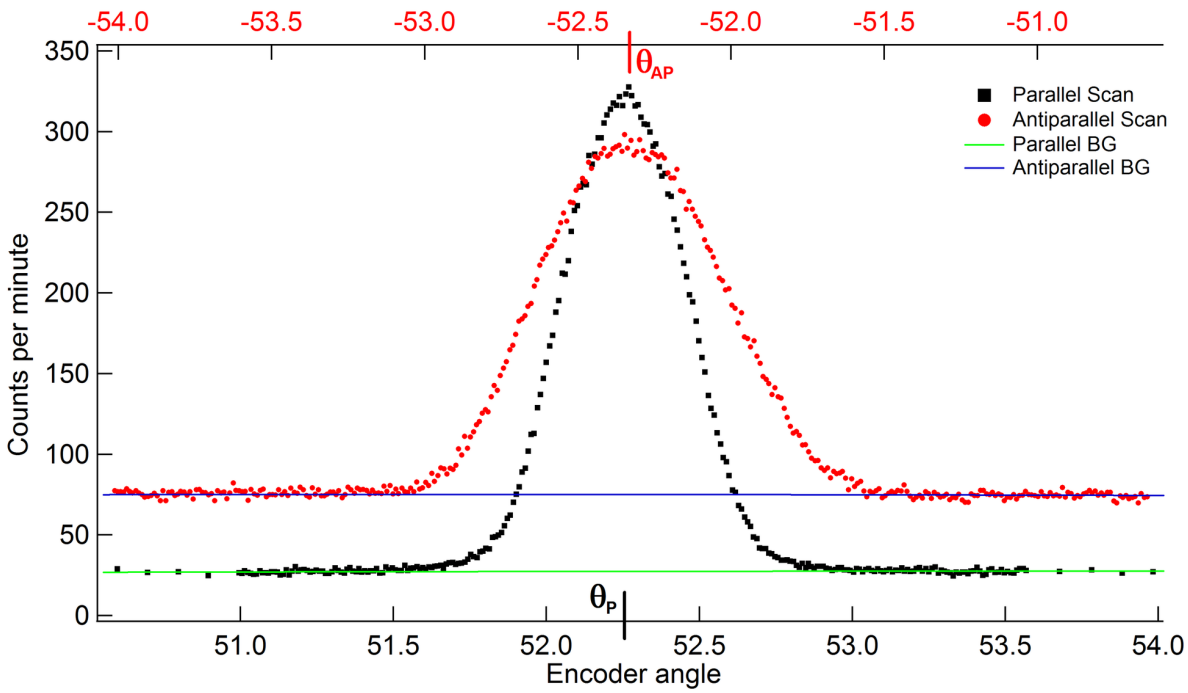

Figure 5.4: Typical scan of the silicon crystal angle resulting in a peak when the Bragg conditions are met, taken from reference [107].

ϵ_γ is determined, is straightforward in principle and is defined as:

$$\epsilon_0 = \frac{\dot{n}_{FM}}{\epsilon_\gamma \dot{n}_{AG}} \tag{5.10}$$

where $\dot{n}_{FM}$ is the detected rate in FM. If the efficiencies of all the detectors are constant, then a simple average over high statistics measurements would yield a $< 0.05\%$ relative measurement in approximately 8 days with the limiting factor being the 6 Hz count rate in the FM. However, in the previous running of the AG device it was discovered that the ratio of the gamma detector rate and FM rate was not constant in time. A 0.07%/day linear shift was seen in the previous running that needs to be accounted for [107]. It is believed that this change in efficiency is not due to a gain shift in either detector, but a physical change in the fundamental efficiency in the device. For the result to be trusted, ϵ_γ must be the same for the thin boron deposit calibration as for the thick boron deposit data taking. To account for the drift, a method of book-ending the thick boron data taking runs by two thin boron deposit calibrations was developed. This so-called "triplet" method takes one day of data with the thin deposit, one day with the thick deposit, followed by a second day of the thin deposit. This allows for the two thin deposit calibrations to be fit to a linear function in time, and then ϵ_γ is taken to be the midpoint of this fit. This method significantly increases the runtime needed for a $< 0.05\%$ relative measurement but increases the robustness of the technique.

There are two main components to the calibration of the neutron fluence monitor, ϵ_0 is a function of both the FM detector array solid angle and the ^6LiF deposit areal density. Using the same calibrated ^{241}Am source from the calibration of the AG device, the solid angle of the FM detector array can be measured. This is critical because two FM vacuum cans exist. One is installed upstream of the AG device, rig 1, and the other is downstream of the BL2 magnet and proton trap, rig 2. When ϵ_0 is determined for the FM installed on the AG beamline that ϵ_0 is valid for a specific ^6LiF deposit in a specific rig. A small correction factor must be used when a calibrated foil is transferred to the BL2 apparatus for data taking. The solid angles of the two rigs have been measured to a 0.04 % relative precision [108].

5.3 Absolute measurement of Neutron Capture Cross Sections

In addition to being used to calibrate the BL2 neutron fluence monitor, the alpha-gamma device can be used to measure neutron capture cross sections in a much lower energy regime than other cross section measurements. In particular, the $^6Li(n,t)^4He$ neutron capture cross section is critical for neutron fluence determinations in measurements of other cross sections. The standard energy range used in this type of cross section is 25.3 meV (thermal) to 1 MeV. However, most cross section measurements have been made at energies far greater than thermal energy [26]. The previous measurements at or near thermal energy have been limited to integral-type measurements [66], measurements of the difference between the total and scattering cross sections [9], or measurements of the ratio of cross sections [25]. No absolute measurement of the $^6Li(n,t)^4He$ cross section has been made at energies close to thermal energy. At energies less than 50 keV, the $^6Li(n,t)^4He$ cross section has been shown to deviate from the $1/v$ law by less than 0.01% [11], therefore extrapolations from higher energies are straightforward to make. However, the beam energy on the NG-6m beamline has been measured to be (3.3255 $\pm$ 0.0016) meV [107], which would be the lowest energy measurement of the $^6Li(n,t)^4He$ cross section by almost a factor of ten.

The measurement is made by relating the total neutron flux in the Alpha-Gamma device with the totally absorbing boron target, $\dot{n}_{AG}$, to the total neutron induced events in the FM thin ^6Li deposit, $\dot{n}_{FM}$. The energy dependent efficiency is then given by:

$$\epsilon(E_n) = 2\sigma(E_n)\Phi, \tag{5.11}$$

where the factor of two comes from the double counting of alpha and tritons due to the nature of the detector array, $\sigma(E_n)$ is the energy dependent cross section, and Φ is a quantity that depends on the neutron monitor solid angle, the areal density of the ^6Li deposit and the neutron beam profile similar to how the neutron detection efficiency was determined in the

BL1 experiment. Φ is given by:

$$\Phi = \frac{N_A}{A} \int \int \Omega(x,y)\rho(x,y)\phi(x,y)dxdy, \tag{5.12}$$

therefore, the cross section is given by:

$$\sigma(E_n) = \frac{\dot{n}_{FM}}{\dot{n}_{AG}} \frac{1}{2\Phi}. \tag{5.13}$$

The determination of the areal density of the ^6Li deposits has been discussed previously [84, 73, 47]. The deposits were manufactured by the Institute for Reference Materials and Measurements (IRMM) in Geel, Belgium, and their relative densities were determined with a thermal neutron beam at the BR1 reactor in Mol, Belgium [83]. The deposit's profile shape and edge quality were measured with spectrophotometry and a Talystep measurement respectively [73]. These measurements were then compared to the calculated profile from the known construction geometry and found to be consistent. The absolute ^6Li mass was then determined by sacrificing two of the fabricated deposits with a destructive isotope dilution mass spectroscopy (IDMS) measurement done by the IRMM. We currently plan to sacrifice another of the measured deposits for a second round of IDMS carried out at NIST to verify the mass of ^6Li has not changed in the last 30 years. It is also planned that the profile of the deposits be re-measured at NIST using ellipsometry. Data taking is ongoing for this measurement but it is believed that a relative precision of $< 0.3\%$ on the $^6Li(n,t)^4He$ neutron capture cross section at sub-thermal energy can be achieved.

Similarly to the $^6Li(n,t)^4He$ cross section measurement, a $^{235}U(n,f)$ neutron capture cross section measurement is currently underway. This measurement is similar to the previously discussed ^6Li measurement except where the $^6Li(n,t)^4He$ reaction has ≈ 5 MeV of excess energy the $^{235}U(n,f)$ carries ≈ 211 MeV of energy. Of this 211 MeV, about 169 MeV is carried by the fission products. This means that the dynamic range of the FM must be much larger for this cross section measurement. Yet another complication is the multi-body decay of the ^{236}U. Because the $^6Li(n,t)^4He$ reaction is a two body decay, the products have fixed energies. This allows for the analysis to look in a very particular energy window. For the $^{235}U(n,f)$ fission products, the energy range is much larger, which makes

the analysis more difficult. Another difference between the ^6Li and the ^{235}U measurements is the presence of multiple isotopes in the ^{235}U deposit. While there is also ^7Li present in the ^6Li deposit, the ^7Li is stable and does not complicate the analysis (it does complicate the mass determination). However, the ^{235}U deposits contains a fraction of ^{234}U. This ^{234}U alpha decays with a lifetime of 2.46×10^5 years and energy of 4.8 MeV and occurs with or without the neutron beam. Because the solid angle of the detector array is known, the total mass of the deposit may be determined if the ^{234}U alpha rate and the relative mass fraction is known. This measurement also requires knowledge about the deposit shape, which will be measured using X-ray Fluorescence at NIST. Similarly to the ^6Li measurement, the energy range used in this experiment is far from any neutron capture resonances and is in a region that is almost purely $1/v$. This measurement is ongoing and the estimated relative precision is commensurate with the $^6Li(n,t)^4He$ measurement.

Chapter 6

Assessment of Systematic Tests and Corrections

This chapter will discuss experimental aspects that have the potential to modify the measured neutron lifetime and may require a correction to the final result. As a systematics limited experiment, the majority of data is collected for different systematic tests. This chapter will outline the systematic tests that have been carried out for BL2, but is not as an exhaustive list of all possible systematic effects in this experiment.

6.1 Magnetic Field Corrections

If the proton trap is perfectly symmetric and the magnetic field is perfectly uniform, the end region, L_{end}, is exactly the same for all trapping lengths, and the lifetime fit, from equation 2.4, will be perfectly linear. In reality, small differences in electrode sizes, small misalignments of the electrodes, the neutron beam divergence, and the magnetic field nonuniformity across the trapping region cause slight deviations to this fit. As a result, a correction is necessary for all trapping lengths. The electrostatic potential of the trap electrodes can be calculated to an accuracy of better than 0.02% using an approximate solution to Laplace's Equations for axially symmetric lenses [20]. Due to the physical open cylinder-like shape of the electrodes, there is some radial dependence to the potential. On the center axis of the trap electrodes, the trapping potential is slightly lower, and that potential

increases closer the electrodes. Figure 6.1 shows the potential shape for a 3 electrode trapping region on the left and the radial dependence of the potential distribution as a function of radius on the right.

Because the trapping potential is not perfectly square shaped, a decay proton can be born at a positive potential in the end regions and still be trapped. In this case, a proton is trapped if its axial kinetic energy and electrostatic potential energy is less than the maximum of the trapping potential. Because of this, protons born in the end region are trapped with less than 100% efficiency. A small correction is applied to the trapping lengths to account for these effects. The nonuniformity in the magnetic field dominates these corrections.

The trapping region acts as a quasi-Penning trap, however, it is not a true Penning trap because it lacks an axial quadruple electrostatic field. The same basic particle modes exist:

1. An axial "bounce" along the axis of the beam with period T_z.
2. Cyclotron motion around the magnetic field lines with period $T_c = \frac{2\pi m_p}{eB}$.
3. Magnetron drift motion perpendicular to the magnetic field lines that is proportional the $\vec{E} \times \vec{B}$ force. Since the electric and magnetic fields are almost solely axial, this force is small and this motion can be ignored [67].

For a charged particle moving in a magnetic field, it can be shown that $\frac{p_\perp^2}{\vec{B}\cdot\vec{l}}$ is an adiabatic invariant; where $\vec{l}$ is the vector along the guiding center of the proton (the axial center of the helical proton trajectory), and $p_\perp$ is the proton momentum perpendicular to $\vec{l}$ [56]. It can also be shown that the adiabatic conditions are satisfied everywhere in the trapping region [67]. If one defines the longitudinal kinetic energy along the guiding center to be K_l, then a variation in the magnetic field, $\vec{B}$, along $\vec{l}$ will cause a change in K_l. The dot product, $\vec{B} \cdot \vec{l}$, acts as a one-dimensional scalar potential that is proportional to the energy of the proton. This quantity is treated as a magnetic pseudo-potential. The magnetic pseudo-potential for a proton's trajectory can be expressed as a voltage that is a function of the guiding center. A proton's initial pseudo-potential can be defined as zero, then the change in pseudo-potential is added to the electrostatic potential along the proton's trajectory. Therefore, a proton is trapped if the sum of the axial kinetic energy and electrostatic potential at birth is less than the sum of the electrostatic potential plus the magnetic pseudo-potential at every point along the proton's path. The nominal trapping potential (800 V) is high enough and the

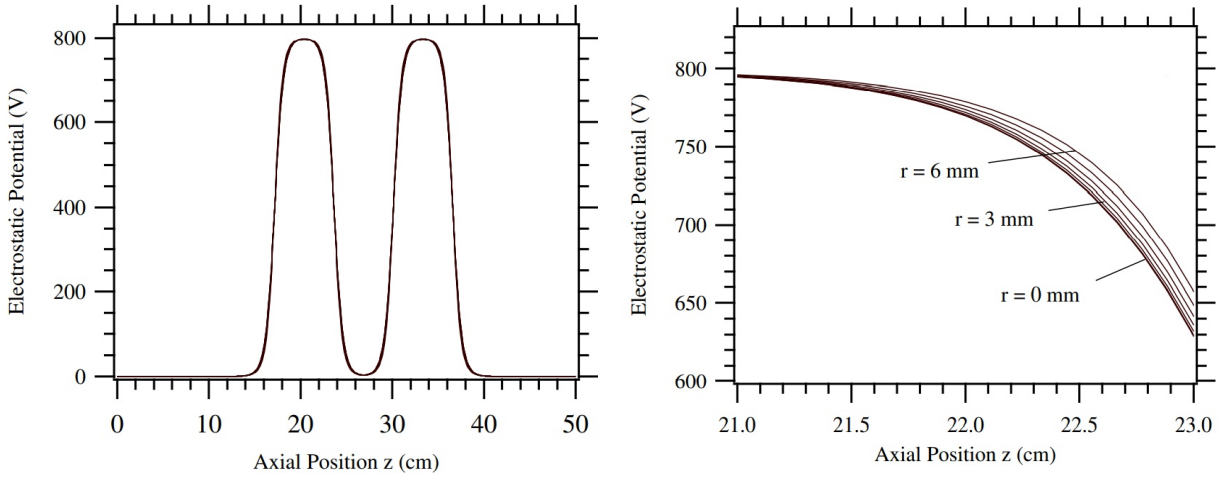

Figure 6.1: Left: electrostatic trapping potential for 3 electrodes and 800 V, showing the trapping potential shape. Right: radial dependence of the electrostatic trapping potential, taken from [67].

maximum value of the magnetic pseudo-potential variation is small enough (≈30 V) that all protons born in the grounded center region are trapped.

If a proton is born in the end region of the trap, at an elevated electrostatic potential, the trapping probability will depend on the magnetic pseudo-potential along the proton's trajectory. Since the magnetic field is not uniform over the entire trapping region, and data are taken at many different trapping lengths, this probability is not constant for all trapping lengths. Figure 6.2 shows the magnitude of the axial magnetic field in relation to the placement of the trapping electrodes. In the normal data taking mode, the door electrodes are kept fixed but the mirror electrodes are moved up and downstream to increase or decrease the trapping volume. These effects cause the neutron lifetime to be slightly non-linear as a function of trapping length, and a correction factor must be applied to each trapping length to account for this. At a much smaller level, these correction factors to the electrode lengths will also depend on the divergence of the neutron beam in the trapping region, and variations in electrode and spacer length. For a more detailed descriptions of these smaller effects see reference [67]. These electrode length corrections depend on the exact placement of the Mark II and Mark III traps in the magnet bore and will be calculated after data taking is finished.

To verify this calculation, data needs to be taken so that the magnetic field nonuniformity is minimized for a particular apparatus configuration. Data was taken with a 3 electrode scan of the trapping region. 3 electrodes is the smallest trapping region that is usable because a smaller trapping region causes the end regions to overlap. Data was taken at 7 different trapping regions, in 3 electrode segments, starting with electrode 4 and ending with electrode 13. Because the magnetic field strength is highest at the middle trapping electrodes, and lower at the door and for downstream positions of the mirror, protons born in the end region are more likely to be trapped when using 6 or 7 electrodes, for example, and less likely to be trapped when using the most extreme cases of a short or long trap, 3 and 10 electrodes respectively. Because protons are trapped further away from the proton detector the more downstream the trapping region, some care must be taken in the analysis to insure that all trapped protons are counted. The most highly energetic protons still arrive at the proton detector almost immediately no matter the trapping location. However, low energy protons

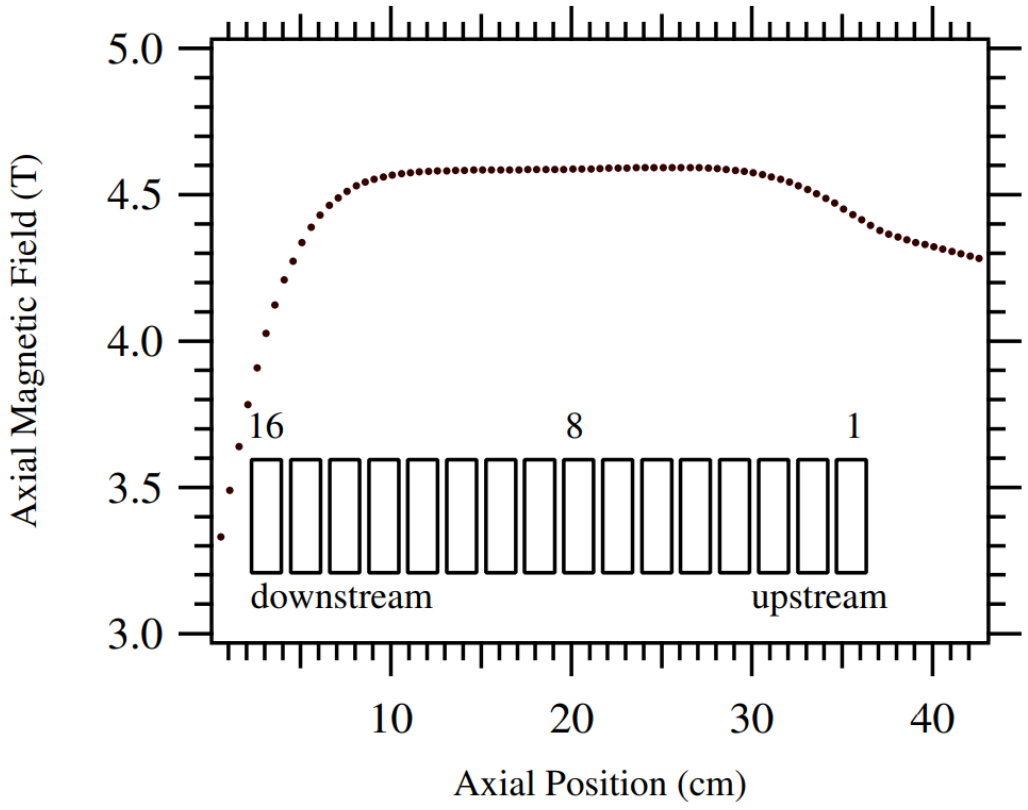

Figure 6.2: Measured axial magnetic field strength showing the position of the Mark II trap electrodes, taken from [67].

that are kicked out of the trap by the ramp can take up to 7 μs longer to reach the detector from the most downstream trapping region compared to the normal trapping position. Figure 6.3 shows an example of the arrival time of the protons for different sections of the trap. This data allows the Monte Carlo, which is similar to the Monte Carlo described in section IV-C of reference [67], be experimentally verified and gives confidence in both the measurement of the magnitude of the magnetic field and the Monte Carlo. The Monte Carlo has many test cases, but generally a comparison is made between the number of trapped protons with a perfectly uniform magnetic field and the measured magnetic field. The difference between these two provides a correction to the trapping length. Figure 6.4 shows a comparison between the $\frac{\dot{N}_p}{\dot{N}_{\alpha+t}}$ ratio for different 3-electrode segments of the trap compared to the expected variation due to the known magnetic field shape assuming a rough placement of the trap. The good agreement between the data and the calculation shows that the magnetic shape is well understood and can be easily corrected. In BL1, a significant portion of the data was taken with 10 central trapping electrodes. In this configuration, the magnetic field varied more than was expected and led to a large, -5.3 s, correction to the neutron lifetime. BL2 plans to take data only up to 9 central trapping electrodes, we believe this should decrease the correction to the $\sim 1\,s$ level. Moreover, because the magnetic field was changing quickly in the vicinity of 10th trapping electrode, the axial placement of the trap had a relatively large effect on $\frac{\dot{N}_p}{\dot{N}_{\alpha+t}}$, leading to systematic uncertainty of $\pm 0.71\,s$. Now, only using up to 9 trapping electrodes and axially positioning the trap using the trap positioning piece mentioned in section 2.2, the uncertainty in the trap position and the sensitivity to that position will be significantly decreased to the $\approx \pm 0.2\,s$ level.

6.2 Proton Trap Unloading Efficiency

Decay protons in the trapping region must be transported to the proton detector with near unit efficiency to minimize a necessary correction to the neutron lifetime. To guarantee proper unloading of the proton trap, a small gradient potential is placed on the previously grounded central electrodes. This gradient, the ramp, forces protons with low axial kinetic energy out of the trap and into the acceleration potential of the proton detector. Because of

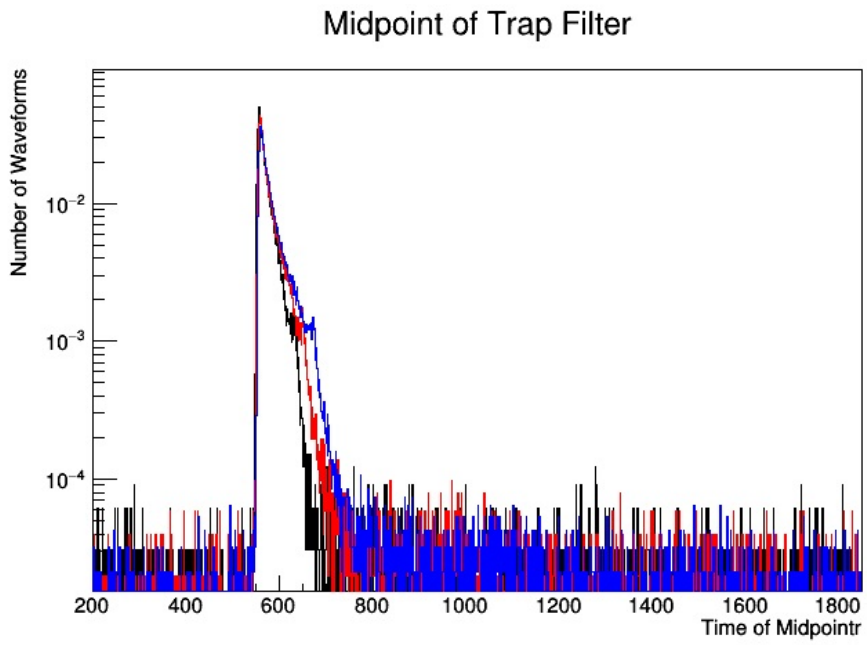

Figure 6.3: Comparison of proton arrival times for 3 electrode trapping regions, showing that protons trapped further downstream can take longer to reach the proton detector. Red: trapping electrodes 4-6, black: trapping electrodes 7-10, blue: trapping electrodes 11-13.

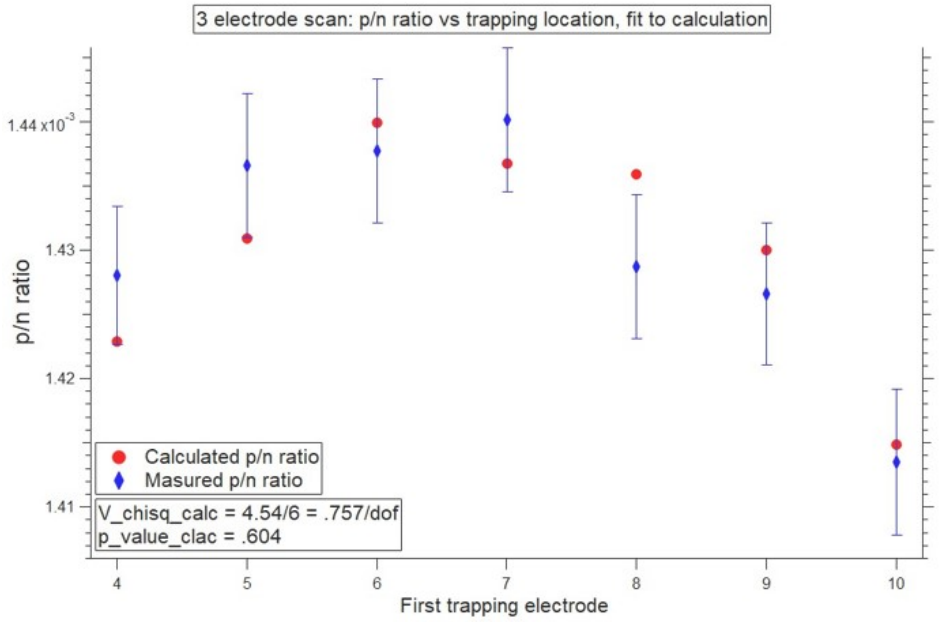

Figure 6.4: Comparison of 3 electrode scan of trapping region with calculation taking into account the change in the magnetic field strength.

the trapping potential of the door and mirror, protons in the trap have axial kinetic energies ranging from 0 to 800 V. If there was no ramp voltage placed on the grounded electrodes, low axial energy trapped protons could take an indefinitely long period of time to reach the proton detector. This would require an open ended arrival time window in the analysis which would cause an unnecessary decrease in the signal to background ratio. Because the detector signal is digitized for only a small portion of the trapping cycle the ramp must be sufficiently high so that the slowest possible protons arrive within this digitization window. It is preferable that protons arrive much earlier than the end of the digitization window because the analysis is most efficient if the whole exponential decay tail preamp waveform can be seen. As a systematic test of the proton trap unloading efficiency, data was taken varying the maximum ramp voltage between 0 and 60 V. One would expect that above a certain cut off voltage the $\frac{\dot{N}_p}{\dot{N}_{\alpha+t}}$ ratio would plateau for a fairly wide range of ramp voltages. As seen in figure 6.5, a reasonable plateau is achieved anywhere between 14.4 and 60 V, and the $\frac{\dot{N}_p}{\dot{N}_{\alpha+t}}$ ratio was significantly lower with no ramp voltage. 14.4 V was the most common ramp voltage during the running of BL1. For BL2, it was decided that the ramp voltage be increased so that the proton arrival time window in analysis could be narrower. This increases the signal to background ratio. The power supply used for the ramp voltage was not able to supply the current necessary for voltages > 60 V. As a result most of production data taking the ramp voltage was set at 45 V. This is far enough away from the current limit that we did not have to strain the power supply. It is believed that for a range of maximum ramp voltages between 14.4 and 45 V, there will be no correction necessary to the neutron lifetime caused by the unloading efficiency of the proton trap.

6.3 Proton Trapping Efficiency

Decay protons have a maximum energy of 751 eV, so the trapping potential must be at least 751 V to completely trap the whole decay proton energy spectrum. The most useful trapping potential is one that is large enough to completely trap the protons while being as low as possible to avoid any problems with instability that may arise with high voltages. The nominal trapping potential used in this experiment has been 800 V. To verify that 800

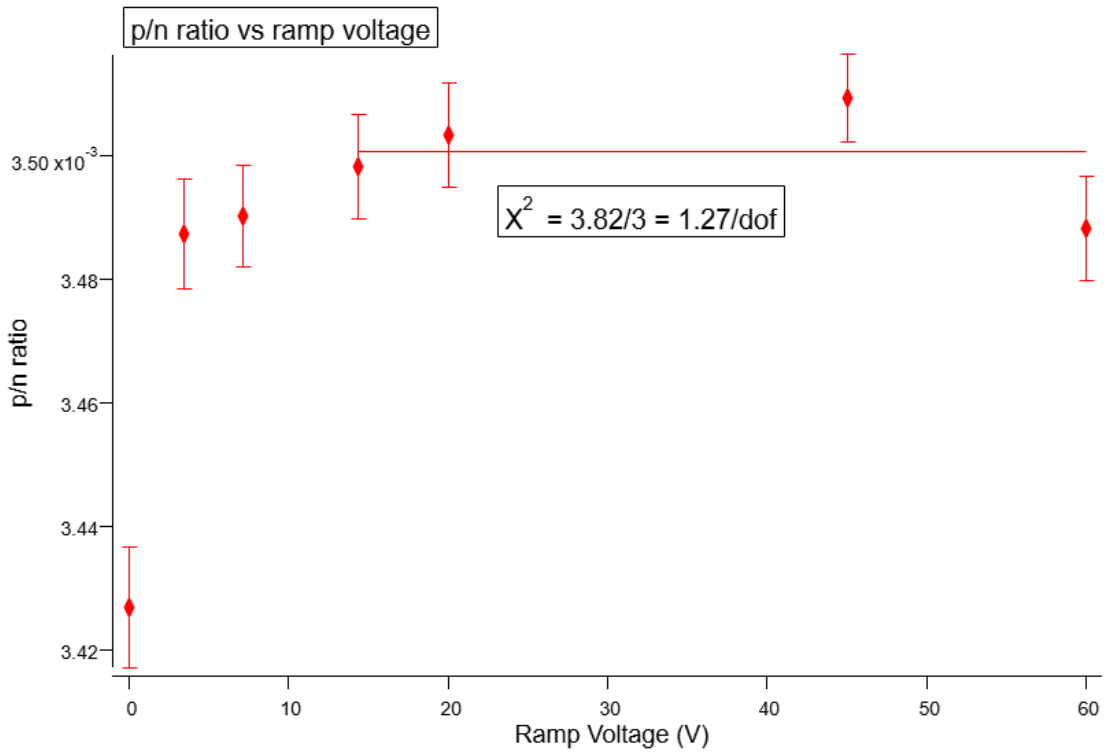

Figure 6.5: Example of $\frac{\dot{N}_p}{\dot{N}_{\alpha+t}}$ vs ramp voltage showing a large plateau in rate for ramp voltages $> 14.4V$.

V is sufficient, data was taken varying the trapping potential between 200 and 1100 V. It is expected that the measured neutron lifetime is constant from 800 to 1100 V and below 800 V the measured lifetime increases in a predictable way. To compare to the data, a GEANT4 simulation was done using the measured magnetic field and electrode sizes.

Because the central trapping electrodes are kept at 0 V the electrostatic potential gradient between the energized electrodes and the central electrodes changes as the applied voltage changes. Higher trapping potentials increase this gradient and functionally increases the proton trapping volume and changes the end region. Because of this, the $\frac{\dot{N}_p}{\dot{N}_{\alpha+t}}$ ratio for each trapping potential also changes, which means the neutron lifetime must be compared for this systematic test, which significantly increases the necessary run time. Data was taken with two different electrode lengths and 14 different trapping potentials between 200 and 1100 V. With two electrode lengths, the neutron lifetime is proportional to the difference in the $\frac{\dot{N}_p}{\dot{N}_{\alpha+t}}$ ratio which makes comparison to simulation much simpler. Doing the systematic test at only two trapping lengths also significantly decreases the amount of time needed for data taking and simulation.

The GEANT4 simulation was done using the results of neutron beam transport simulations to weight the starting positions of protons. The proton energies are sampled from the decay energy spectra ranging from 0 to 751 eV with randomized momenta. These protons are born at axial positions covering the whole trapping region plus some extent outside of the trapping region to replicate the real neutron beam decays. Realistic electric and magnetic fields are also included in the simulation. The axial magnetic fields are taken from previous measurements of magnetic field. The electrostatic potential is calculated with COMSOL using realistic electrode geometries. The simulation is done for three and nine electrode trapping lengths. After the initial proton positions are determined, the proton tracks are evolved for enough time so that the vast majority of protons make multiple bounces back and forth off of the door and mirror potentials. After this run time, the number of protons that are still trapped is tallied. The neutron lifetime is proportional to the difference in the trapped proton fraction between the 9 and 3 electrode simulation. This same set of simulations was then repeated for many trapping potentials ranging from 200 to 1600 V. As seen in figure 6.6, the simulation shows the expected increase in proton rate (here proton

rate is perfectly analogous to the $\frac{\dot{N}_p}{\dot{N}_{\alpha+t}}$ assuming constant neutron fluence) ratio for both the three and nine electrode cases above 800 V. The fast drop of the proton rate is also seen when the trapping potential is below the proton endpoint energy. Although the proton rate is expected to increase because of the effective change in the trapping length, the neutron lifetime is expected to remain constant (neglecting any small changes in the magnetic field in the end region). Figure 6.7 shows the simulated data fit from 700 - 1600 V with a linear function, the resulting slope is consistent with 0. It may also be noted that there is not a significant increase to the neutron lifetime with only a 700 V trapping potential. Only 2% of all protons are born with total kinetic energy $>$ 700 V, but axial kinetic energy is required to escape over the trapping potential. From the simulated data we see that 800 V is sufficient to trap all decay protons, and we should see a constant neutron lifetime with a trapping potential from about 700 V to much greater than 1000 V. Figure 6.8 shows a wide range of data taken between 200 and 1100 V door/mirror voltage. As expected, the measured neutron lifetime increases quickly as the trapping voltages drop below the end point energy of the decay protons and a large plateau is achieved for trapping voltages greater than 700 V. From the simulation, it can be seen that we are not able to detect an increase in the neutron lifetime until the trapping voltages are below $\approx 700\,V$. To show this, the inset of figure 6.8 shows a fit to the measured lifetime from 700 to 1100 V, as expected; this data shows no change in the neutron lifetime over this range. As a result, the nominal trapping voltage of 800 V is sufficient to trap all decay protons born in the central grounded region and no correction is expected for this effect.

6.4 Proton Detector Alignment

Because of the absolute counting nature of the experiment, detector alignment with the neutron beam must be treated carefully or trapped protons may miss the detector. The neutron beam has a 7 mm diameter collimator (C2) directly upstream of the superconducting magnet, and a 25.4 mm diameter collimator (C1) approximately 5.5 m upstream. From this we can calculate that the extent of the neutron beam is $<$ 9 mm in radius at all points in the trapping region. Using the proton end point energy of 751 eV and the 4.6 T magnetic field in

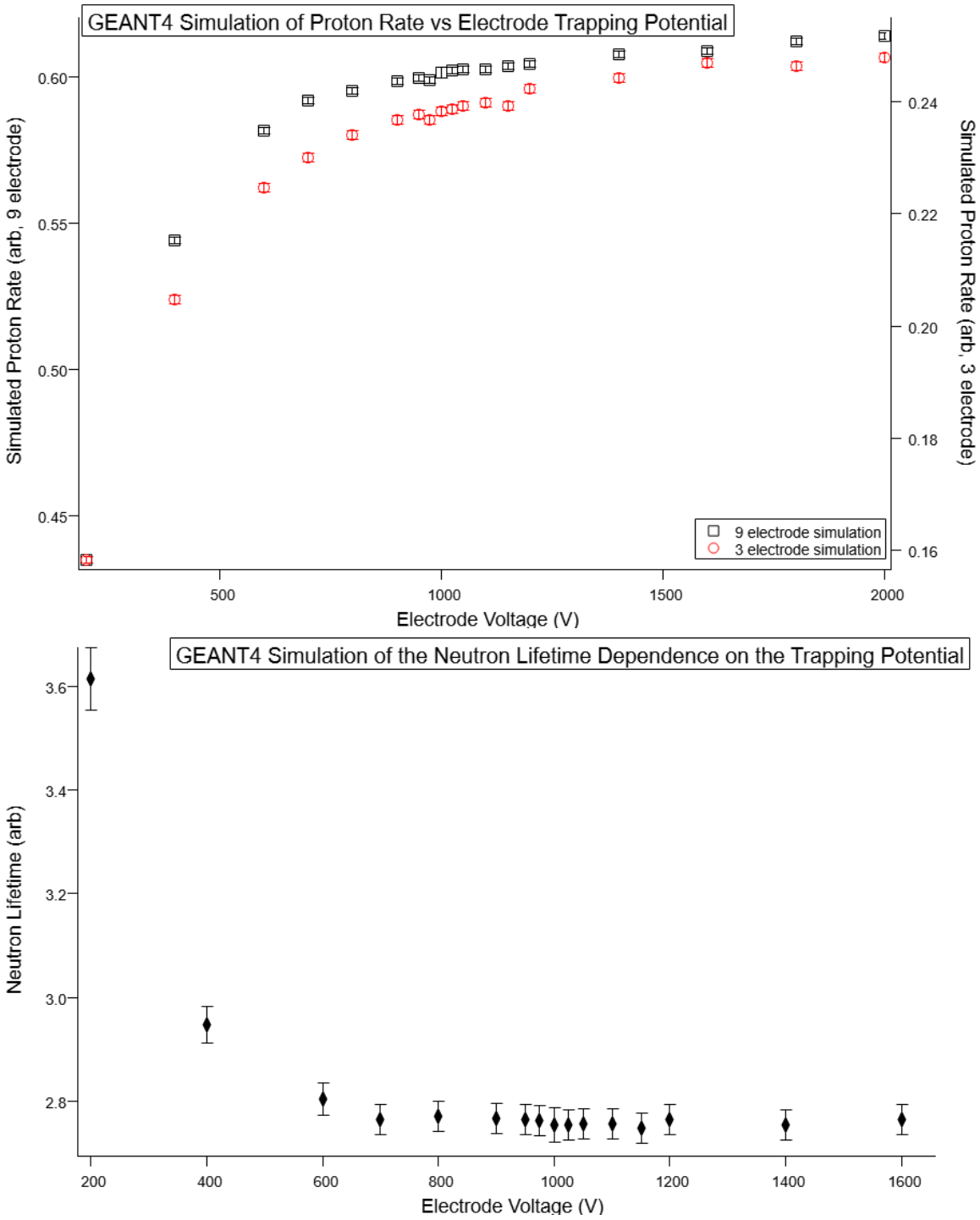

Figure 6.6: Top: Simulated dependence of the proton rate as a function of door and mirror voltage, the increase in rate above 800 V comes from the change in L_{end}. Bottom: Simulated dependence of the neutron lifetime as a function of door and mirror voltage.

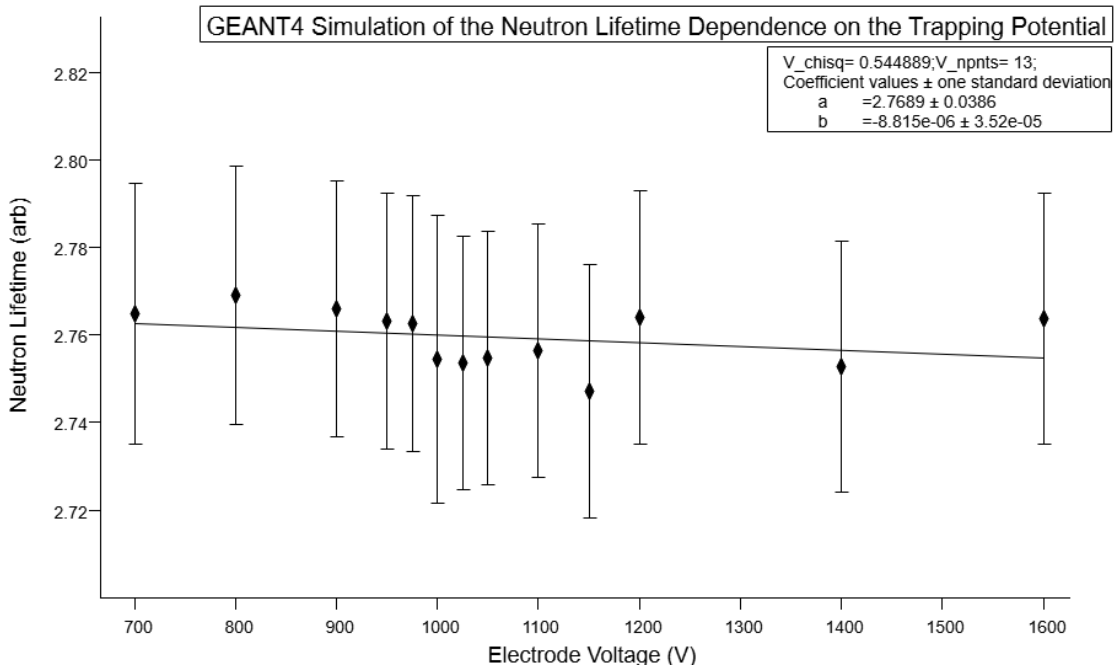

Figure 6.7: Simulated dependence of the neutron lifetime as a function of door and mirror voltage. Simulated data from 700 to 1600 V fit with a linear function. Fit slope is consistent with 0, showing that no neutron lifetime dependence is expected for these trapping potentials.

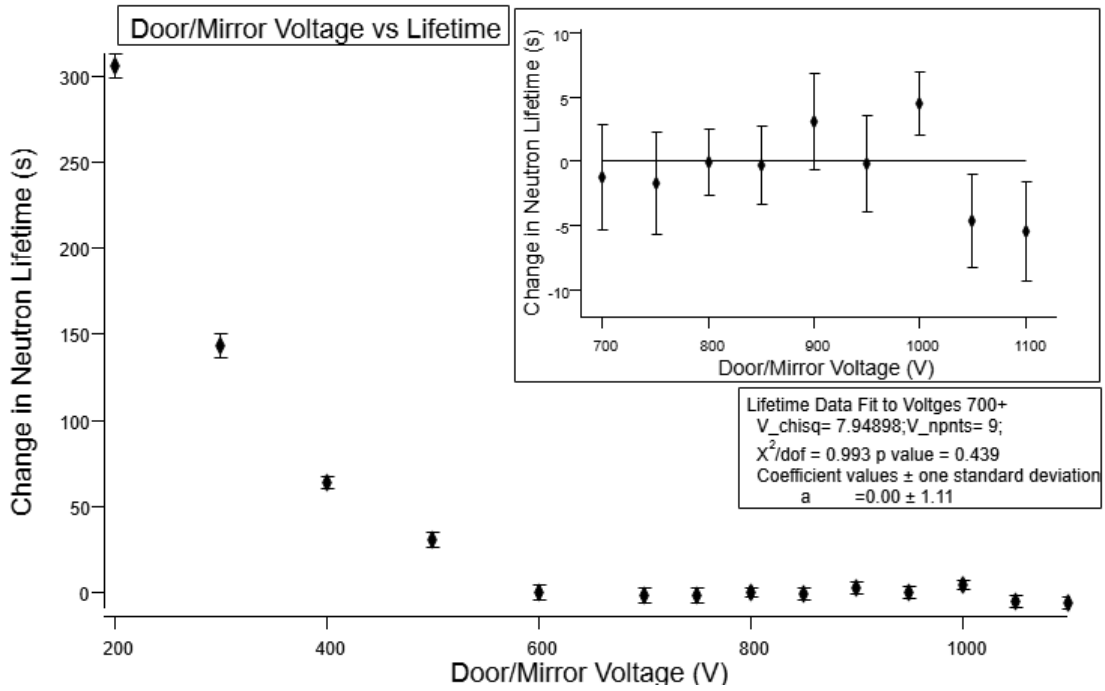

Figure 6.8: Measured lifetime data as a function of door and mirror voltage. Inset shows the data from 700 to 1100 V fit to a constant.

the trapping region, the maximum cyclotron radius of the protons is $< 0.9\,\mathrm{mm}$. Combining these two, the full extent of the proton distribution is slightly less than 10 mm in radius. The smallest detector that could be used for lifetime data is a $300\,\mathrm{mm}^2$ detector with a radius of 9.77 mm. To achieve a negligible amount of missed protons, $< 0.1\,s$ effect on the neutron lifetime, the proton detector must be aligned to better than 1 mm to the neutron beam center. To align the proton detector a theodolite is placed downstream of the apparatus. This theodolite is aligned to the neutron beam center using precisely placed beam markers on the floor and shielding walls. The height of the beam is found using beam markers on the shielding, as well as the magnet flange, and the horizontal position and the angle of the beam is found using multiple beam markers on the floor of the guide hall. The proton detector mount is attached to two encoder motors that are controlled by the DAQ. These motors allow the detector to be moved in the X-Y plane normal to the incoming protons. When the theodolite is aligned, the proton detector position is then centered to this alignment using the encoder motors. The location of the proton detector is now defined as (0,0) on the encoder motors in the X-Y plane. Because of space restrictions caused by the vacuum and high voltage systems, the detector is only able to move a few mm in any direction before it would run into a wall. The DAQ was programmed so that this process of moving the proton detector was automated; this allowed for data to be taken in a much finer grid compared to manually moving the detector. Data was taken by moving the detector in 1 mm increments over the full movable range; this amounted to an approximate 10 mm x 10 mm grid.

The proton detector alignment test was initially done with a $300mm^2$ detector that was moved from -4 to +6 mm in the horizontal and -5 to +3 mm in the vertical direction. The results of this scan can be seen in figure 6.9. Because of the relatively small area over which the proton detector can be moved and the peaked neutron beam distribution, the fall off in the $\frac{\dot{N}_p}{\dot{N}_{\alpha+t}}$ ratio is small compared to the uncertainty over a large portion of the scan area. As can be see in figure 6.9, the $\frac{\dot{N}_p}{\dot{N}_{\alpha+t}}$ ratio is practically constant from -2 to +4 mm in the horizontal and -2 to +2 mm in the vertical. A fall off can be seen as the proton detector moves to the extremities of the scan grid; this is most noticeable where the proton detector is furthest away from (0,0) at +6 mm horizontal and -5 mm vertical. The bottom plots of figure 6.9 show the calculated dependence of the proton rate on detector position

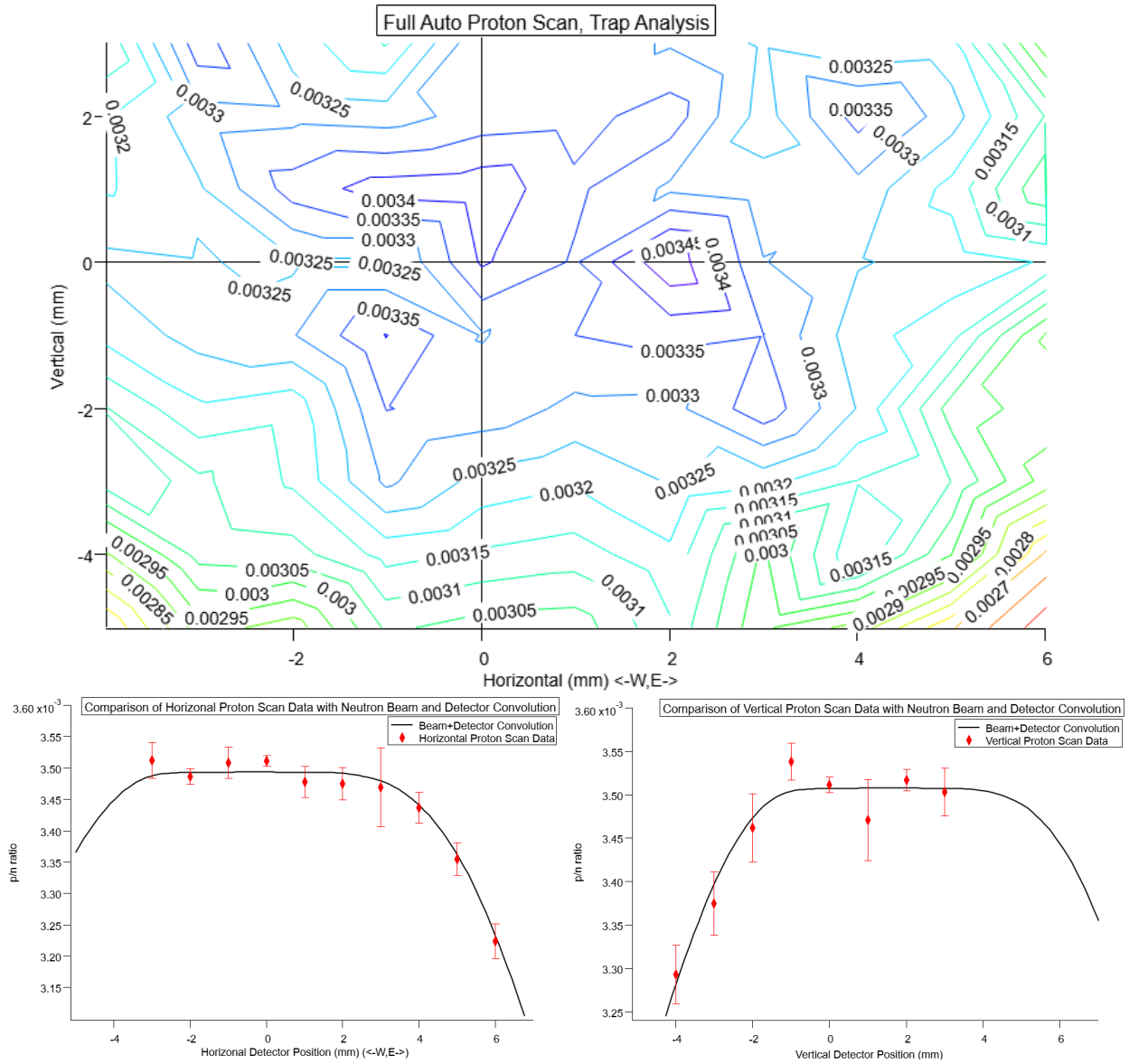

Figure 6.9: Top: contour plot of a full proton detector scan, $\frac{\dot{N}_p}{\dot{N}_{\alpha+t}}$ ratios are on the z-axis. A large plateau in $\frac{\dot{N}_p}{\dot{N}_{\alpha+t}}$ ratio relative to errors (not shown) can be seen in the region of (0,0). Relative error on the data approximately 2 %. Bottom: 1-dimensional proton scan data along horizontal (left) and vertical (right) axes. The data is compared with the excepted rate dependence (see text for details). Because of the restriction in detector movement, only one shoulder can be seen with data.

compared to 1 dimensional scans of the proton detector. This dependence is calculated using a convolution of neutron beam images with the active area of the detector. Using this scan, it is difficult to be certain that the proton detector is aligned to the center of the beam because a large portion of the scan is flat. However, this gives us confidence that the neutron beam distribution is well understood and the proton detector placement is not more sensitive than anticipated.

A smaller active area proton detector would increase the sensitivity to small changes in alignment. GEANT4 simulations were done for detectors ranging in size from 1 to 10 mm in radius to better understand this effect. A smaller detector is more sensitive to misalignment, but at a loss of stats which would require longer running times. For example, a 2 mm radius proton detector would start to see a noticeable drop off in $\frac{\dot{N}_p}{\dot{N}_{\alpha+t}}$ ratio after only a 1 mm misalignment, but would only have 16 % of the proton rate in the center of beam. A 5 mm radius active area detector was chosen for the next proton scan. This setup would show a noticeable drop off in rate after a 2 mm misalignment and keeps approximately 70 % of the proton rate. The 5 mm radius simulation also had the added benefit that the functional shape of the $\frac{\dot{N}_p}{\dot{N}_{\alpha+t}}$ ratio dependence is roughly Gaussian, which would allow for straightforward fitting to the data. To create a detector with an active region with a 5 mm radius, a 10 mm diameter hole was drilled into one of the plastic detector caps, and the detector was installed with this cap. A simple drilled hole in a plastic cap is not a precision aperture, but since relative rates are being compared, small imperfections in the cap hole can be ignored. The same proton scan technique as with the unmasked detector was followed, and data was taken in 1 mm intervals at roughly 100 different points. The data is plotted and fit to a two dimensional Gaussian and can be seen in figure 6.10. From the plot, the smooth drop off in $\frac{\dot{N}_p}{\dot{N}_{\alpha+t}}$ ratio in all directions can be seen. The results from the Gaussian fit gives a central value of (-0.16,0.63), which is within the requisite 1 mm. This gives us confidence that we can align the detector optically to the neutron beam center using the theodolite to better than the required precision. Furthermore, it is planned for production neutron lifetime data to be taken with a $600\,mm^2$ detector with a radius of 13.8 mm. Using these larger detectors significantly lessens the restrictions on the proton detector alignment.

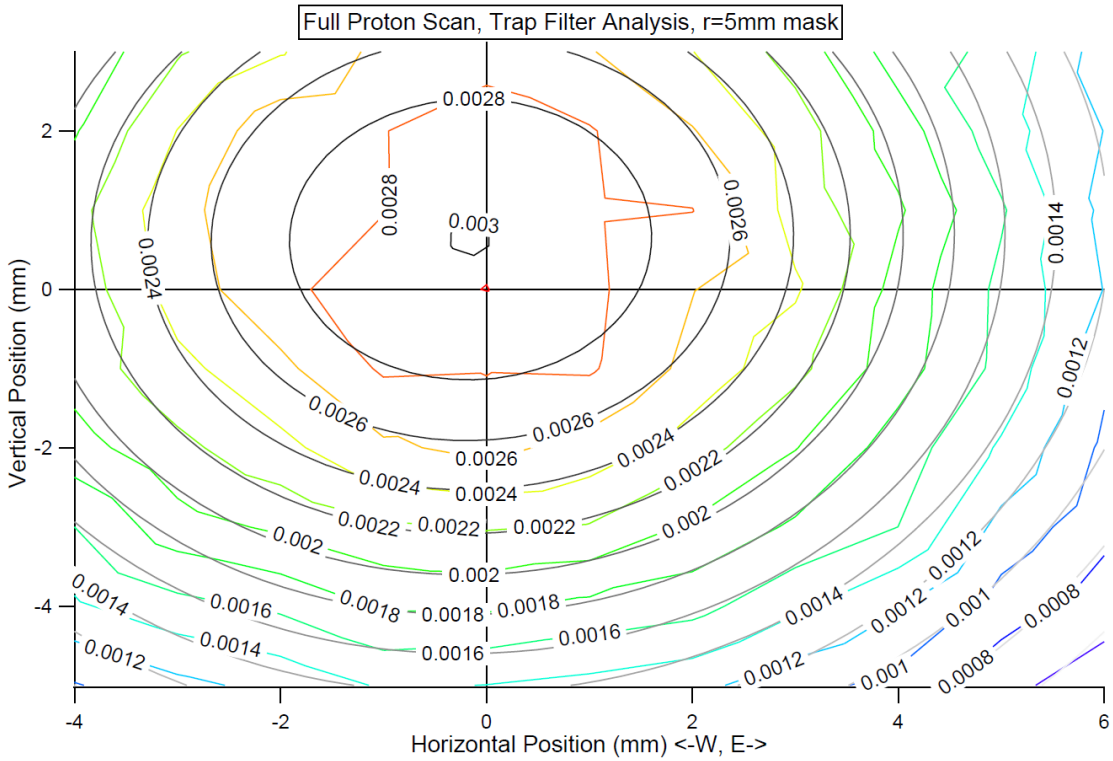

Figure 6.10: Contour plot of a full proton detector scan with a 5 mm radius detector mask, $\frac{\dot{N}_p}{\dot{N}_{\alpha+t}}$ ratios are on the z-axis. The data is fit to a 2-D Gaussian, and the centroid of the fit is within 1 mm of the nominal (0,0) centered position. Relative error on the data ranges from 2 to 5 %.

6.5 Proton Trapping Time Effects

One of the major questions about this experimental method is whether or not protons escape during the trapping sequence and going undetected. This would cause an artificially long measured neutron lifetime and was not extensively tested in BL1. One of the main goals of the BL2 systematic testing was to take data at multiple different trapping times to see if there was any change in the neutron lifetime. In BL1, a 10 ms trapping time was used almost exclusively. In 2018 and 2019, BL2 took data with trapping times ranging from 3 to 20 ms. In this data, it was inconclusive if the trapping time affected the neutron lifetime. In figure 6.11, it can be seen that there was no strong preference for a constant or a linear fit, and more data taking would be necessary.

The most powerful way to leverage data taking in this test is to take data with as long a trapping time as possible. However, because of stability issues in the BL1 apparatus, the trapping times used in BL2 were increased slowly. When the trapping time was increased to 30 ms, similar instability to that in the BL1 experiment was seen. If the apparatus was left running for too long, high energy pulses, correlated with the door opening, would start and damage the proton detector. This damage caused proton detector noise to increase to an unusable level. It was later discovered that completely zeroing the trapping voltages every few hours would stop this instability from occuring. Therefore, data taking continued at 30 ms trapping time with the caveat that data taking would be paused every few hours to zero the trapping voltages. With this procedure, enough data was collected at 30 ms to measure the neutron lifetime to a slightly worse precision than the data taken between 3 and 20 ms.

In figure 6.12, it can be seen that there was an increase in the measured lifetime with a 30 ms trapping time. It can be seen from the fits in figure 6.12 that the data does not fit well to a constant. This data fits reasonably well to a linear function, but the p-value for both fits with the 30 ms point added is worse than in the fits from figure 6.11. Because of the instability concerns of the apparatus at 30 ms, there is some reason to distrust the measured lifetime at 30 ms. It was then decided that we would attempt to improve the stability of the apparatus and take data at longer trapping times before making any conclusions about the dependence of the neutron lifetime on the trapping time.

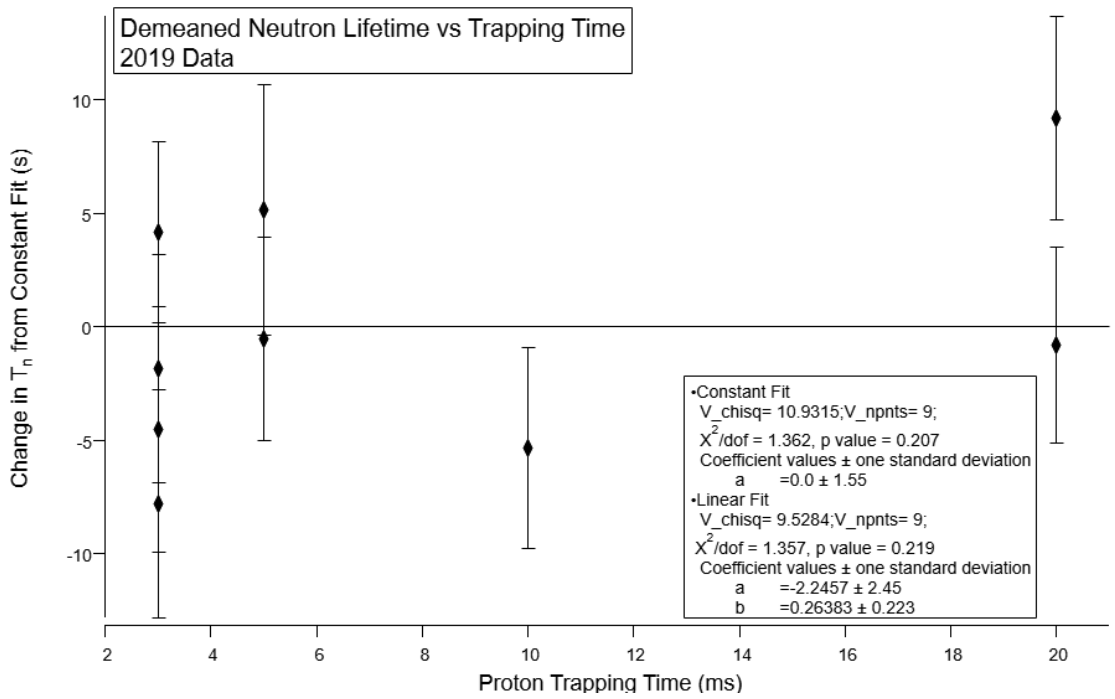

Figure 6.11: Change in the measured neutron lifetime vs trapping time. October 2019 reactor cycle, pre Si windows installation.

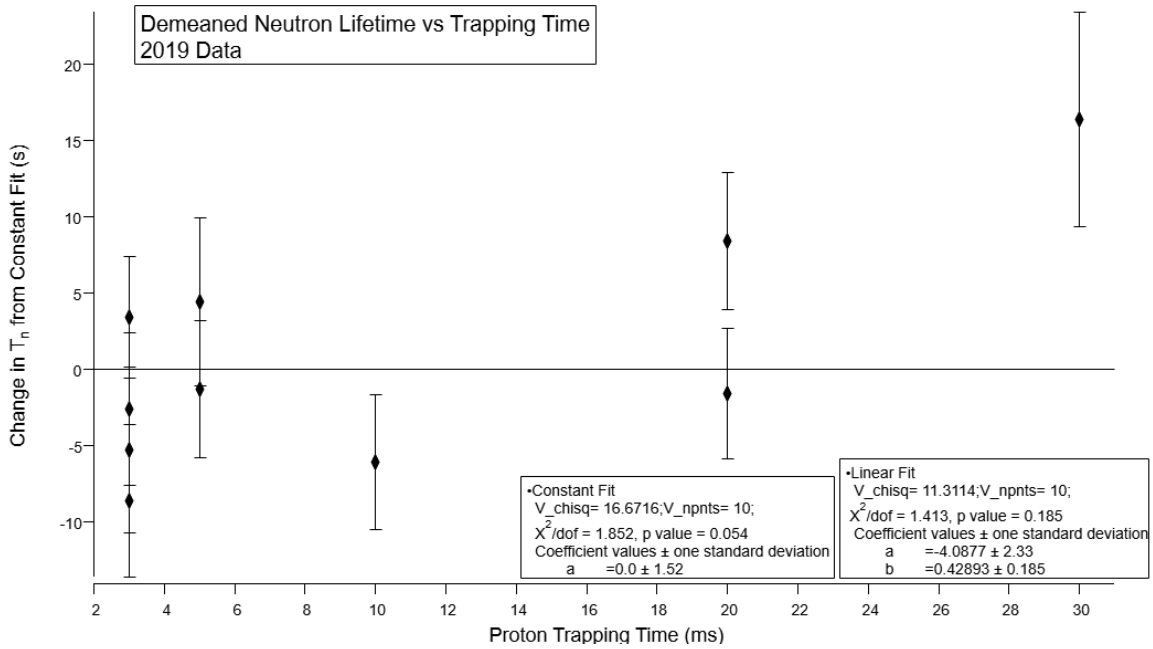

Figure 6.12: Change in the measured neutron lifetime vs trapping time with added data at 30 ms. October 2019 reactor cycle, pre Si windows installation.

At this point, a significant amount of time was devoted to pinpointing the cause of the instability. Some of the major findings of the instability studies are: 1) the neutron beam is not required for the instability to occur, 2) shutting off the accelerating potential does not stop the high energy pulses, 3) changing the door and flush voltages seemed to have no effect on stability, 4) increasing the ramp and mirror voltages made the apparatus less stable, decreasing them made the apparatus more stable. The instability was particularly sensitive to manipulating the mirror voltage as it could be made to come and go by turning the mirror voltage on and off.

In addition to the trapping voltages, the connection of the magnet bore to the upstream and downstream vacuum sections was also investigated. Because the instabilities were not dependent on the neutron beam, the vacuum gate values could be opened or closed during this testing. With the gate valves connecting the cold magnet bore to the rest of the room temperature beamline closed, stability improved significantly. Similarly to the test of the trapping voltages, it was also seen that the stability was affected more by the downstream gate valve (closer to the mirror) than it was by the upstream gate valve (closer to the door). With both gate valves closed, the apparatus was able to run stably up to 100 ms trapping time. At that point, we started to design an apparatus modification to better isolate the cold magnet bore from the rest of the warm beamline vacuum sections.

The goal of the cold bore isolation was mainly to improve the pressure in the trapping and proton detection regions. An additional goal was to decrease possible interactions between the warm and cold vacuum sections while affecting the neutron beam as little as possible. As discussed in section 3.4, two thin, perfect silicon windows were installed upstream and downstream of the magnet at the closest possible flange connection. Even though the total scattering cross section of silicon is slightly larger than some other possibilities, aluminum for example [68, 85], the ability to make single crystal silicon decreases the likelihood of scattering. From previous experience with silicon wafers [83, 67, 108], the scattering in a polychromatic beam is larger than one would expect from pure Bragg scattering. However, this type of systematic effect was previously accounted for because of the silicon wafer backing of the ^6Li target. Because the silicon windows are installed in gates valves, this gives the ability to do an in situ measurement of the change in neutron flux with the windows open

and closed. No data has yet been taken for this systematic effect but it is planned at the end of the running period.

These silicon windows were installed in November 2019, and over the next couple months, data was taken comparing the neutron lifetime with the windows in the open and closed positions between 3 and 20 ms trapping time. It was consistently seen that the pressure in the vacuum section connected to the proton detector was lower when the windows were closed, routinely going under range ($< 3.79 \times 10^{-9}\ Torr$) of the pressure gauge.

As can be seen in figure 6.13, the neutron lifetime values are similar at short trapping times, but at 20 ms the windows closed data continued to be flat while the neutron lifetime with the windows open increased. Because of instability concerns at trapping times greater than 20 ms, it was decided that data taking at 30 ms and longer trapping times would continue with windows closed only. With the windows closed, we continued to see lower pressure in the proton vacuum section and have seen no stability issues at trapping times up to 100 ms. The January 2020 and March 2020 reactor cycles were dedicated to investigating the neutron lifetime dependence on the trapping time. The January 2020 cycle was roughly 6 weeks of data, but the March 2020 was only approximately a week before the facility was shutdown due to the Covid-19 pandemic. In the January cycle, data was taken at 10 different trapping time ranging from 3 ms to 100 ms, in the March cycle, data was taken at 3 ms and 50 ms.

As can be seen in figures 6.14 and 6.15, the conclusions from these data are not straightforward. In the January 2020 cycle, the data fits well with a linear function with the exception of the 100 ms data, which has a longer lifetime than one would expect with a linear trend. The March 2020 data shows no change in the neutron lifetime out to 50 ms. Unfortunately, no data was taken at longer trapping times because the cycle was cut short. If the trend from the January 2020 cycle was present in the March 2020 data one would expect the neutron lifetime at 50 ms to be about 15 s longer than the neutron lifetime at 3 ms. Even with very little data, this would be clearly seen. Throughout the rest of the 2020, reactor operation was sporadic and time in the lab was limited due to the pandemic. However, some data was taken with a variety of different detector types. While carrying out other systematic tests, data was always taken at different trapping times. Between November

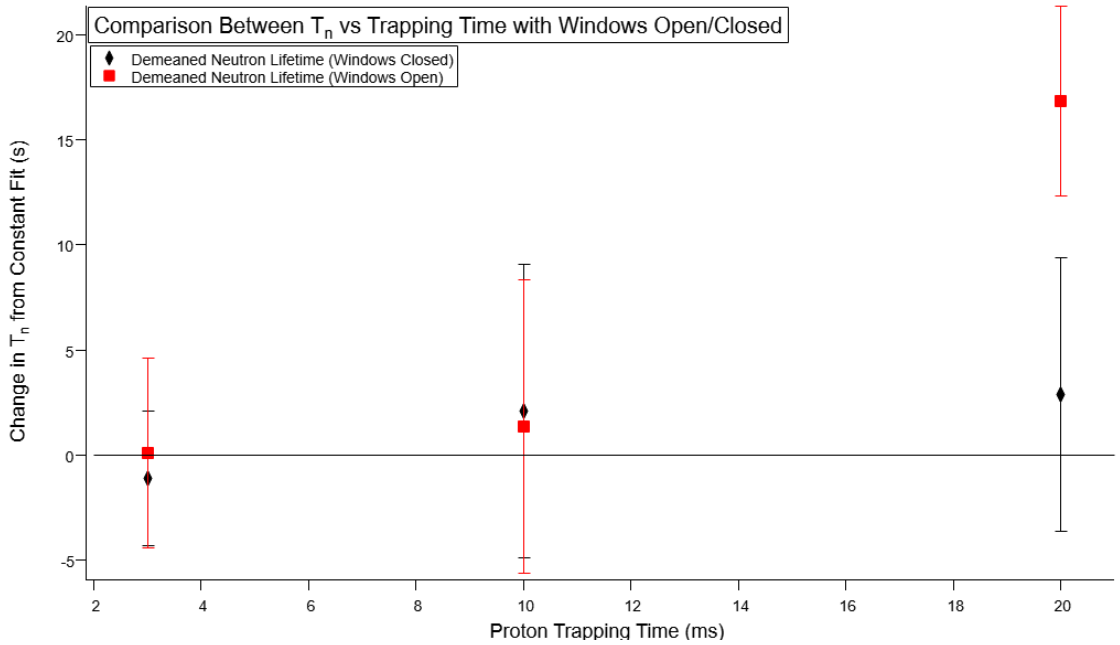

Figure 6.13: Change in the measured neutron lifetime vs trapping time showing the difference between Si windows open and Si windows closed. November 2019 reactor cycle data.

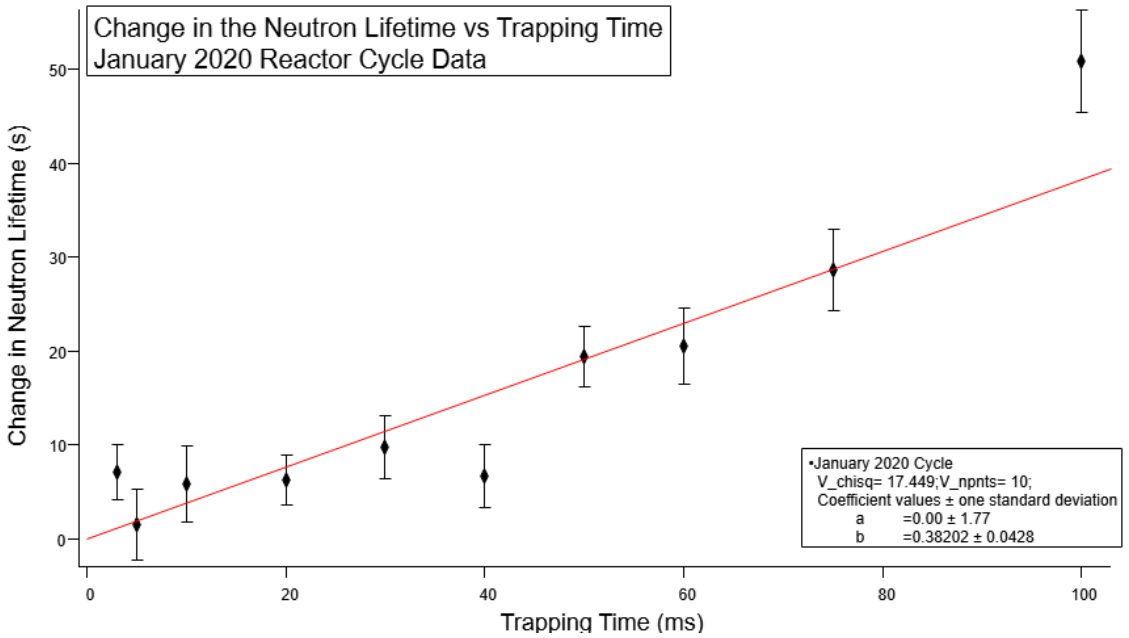

Figure 6.14: Change in the measured neutron lifetime vs trapping time for the January 2020 reactor cycle.

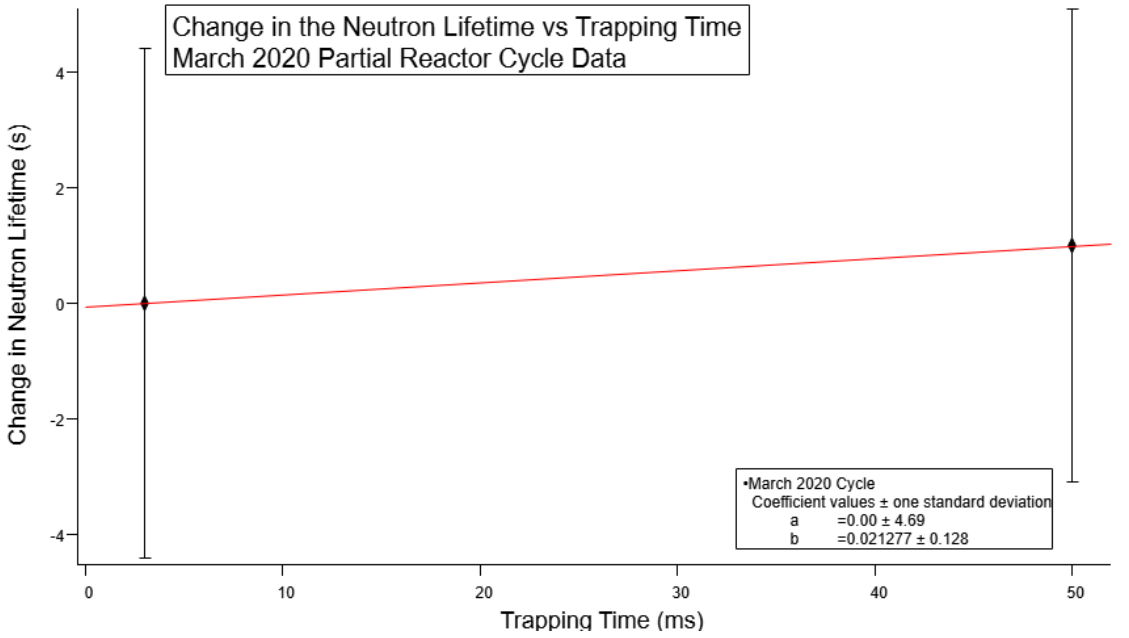

Figure 6.15: Change in the measured neutron lifetime vs trapping time for the March 2020 reactor cycle.

2019 and present, data has been taken in 6 reactor cycles that varied between 1 and 6 weeks. A collection of the neutron lifetime vs trapping time plots for all of these cycles can be seen in appendix E. As can be seen in the collection of plots, there are a variety of results. Two of the cycles produced results that did not show a neutron lifetime dependence with trapping time, the other four cycles show a roughly linear relationship, with the neutron lifetime increasing as trapping time increases. One possible explanation for the differences in each cycle could be the average pressure during data taking. One could imagine that there is a correlation between the pressure and the change in the lifetime. However, looking at the closest pressure monitor to the proton trap and detector we see no significant difference in the pressure when comparing the cycles.

Figure 6.16 shows the pressure recorded by two different pressure gauges installed in the same vacuum section as the proton detector. As mentioned earlier, after the windows were installed the pressure gauge routinely read "under range," this can be seen in the black points. After series S1046, a different pressure gauge was installed with the ability to read lower pressures, these points can be seen in red. Figure 6.16 covers all series in which the data in appendix E was taken, the newer gauge was installed before the July 2020 cycle. There is no correlation between the pressure in these series and the measured neutron lifetime dependence. Currently, there is no concrete explanation for some cycles showing a significant neutron lifetime dependence on the trapping time. The current best guess is there are subtle, local vacuum effects in the trapping volume that change when the apparatus is opened to atmosphere in-between reactor cycles. This is part of the reason the Mark III trap was installed as it should have better local vacuum conditions as discussed in section 2.2. Unfortunately, no data has been taken with the Mark III trap for comparison due to the reactor outage discussed in section 8.2. The goal is to take similar data with the Mark III trap and compare this data to the Mark II trap data before making any conclusions.

6.6 Proton Detector Backscatter Extrapolation

Because of the absolute counting nature of the experiment, proton backscatter off of the detector leads to a direct shift in the measured neutron lifetime. There is currently no

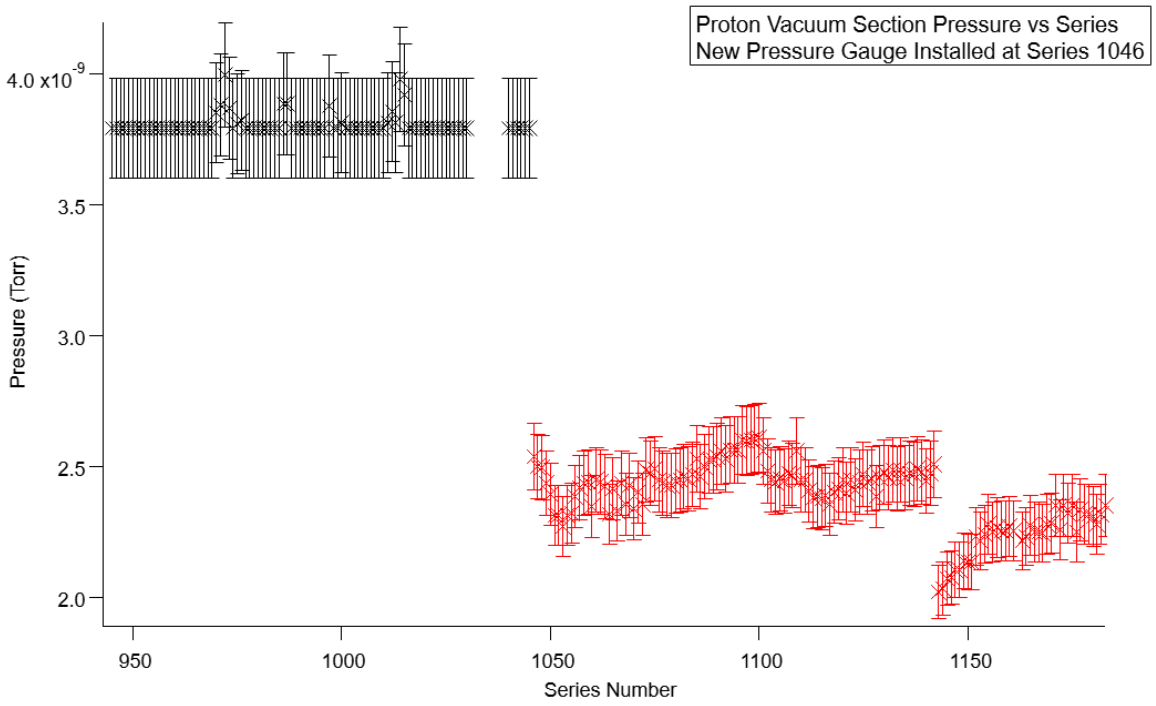

Figure 6.16: Proton detector vacuum section pressure vs series. Change at series 1046 corresponds to the installation of a new pressure gauge. The error bars are equal to the the manufacturer's specifications for repeatably for each gauge.

possible way to account for this effect with data, so we rely heavily on simulation for this systematic correction. There is a further complication that any proton that backscatters will be turned around by the acceleration potential and may still have enough energy to be detected. To account for these effects, neutron lifetime data is taken with many different detector types. These detectors have different backscatter fractions, and by taking data with different detectors, the neutron lifetime can be plotted against the simulated backscatter fraction. The neutron lifetime dependence on the backscatter fraction can then be fit and extrapolated to zero backscatter. This is by far the most time consuming systematic test of the experiment because, for each detector type, the neutron lifetime must be measured to good precision.

The backscatter fraction depends on the acceleration potential, the deadlayer material, and the deadlayer thickness. This gives the experiment a wide range of backscatter fractions to measure. Depending on the configuration, the backscatter fraction can vary by up to a factor of 40. Rutherford scattering from the atomic nuclei can be calculated analytically. Although this does not take into account multiple scattering and energy loss in material, this is still a good check of the backscatter fraction. If one has protons of energy E, incident on a material of atomic number Z, the Rutherford backscattering cross section is given by:

$$\sigma_{Ruth} = 2\pi \int_{\frac{\pi}{2}}^{\pi} \left(\frac{m_e c^2}{E} \frac{Z r_e}{4 sin^2 \frac{\theta}{2}} \right) sin\theta d\theta \tag{6.1}$$

$$\sigma_{Ruth} = \frac{\pi}{4} Z^2 r_e^2 \left(\frac{m_e c^2}{E} \right)^2, \tag{6.2}$$

where θ is the scattered proton angle, integrated over all possible angles, and r_e is the classical radius of the electron. It then follows that the backscatter probability is given by:

$$P_{bk} = \frac{N_A}{A} \sigma_{Ruth} \rho, \tag{6.3}$$

where N_A is Avogadro's number, A is the atomic weight of the deadlayer material, and ρ is the areal density of the detector deadlayer. It can be seen that P_{bk} is dominated by the material of the detector, but it is also inversely dependent on the square of the

acceleration voltage. As an example, let's consider the two most extreme cases used in this experiment, a PIPS detector at high acceleration voltage and an SB detector with a thick deadlayer at low acceleration voltage. Let's assume the PIPS detector has a deadlayer of SiO_2 with density 2.65 g/cm^3, for a nominal deadlayer thickness of 775 Å, the areal density is then $2.05 \times 10^{-5}\, g/cm^2$. Our thickest deadlayer SB detector has an areal density of $100 \times 10^{-6}\, g/cm^2$ per the manufactures spec sheet. If we now assume the highest operating voltage for the PIPS detector (35 kV) and the lowest operating voltage for the SB detector (25 kV), we see that $P_{bk_{PIPS}} \approx 0.125\,\%$ and $P_{bk_{SB}} \approx 5.4\,\%$, a difference of more than 40 times. For an example of how varying the acceleration potential changes the backscatter probability see figure 6.17. The plotted data encompasses four detector types, a PIPS detector and SB detectors with 20, 40 and 60 $\mu g/cm^2$ Au deadlayers, these detectors are the mostly likely to be used for production data. Each detector type has its backscatter fraction calculated for four different acceleration potentials between 25 and 32.5 kV. This plot demonstrates how the material and thickness of the deadlayer dominate P_{bk}, but varying the acceleration potential can also change P_{bk} by a factor of 2 or 3. Note that this calculation does not include any energy loss of the protons as they traverse the deadlayer. In general, the proton energy loss is proportional to 1/A and P_{bk} is proportional to A. This means that higher Z materials have less energy loss through the deadlayer, but larger P_{bk} [67]. For this experiment, that means that for similar deadlayer thickness a PIPS detector will have greater energy loss but less backscatter than a SB detector. These effects are taken into account by using the Stopping and Range of Ions in Matter (SRIM) software package [109].

6.6.1 SRIM Simulation of the Proton Backscatter Fraction

While the analytic expressions in equations 6.2 and 6.3 are useful for quick estimates of the backscatter fraction, it neglects to account for some aforementioned effects like multiple scattering (allowing for a proton to scatter multiple times in the material) and energy loss in the material. For a full treatment of backscatter physics SRIM 2013 is used [109]. The simulation setup is rather straightforward for our purposes. The user inputs the energy of the incident ion (proton), the incident angle, the material of the deadlayer, and the deadlayer thickness. The simulation then uses a large collection of tabulated stopping ranges that are

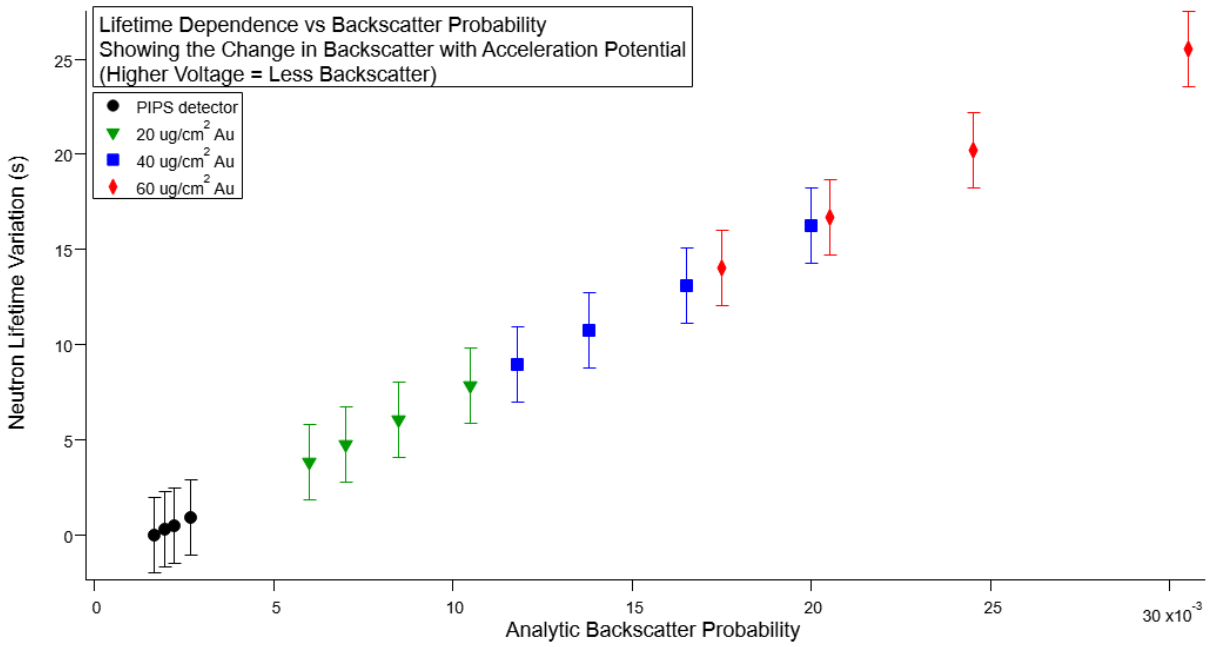

Figure 6.17: Predicted change in the neutron lifetime vs backscatter probability calculated with equation 6.2. The spread in each detector type corresponds to varying the HV potential. Error bars on the points are commensurate with typical measured lifetime uncertainties.

dependent on the density of the deadlayer to calculate the trajectory of the incident ion. One significant complication to these simulations is the thickness of the deadlayer used. The detector manufacturers typically do not give an uncertainty of the deadlayer of the detector (and if they do the uncertainties are large), so the deadlayer must be determined experimentally. To do this, the detector is calibrated using the 59.5 keV gamma from a ^{241}Am source. After the detector is calibrated, the single proton energy peak is fit to a Gaussian giving the deposited energy of a typical proton. The difference between the acceleration potential and this deposited energy is the energy loss through the deadlayer, E_{loss}. E_{loss} is a direct result of the deadlayer thickness, which can be estimated using the stopping range calculations in SRIM. The exact thickness of the deadlayer is slightly more complicated and tedious to extract. Because one is not able to give SRIM a desired energy loss, only the deadlayer thickness, the precise determination is an iterative process. The simulations are run initially for only a short period of time necessary for fitting to the central proton peak. This value is then compared to E_{loss} for the calibrated proton energy spectrum. The deadlayer thickness is then varied slightly and the process is repeated until the simulated energy loss agrees with E_{loss}. After this is determined, a much longer simulation is run with 1×10^6 events; each of these simulations takes approximately 12 hours.

SRIM gives the user the option of three "damage calculation models," the description of these three models from the SRIM textbook [110] can be seen in appendix D. For BL1, the simulations used the default "quick" calculation model. Using this model for comparisons to BL2 data it was seen that the output energy spectra did not match well as the width of the proton energy peak was far greater in the simulation than the data.

As seen in figure 6.18, the quick and "full" damage calculation types are nearly identical while the "monolayer" damage calculation type is significantly narrower. A narrower peak is expected as the simulation does not account detector noise that widens the analyzed spectra. The SRIM textbook [110] describes that to save computation time the quick and full damage calculation models use a "Free Flight Path" approximation which allows an incident ion to travel up to $1\,\mu m$ in the detector material without interactions. This is acceptable in some applications but with deadlayers $< 1\,\mu m$ for all detector types this is not an appropriate model to simulate BL2 data. Using the monolayer damage model

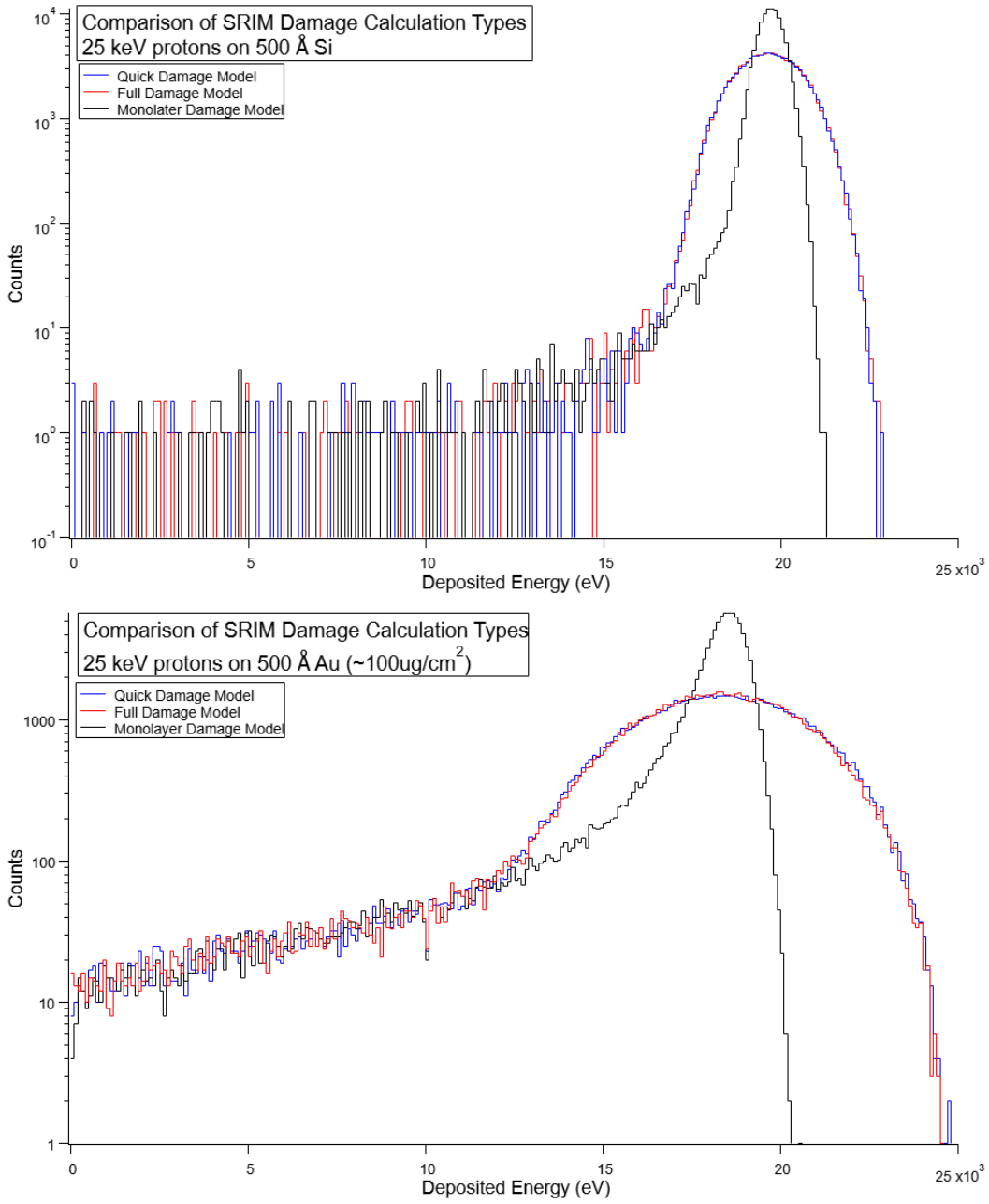

Figure 6.18: Top: comparison of the quick, full, and monolayer damage calculation model for a proton with 25 kV of energy incident on 500 Å of Si. This is similar to a PIPS detector deadlayer Bottom: comparison of the quick, full, and monolayer damage calculation model for a proton with 25 kV of energy incident on 500 Å of Au. This is similar to a SB detector deadlayer. Both plots show that the quick and full calculation models are similar and result in a significantly wider proton peak than the monolayer model.

SRIM does not use approximations, and it forces the ion to interact every few Å. This significantly increases the simulation time but results in a more believable energy spectrum. All simulations were done using this damage calculation model.

The output of the SRIM simulation is two files, "BACKSCAT" which contains the kinetics of ions that "after one or more target collisions, have a trajectory that exits the target back through its surface," and "TRANSMIT" which contains the kinetics of ions that "leave the bottom of the target." Each of these files lists the energy and trajectory of each ion (proton) that leaves the deadlayer. From the TRANSMIT file, the energy of each ion is taken as the amount of energy that will be deposited in the detector. The BACKSCAT file is largely used to tabulate the number of backscattered events, although the trajectories of the backscatter protons can be used as input for a more sophisticated simulation to estimate the number of protons that return to the detector. Using these files, one can determine $f(H)_{ruth}$ and $f(H)_{act}$. $f(H)_{ruth}$ is the fraction of proton events that backscatter from the deadlayer and $f(H)_{act}$ is the fraction of proton events that backscatter from active region of the detector. $f(H)_{act}$ requires an extra simulation to calculate but, P_{bk} was previous dominated by $f(H)_{ruth}$ so, $f(H)_{act}$ will be ignored for now. This leaves a simple calculation for $f(H)_{ruth}$. It is simply taken as the ratio of the total number of events in the BACKSCAT output file to the total number of simulated events. For all possible experimental configurations, the proton backscatter fractions can be seen in table 7.2. The exact backscatter correction to the neutron lifetime will not be known until all detector types and acceleration voltages are known.

6.7 Undetected Protons

There are two possibilities where a proton could be trapped, hit the detector and not deposit enough energy to be detected. Those are denoted by $f(H)_{stp}$ and $f(H)_{BT}$, which correspond to the fraction of protons that stop in the deadlayer of the detector and the fraction of protons that enter the active region but do not deposit enough energy to be detected, respectively. $f(H)_{stp}$ is impossible to determine experimentally, so SRIM is used to simulate all possible detector configurations. The SRIM simulation tabulates each particle that is transmitted

or backscattered from the deadlayer, any event that is not in either of these categories is considered to be stopped in the deadlayer and undetected. The value of $f(H)_{stp}$ changes significantly depending on the acceleration potential and deadlayer of the detector. With a thin deadlayer, $f(H)_{stp}$ can be neglected entirely. With a low acceleration potential, and a thick gold deadlayer detector $f(H)_{stp}$ can be as large as a 1.2 % effect on the proton rate. For a determination of $f(H)_{stp}$ for all possible run configurations see table 7.2.

The fraction of below threshold protons, in addition to being dependent on the detector deadlayer and the acceleration potential, is also dependent on variables that are not captured in simulation. The two largest contributors that are not captured are intrinsic detector noise and the noise suppression in the analysis. Data is generally taken with either a 300 mm^2 or a 600 mm^2 area detector and these vary from 300 μm to 1000 μm depletion depth. The detector noise is proportional to the capacitance of the detector, which is proportional to the ratio of the detector area to the depletion depth. The smaller the area or the thicker the detector, the less intrinsic noise the detector has. Using the optimized trapezoid filter parameters from section 4.3, the proton energy threshold is typically between 5 keV and 8 keV depending on the detector used. To determine $f(H)_{BT}$, the energy transmitted through the deadlayer from the SRIM simulation is overlaid against the analyzed data. In principle, the low energy proton tail matches well with the data, and $f(H)_{BT}$ is taken as the fraction of proton events that are below the analysis threshold. However, at low acceleration potential or with thick deadlayer detectors it can be difficult to make this comparison precisely. In these scenarios, there is only a small portion of the low energy proton tail visible above the noise. To address this, data is taken with the same detector at multiple acceleration potentials. An example of these energy spectra with varying acceleration potentials can be seen in figure 6.19. Using this type of data, the analyzed tails can be benchmarked against the simulation. If the low energy proton tails agree well with the high acceleration potential data, then it can be assumed they will also agree well with lower acceleration potential data. The reason that not all data is taken with a high acceleration potential is that this increases the likelihood of catastrophic detector breakdown. This benchmarking allows for the majority of data to be taken at a safer acceleration potential, while still having confidence in the below threshold

proton correction. A list of $f(H)_{BT}$ for all possible apparatus configurations and a reference threshold (6 keV) can be seen in table 7.2.

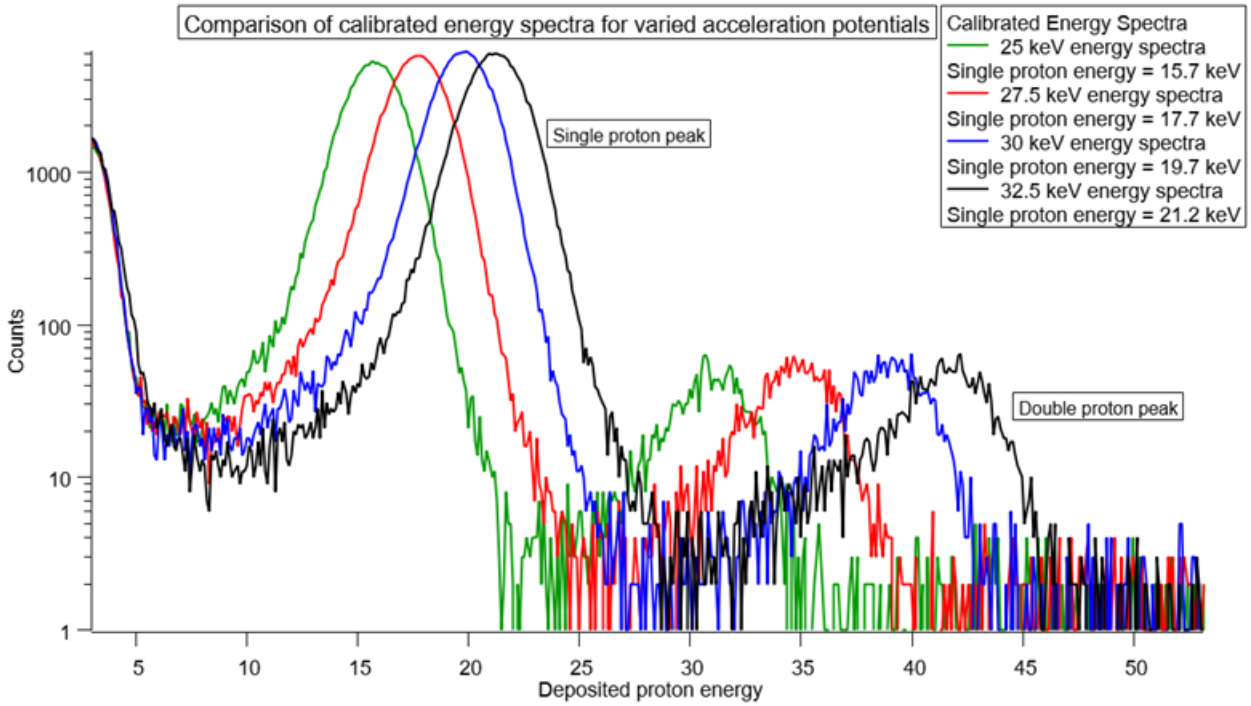

Figure 6.19: Example of proton energy spectra for varying high voltage potentials. The larger the accelerating potential the more proton tail can be seen which can more easily be compared to simulation.

Chapter 7

Detection Efficiency of Molecular Hydrogen

On average, protons make many axial bounces during the trapping cycle. This enhances the possibility that protons could interact with the residual gases in the trapping volume. These interactions could change the trapping or detection efficiency of the protons leading to a systematic shift in the neutron lifetime. In this chapter, I will discuss one of these interactions and the effects it causes in the data.

7.1 Residual Gas Interactions in the Proton Trap

Protons bouncing back and forth in the proton trap are subject to three types of interactions with residual gas: 1) elastic scattering, 2) inelastic scattering, and 3) charge exchange. The first two types of scattering do not change the efficiency of proton detection, because they do not increase the proton energy as the residual gas molecules are extremely low energy. However, charge exchange, where one or more electrons are transferred between a residual gas atom (molecule) and the proton, results in an ionized atom (molecule). The now ionized atom (molecule) will follow the magnetic field lines and be accelerated to the detector just like a normal trapped proton. This has the potential to decrease the proton detection efficiency because the heavier atom (molecule) losses more energy in the deadlayer of the detector. The charge exchange interaction dominates in this low energy regime where the proton velocity

is less than the orbital electron velocity of the residual gas atom (molecule) [23]. Charge exchange of a trapped proton and a residual gas atom (molecule) is represented by:

$$p + M \rightarrow H + M^{+}, \tag{7.1}$$

where p is a proton, M is any atom or molecule and H is a neutral hydrogen atom. The proton captures an electron from a residual gas atom (molecule) and is converted to a neutral hydrogen atom, which escapes the trap and the singly charged atom (molecule) is left trapped. The new ion, M^{+}, then acts as a normal trapped proton, confined axially by the electrostatic field of the door and mirror and radially by the magnetic field. When the trap transitions into counting mode, the M^{+} ion is transported to the proton detector by the acceleration potential and is detected with efficiency ϵ_M, where each M^{+} has a separate efficiency.

The superconducting magnet is cooled by liquid helium. When the magnet comes to equilibrium with the rest of the apparatus, its bore is $< 10\,K$. At these temperatures all residual gasses "freeze out" except for hydrogen, helium and neon. Figure 7.1 shows the calculated saturated vapor pressure for many common gasses as a function of temperature [7].

It is expected that the partial pressure of all other species except for helium and hydrogen are low enough as to not contribute to charge exchange with trapped protons. The majority of the pumping for the two lightest gasses is done by three ion pumps outside of the cold magnet bore. This makes the partial pressure of H_2 and He difficult to estimate.

The probability, $P_M(x)$, of a proton charge exchange occurring is

$$P_M(x) = 1 - e^{n\sigma_M x} \sim n\sigma_M x, \tag{7.2}$$

where σ_M is the charge exchange cross section for each residual gas, x is the distance traveled through the residual gas, and n is the number density of the residual gas [23]. At low energies, $< 1\,keV$, charge exchange cross sections vary significantly over the range of light elements and common molecules [98, 76, 12, 93, 45, 92, 1]. The charge exchange cross section for ^4He is approximately two orders of magnitude lower than molecular hydrogen for the relevant

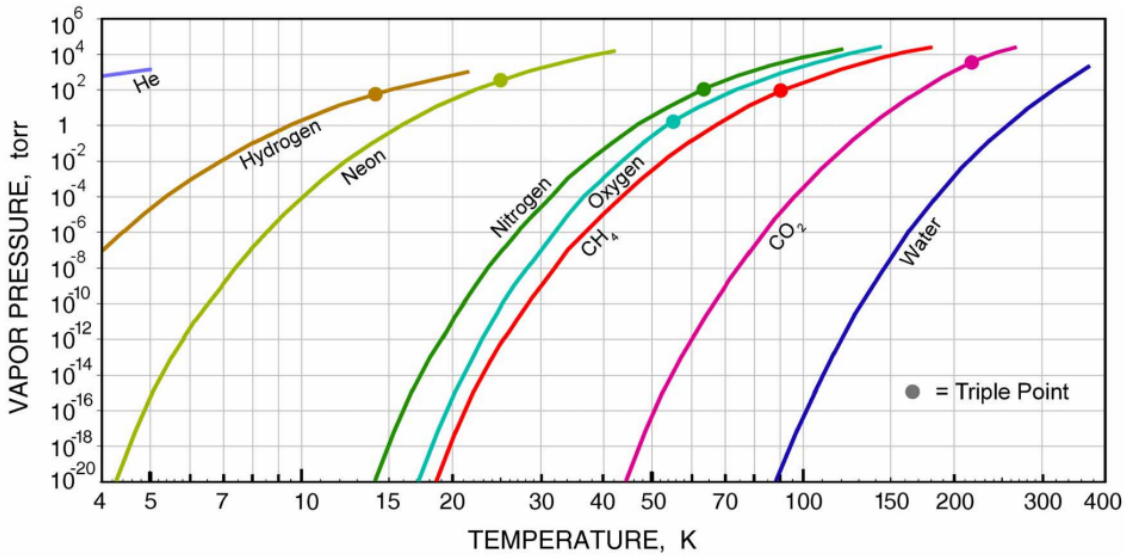

Figure 7.1: Saturated vapor pressure of common gases as a function of temperature, calculated in [7], taken from [102].

energy ranges [76, 1, 93], and we assume the partial pressure of all other gasses are extremely low. As a result we will focus solely be on molecular hydrogen, H_2, in this chapter.

7.2 Evidence of Trapped H_2^+

Proton charge exchange with molecular hydrogen, H_2, resulting in singularly ionized molecular hydrogen, H_2^+, and a neutral hydrogen atom, H, would result in many observable effects in the BL2 data. In the sections below, I will cover indications that show why we believe H_2^+ ions are being created via charge exchange. Many of these effects have been observed including, evidence for low energy, trapped ions, deposited energies that agree with the simulation of H_2^+ molecules in solid state silicon detectors, a pressure related dependence on these type of events, and a change in the backscatter fraction.

7.2.1 Low energy H_2^+ Ions

A proton undergoing $p(H_2, H_2^+)H$ would result in the H_2^+ molecule being trapped while the H atom escapes. This H_2^+ molecule would have very low energy because the initial H_2 molecule is thermalized with the cryogenic magnet bore, on the order of 10 K. Since these H_2^+ molecules are now trapped with much lower energies than decay protons they will behave differently after the trap is opened. The majority of the decay protons have enough energy to escape the trap without the need of the potential ramp. Because of this, we see protons almost immediately after the door is opened and continuing until the low energy protons are pushed out by the ramp. Because the H_2^+ molecules have such low energy it is not expected to promptly see these type of events. The vast majority of these events would be kicked out by the ramp, and it is expected that the arrival time of these events would depend almost entirely on the ramp voltage.

Figure 7.2 shows an example of the typical 2-dimensional histogram of proton energy and arrival time with a high and low ramp voltage. In these plots, it can be seen that there is an excess amount of events at the tail end of the trapped proton peak that is consistent with the expected arrival time of H_2^+. It is also expected that a lower ramp voltage would make it easier to see these events at the tail end of the proton timing spectrum because fewer

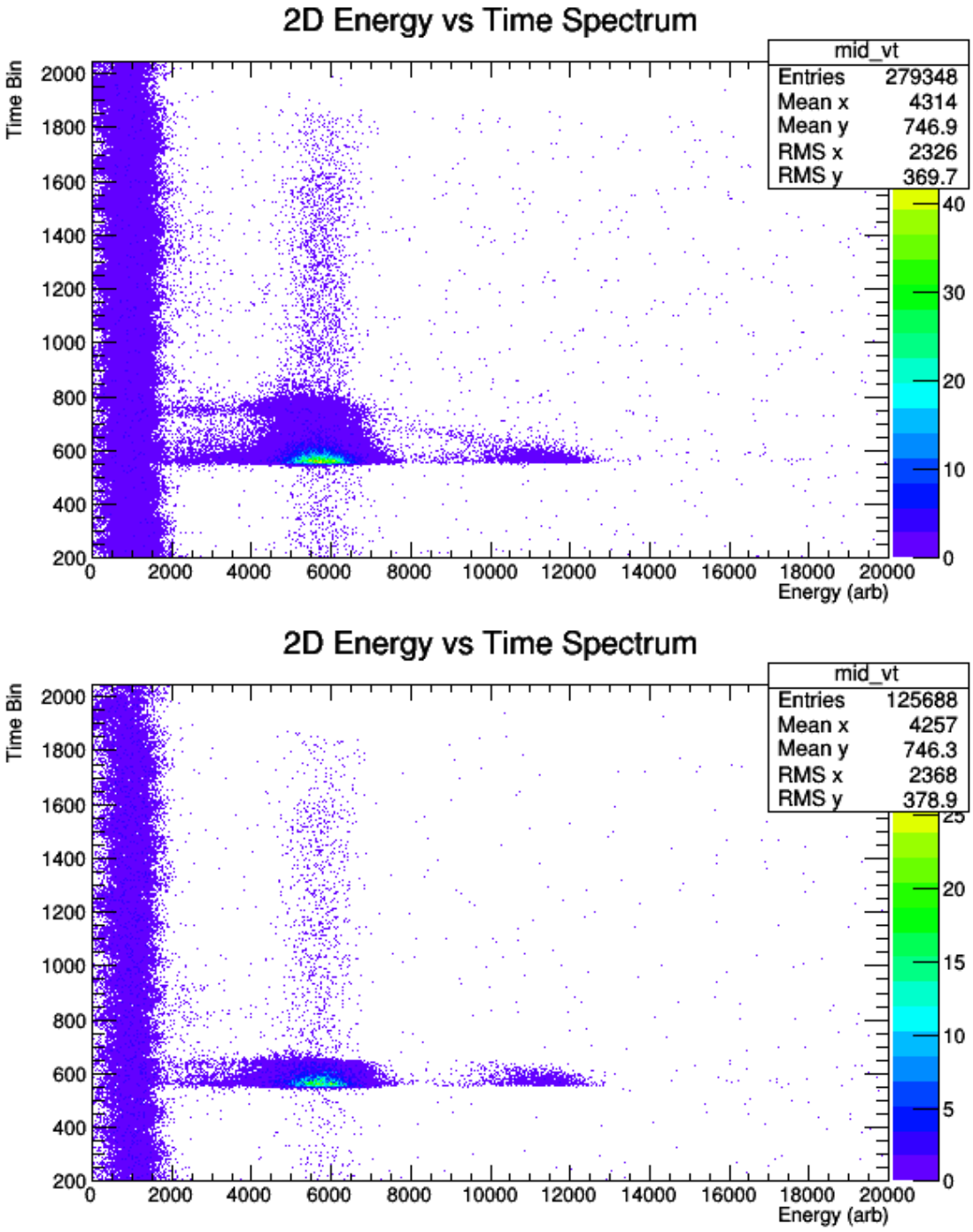

Figure 7.2: Comparison of 2-dimensional proton energy and proton arrival time histograms, showing the difference in the arrival time of the bonus peak as a function of the ramp voltage. Top: 14.4 V ramp, Bottom: 45 V ramp.

protons are kicked out by the lower ramp, but nearly all H_2^+ molecules are kicked out by the ramp. Figure 7.3 shows the arrival time spectra for five different ramp voltages. One can see that as the ramp voltage decreases the H_2^+ peak becomes more visible, and at zero ramp voltage there is no H_2^+ peak because there is no potential to bunch the ions in time. Seeing these excess events at the tail end of the proton arrival time was the first indication that something other than decay protons were being trapped, these events came to be known as the "bonus peak."

7.2.2 Pressure and Trap Time Dependence

The charge exchange mechanism is dependent on the number density of the residual gas. Therefore, it is expected that as the partial pressure of a gas increases, the probability of charge exchange would also increase. After the two, thin perfect crystal silicon windows were installed just upstream and downstream of the magnet bore, the pressure in the proton vacuum section was noticeably lower. As a result, the fraction of bonus peak events seen in the data was smaller for apparatus configurations that were otherwise identical. Figure 7.4 shows the arrival time spectrum for two series with identical run parameters except the blue histogram was taken with the windows closed and the red histogram was taken with the windows open. One can see that for otherwise identical arrival time spectra, there is a much more noticeable peak at times where the bonus peak is expected.

Residual gas analyzer (RGA) data is also taken periodically, usually at the end of a reactor cycle. The RGA is positioned in the warm region of the proton detector vacuum section. This is not a direct measurement of the bore vacuum; however, we believe the trends in the data are useful. Using these spectra it is possible to track correlations between bonus peak events and specific atomic masses. As seen in figure 7.5, RGA spectra can differ substantially from reactor cycle to reactor cycle, this is because the vacuum system is opened in-between reactor cycles to swap detectors. It is rarely seen that there are significant changes in the bonus peak fraction during the same reactor cycle, further evidence suggesting that the composition of the vacuum make up is important, and taking RGA spectra at the end of a reactor cycle is sufficient. While figure 7.5 shows much more H_2O and CO_2 in the vacuum during the March 2020 cycle the, January 2020 RGA spectra shows an increased

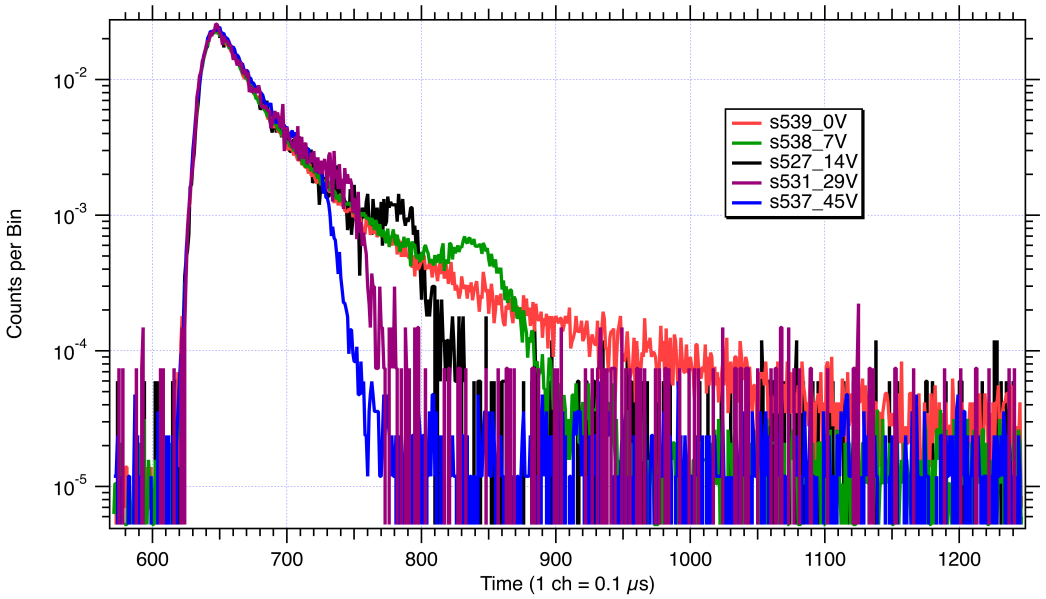

Figure 7.3: Comparison of the arrival time of bonus peak with varied ramp voltage. Lower ramp voltages lead to a later arrival time and easier identification of the bonus peak.

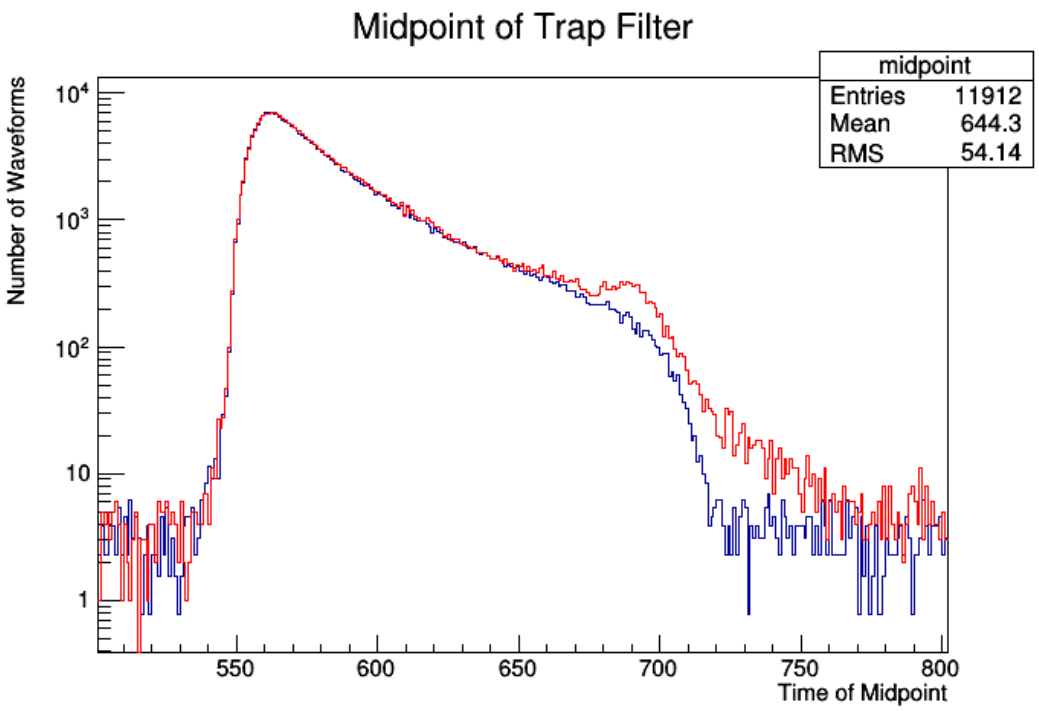

Figure 7.4: Comparison of proton arrival time spectra between Si windows open (red) and Si windows closed (blue), showing the increase in the bonus peak at time bin ≈ 700 with the Si windows open.

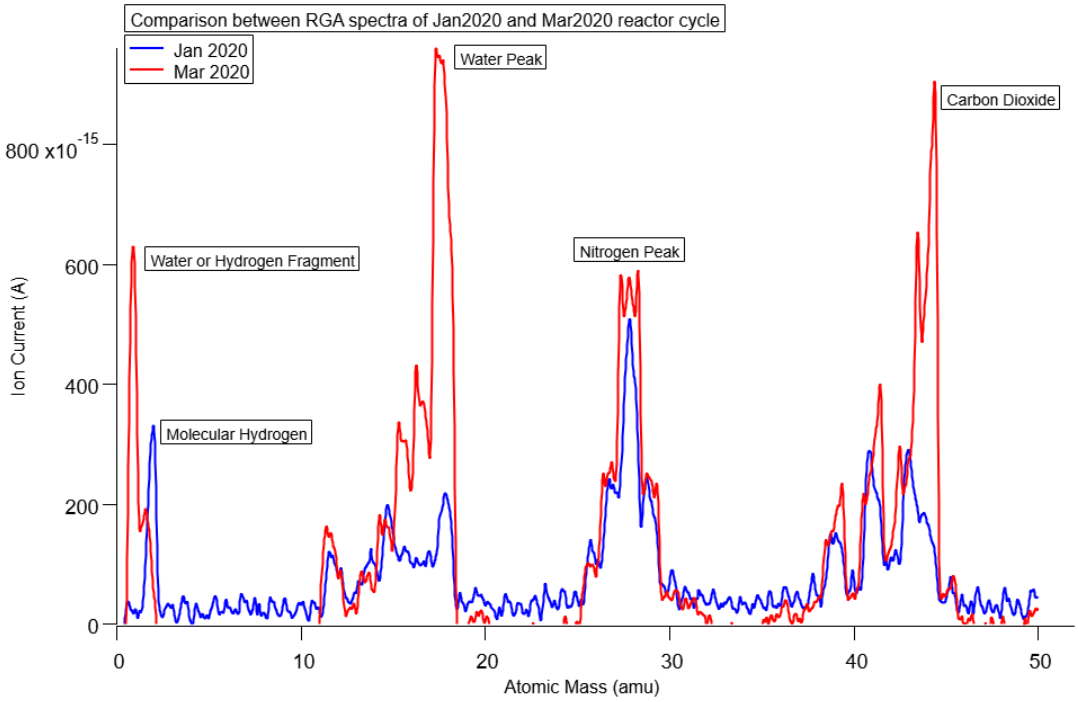

Figure 7.5: Comparison of RGA spectra taken in the January and March 2020 reactor cycles. Bonus peak events are seen in the January 2020 cycles and not seen in the March 2020 cycle.

amount of mass 2. The data from the January 2020 and March 2020 reactor cycles show a significant difference in the bonus peak fraction. The March 2020 cycle shows little evidence of a bonus peak even though the overall pressure from that cycle is higher. The January 2020 cycle shows a clear bonus peak, suggesting that the dominant gas species contributing to the bonus peak is molecular hydrogen at mass two.

The charge exchange mechanism is also dependent on the distance that the proton has traveled through the residual gas. Because the decay proton energy spectrum is always constant, the average distance traveled is proportional to the amount of time a trapped proton spends in the trap. Because of this, it is expected that the bonus peak fraction would increase linearly with trapping time. Data was successfully taken at 10 trapping times varying from 3 to 100 ms. Figure 7.6 shows a comparison of timing spectra between different trapping times, while all other experimental variables are kept the same. It can be seen that as the trapping time increases the bonus peak fraction also increases. This is consistent with what one would expect from a proton interaction with a residual gas in the trap itself. Seeing positive correlations in the data between the two variables expected to affect the probability of charge exchange gives us confidence that this is the mechanism leading to H_2^+ in the trap.

7.2.3 Energy Loss in the Proton Detector

If H_2^+ ions are being trapped, one would expect that the deposited energy of the protons and the H_2^+ ions would be slightly different because of the energy loss through the deadlayer. Using the energy spectra from different series at many different experimental configurations, a comparison of the bonus peak energy spectra can be made to that of the proton spectra. By changing the trapping time, the fraction of bonus peak events changes relative to the number of proton events in the spectra. Using this, the bonus peak energy can be isolated from the proton energy subtracting spectra with different trapping times or by isolating the bonus peak events in the timing spectra. After the bonus peak energy spectra is determined, it may be compared to simulation. The H_2^+ energy spectra are simulated using the SRIM software package. SRIM simulations were done for each apparatus configuration, for the proton at the full acceleration potential and for a proton with half the acceleration potential. We assume

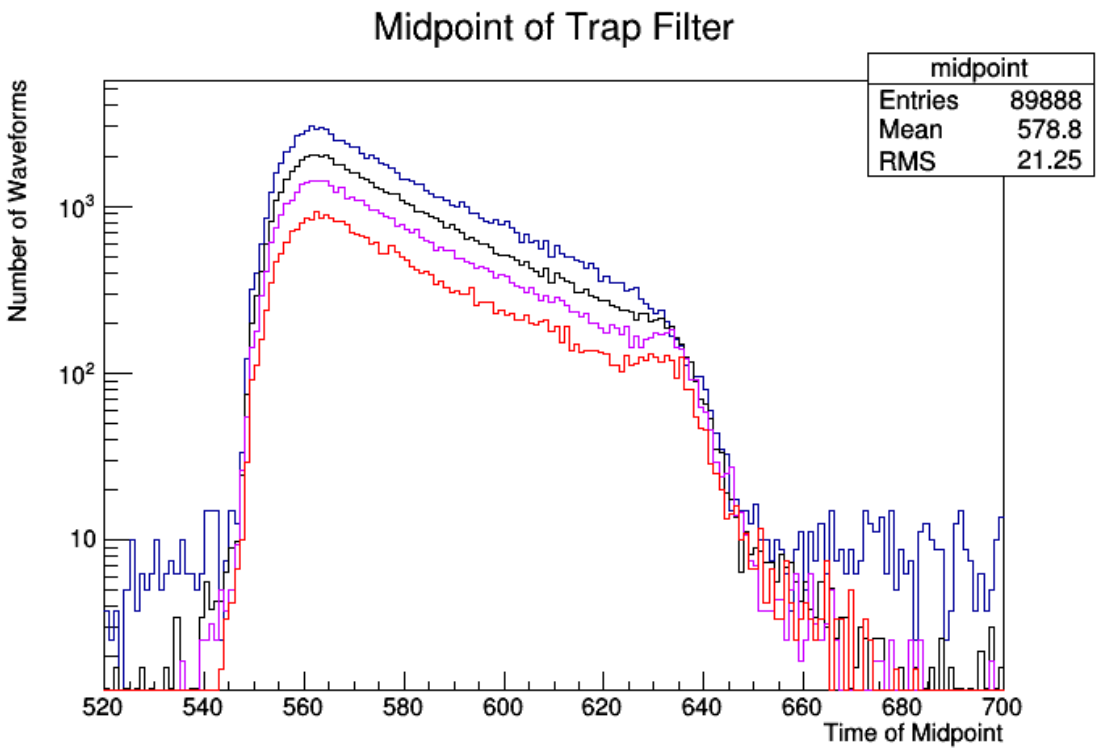

Figure 7.6: Comparison of the proton timing spectra with the Si windows closed, showing the increase in the bonus peak events with increased trapping time. Blue: 3ms, black: 10 ms, purple: 20 ms, red: 50 ms trapping time. Spectra are normalized arbitrarily so that all spectra can be seen.

that the two constituent protons of H_2^+ are loosely bound, therefore we can model H_2^+ as two independent protons each with half the energy of the acceleration potential. Each of these "half-energy" protons is then simulated so that the energy loss and backscatter fraction are determined independently. To reconstruct the full H_2^+ deposited energy, the simulated energy spectra for the half-energy protons are treated as a probability density function (PDF). Using this PDF, we use a simple Monte Carlo to select two half-energy proton energies. These two energies are then added together to make a new total energy spectrum for the H_2^+. The result is a energy spectrum that is slightly wider and lower energy than the normal proton spectrum. The resulting H_2^+ spectrum is slightly lower energy because each of the two half energy protons loses some energy through the deadlayer. Figure 7.7 shows the difference between two 2-dimensional proton energy and arrival time histograms taken with a 60 $\mu g/cm^2$ SB detector at 5 and 75 ms trapping time. Because the bonus peak fraction is larger at longer trapping times, this difference can isolate the H_2^+ peak energy. The dark blue points show where there is a deficit in the 5 ms data compared to the 75 ms data. This can be seen in two places, at $\approx 11,600$ energy and time bin ≈ 570 where the double proton peak is centered and at ≈ 4800 energy and time bin ≈ 640. This cluster, which is slightly lower in energy and later in time than the main proton peak, is the bonus peak. It can be seen that the average deposited energy of the bonus peak is about 85 % of that of the proton peak for this specific apparatus configuration. The SRIM simulation gives a deposited energy of 18.2 keV for the H_2^+ ion and a deposited energy of 20.9 keV for a proton with the same detector configuration. The deposited energy ratio of ≈ 87 % is well within the approximate range from figure 7.7. This comparison gives us confidence that the simulation does a good job at matching the relative energies of the proton and H_2^+ ion, and this matching is another piece of evidence that H_2^+ is being generated via charge exchange.

7.2.4 Change in Backscatter Fraction

Another unique characteristic observable of an H_2^+ event is a different backscatter fraction compared to the proton. Because the H_2^+ molecule is composed of two loosely bound protons, each proton acts independently as it enters the detector. Not only does each proton have energy loss through the deadlayer that leads to a slightly lower deposited energy than a single

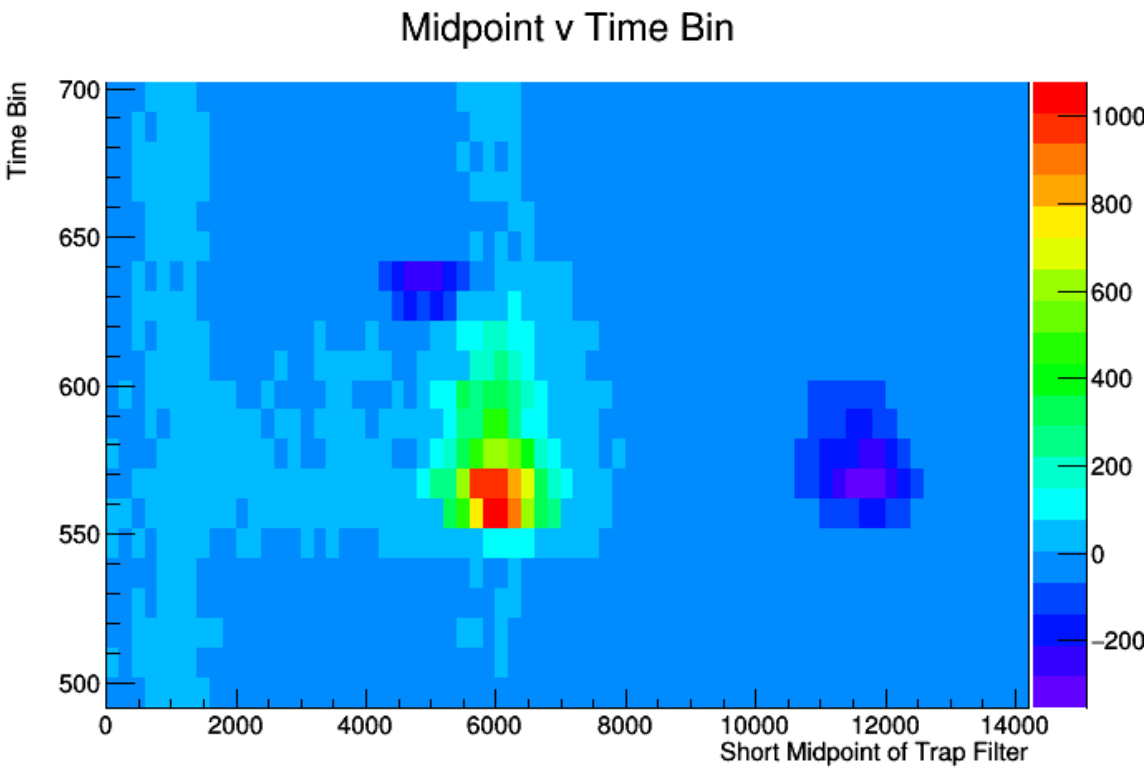

Figure 7.7: Time normalized difference between 5 ms and 75 ms proton energy and arrival time 2-dimensional histogram, showing the increase in the bonus peak at larger trapping times.

trapped proton, but it also means that both protons have a chance to backscatter. A normal trapped proton has two options after it backscatters out of the detector. It can either be re-accelerated by the electric field and return to the detector or backscatter at such an angle that it misses the detector and is completely lost. If the proton re-enters the detector it may or may not have enough energy to get completely through the deadlayer. If the proton has enough energy to get through the deadlayer, it deposits the rest of its energy into the active region leading to less deposited energy than a typical proton. The proton may also return to the detector with less energy than is needed to get through the deadlayer. In this case, the proton is completely lost. For H_2^+, each of the two protons has all of these same options. This leads to three main cases: 1) both half-energy protons from H_2^+ enter the detector on their first hit, this leads to a slightly lower energy peak than a single accelerated trapped proton, 2) both H_2^+ protons backscatter in such a way that they are both completely lost, or 3) one H_2^+ proton backscatters in such a way that it is lost and the other enters the detector on its first hit. The causes a unique feature in the bonus peak energy spectrum where there should two peaks visible, one at slightly lower energy than the main proton peak, and a second peak at roughly half the energy of the main bonus peak corresponding to only a single H_2^+ proton being detected. As the amount of bonus peak events increase with increased trapping time, this half-energy peak should become more visible. Figure 7.8 shows the proton energy spectra with time cuts made to enhance the visibility of the bonus peak.

The plot on the left is 5 ms data and the plot on the right is 75 ms data. One can see that as the trapping time increased this half-energy peak is more visible. This half-energy peak is comparable to simulation since it should be the energy of a single proton accelerated by approximately half of the nominal acceleration potential. The Monte Carlo used to generate the H_2^+ energy spectrum takes into account the probability each of the half-energy protons to backscatter or be stopped in the deadlayer. Because there are two half-energy protons incident on the detector there is some probability (this depends of the detector type and acceleration voltage) that one of the half-energy protons backscatters or is stopped in the deadlayer and the other does not. This results in a single half-energy proton depositing its energy in the active region. The SRIM + Monte Carlo H_2^+ energy spectrum encapsulates

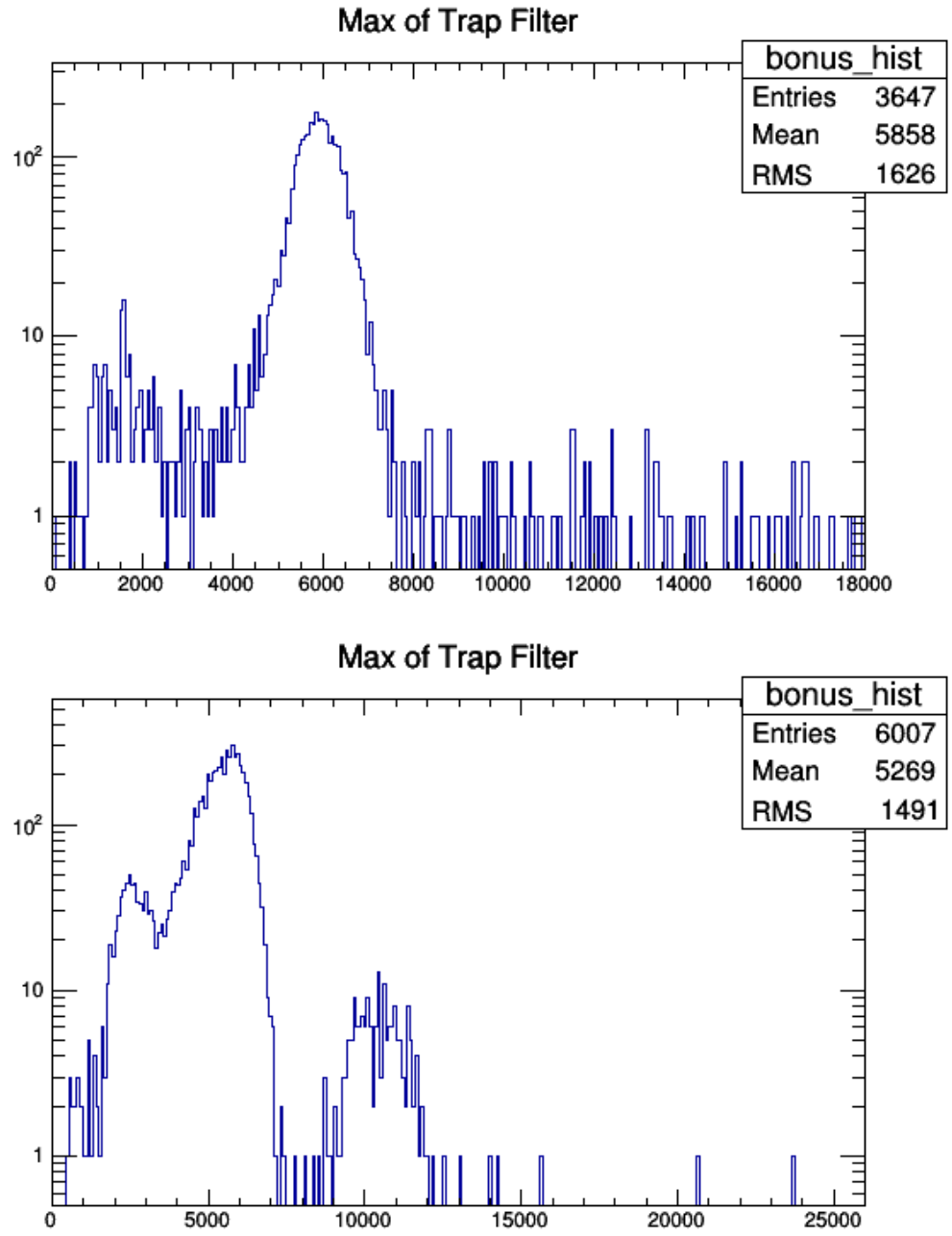

Figure 7.8: Comparison of energy spectra at 5 ms (top) and 75 ms (bottom), showing the increase of backscattered H_2^+ events with increased trapping time.

this, resulting in a main H_2^+ peak, slightly lower in energy than the normal proton peak and a half-energy peak that is caused by a single half-energy proton. While it is not possible for the simulation to give any estimate of the dependence of the half-energy peak on trapping time, one can see from figure 7.9 that the simulated half-energy peak does behave as one would expect. In figure 7.9 one can see that the half-energy peak fraction increases as the backscatter fraction of the detector increases. This is also seen in the data. The half-energy peak is much more difficult to identify with PIPS detector data than for SB detector data because the smaller backscatter fraction suppresses this peak.

7.2.5 Better Matching to Energy Spectra

Because the H_2^+ ion arrives at the proton detector in a time range overlapping with the trapped protons, the energy spectra of the two are practically impossible to disentangle. Therefore, the measured energy spectra should be some combination of the proton energy spectra and the H_2^+ energy spectra.

The SRIM + Monte Carlo H_2^+ energy spectra, as well as the normal proton spectra, can be compared to the analyzed energy spectra. One would expect that if H_2^+ was present in the trap some admixture of the H_2^+ and proton spectra would best fit the data. Two test cases are examined here, one with a negligible amount of bonus peak visible (PIPS detector) and one with a large amount of bonus peak visible (100 $\mu g/cm^2$ SB detector). To do this, noise must be added to the simulated spectra to match the width of the data. Approximately 1.3 keV of Gaussian noise is added to both the H_2^+ and the proton spectra. The same 1.3 keV of added width makes a good match to most of the data, suggesting that the noise is rather stable over long periods of running. After the noise is added, the simulated spectra may be compared directly to the data.

As seen in figure 7.10, the normal proton simulation (blue) agrees with the data (red) in the central peak region as well as the high energy shoulder of the peak. However, it starts to deviate from the data on the low energy shoulder and the low energy tail. It can also be seen that the H_2^+ spectra does not do a good job by itself of matching the data spectra, suggesting that if H_2^+ is present in the proton trap, it makes up a relatively small fraction of the total events. It can also be seen in figure 7.10 that the half-energy peak

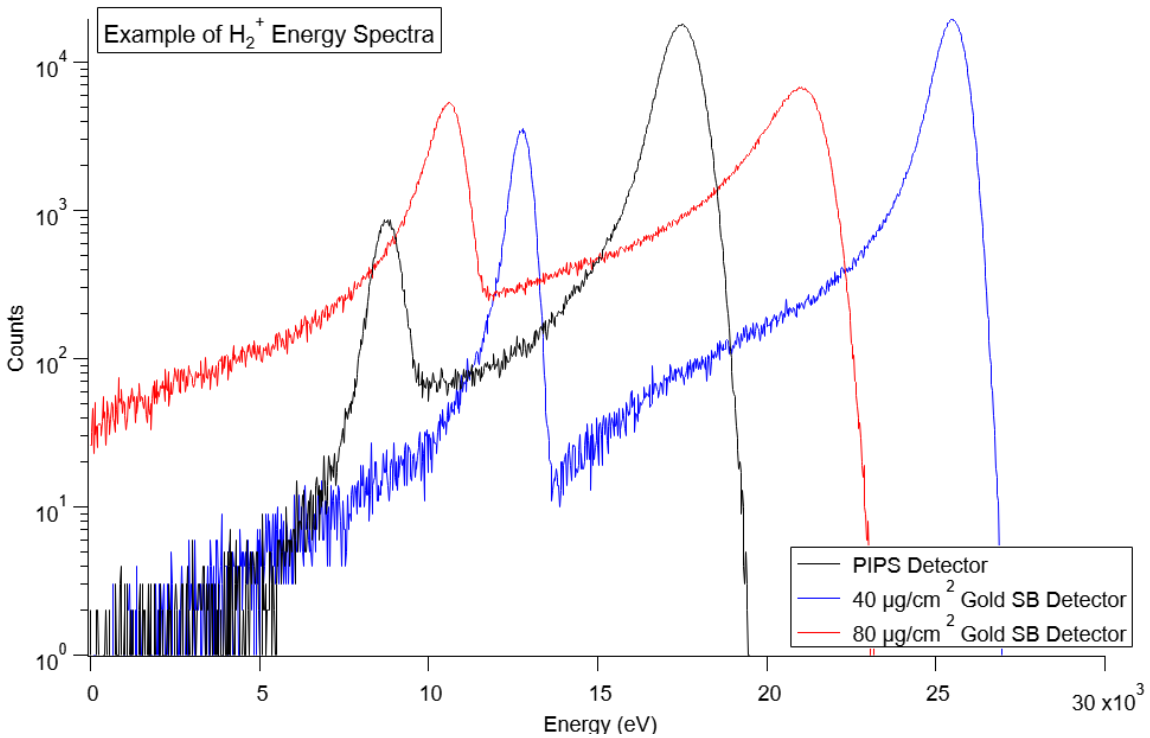

Figure 7.9: Example of simulated H_2^+ energy spectra for three different detector types.

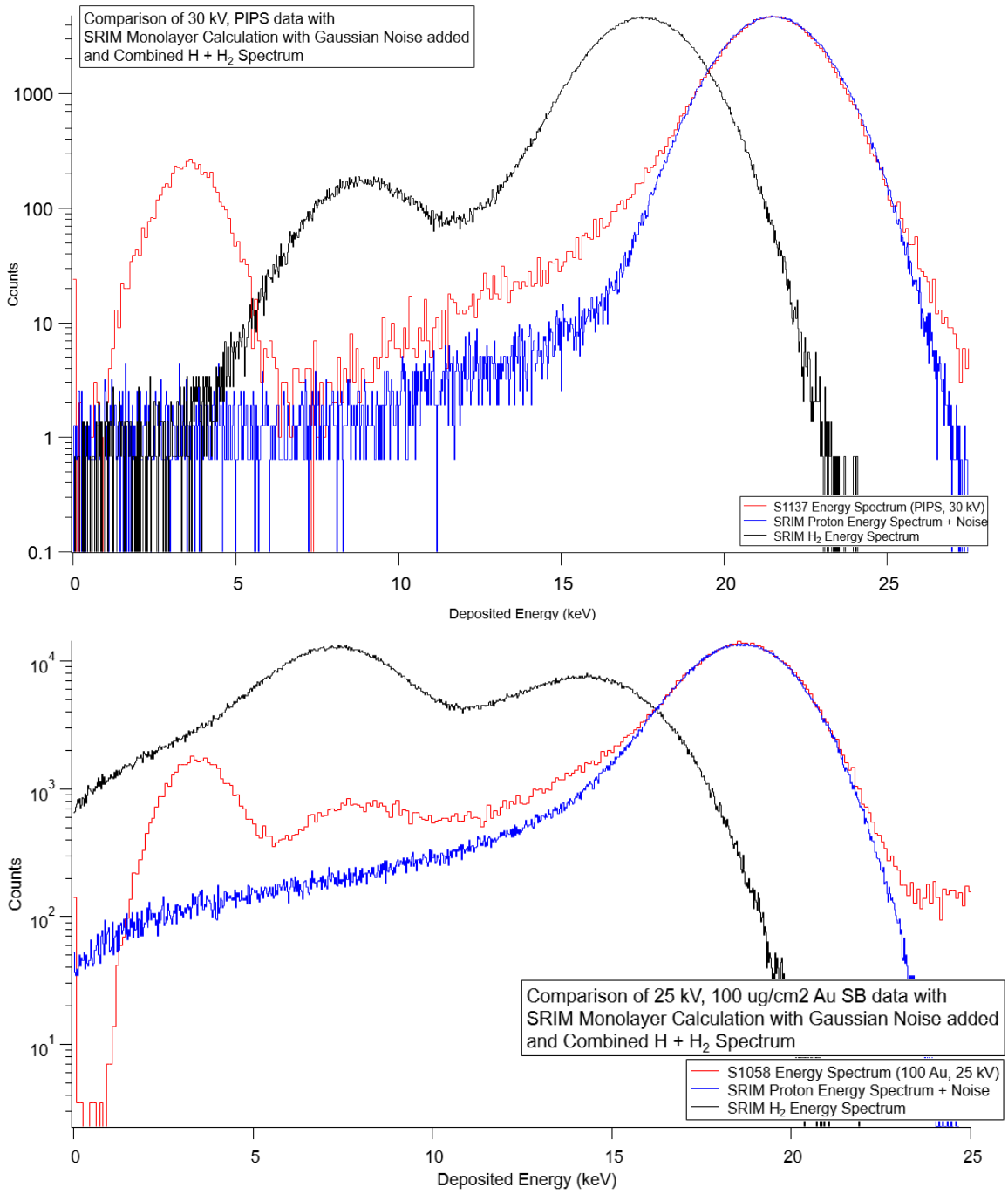

Figure 7.10: Top: Comparison of PIPS detector data (red) with the SRIM simulated energy spectra of the proton (blue) and H_2^+ (black). Bottom: Comparison of 100 $\mu g/cm^2$ SB detector data (red) with the SRIM simulated energy spectra of the proton (blue) and H_2^+ (black). Both plots illustrate that the proton spectra alone is not sufficient to match the data.

of the H_2^+ spectra varies significantly depending on the apparatus configuration. Because the half-energy peak is caused by one backscattered half-energy proton, the probability of a half-energy event increases when the backscatter fraction of the half-energy proton increases. From those plots it can be seen that with the PIPS detector the small backscatter fraction causes a small half-energy peak. The 100 $\mu g/cm^2$ SB detector has the highest backscatter fraction of any detector used in the experiment. The probability that a half-energy proton is not transmitted into the active region with this detector is $> 30\,\%$, thus the size of the half-energy peak is larger than that of the full energy H_2^+ peak.

Using the simulated proton and the H_2^+ energy spectra, an admixture of the two can now be generated to try and mimic the data with a single free parameter. This "combined" energy spectrum is generated by taking a small amount of the H_2^+ spectrum and adding it to the normal proton spectrum until the best match to the data is achieved. This is done independently for each series. As seen in figure 7.11, the combined energy spectra fits the data much better than the proton spectrum alone. This is yet another indication that there is some H_2^+ in the proton trap, and the H_2^+ is easily detected because of the accelerating potential. The total amount of H_2^+ in the combined spectrum admixture is $\approx 2.5\%$ for the PIPS detector comparison, and is $\approx 5.0\%$ for the SB detector comparison. Above, it was stated that the PIPS detector data had a "negligible amount of bonus peak visible," but the admixture spectra suggests that there is only a factor of 2 less H_2^+ in the data than the SB detector data. The keyword is "visible," during standard diagnostic checks on the data, the tell-tale sign of bonus peak in the data is the half-energy peak. Because the backscatter fraction is significantly smaller with the PIPS detector, the half-energy peak is highly suppressed compared to the full energy H_2^+ peak. This means that even when the half-energy peak is not easily visible that does not mean there is no H_2^+ present in the data. A more careful comparison of the spectral shapes, like the examples in figure 7.10, is necessary to determine whether or not there is H_2^+ in the data.

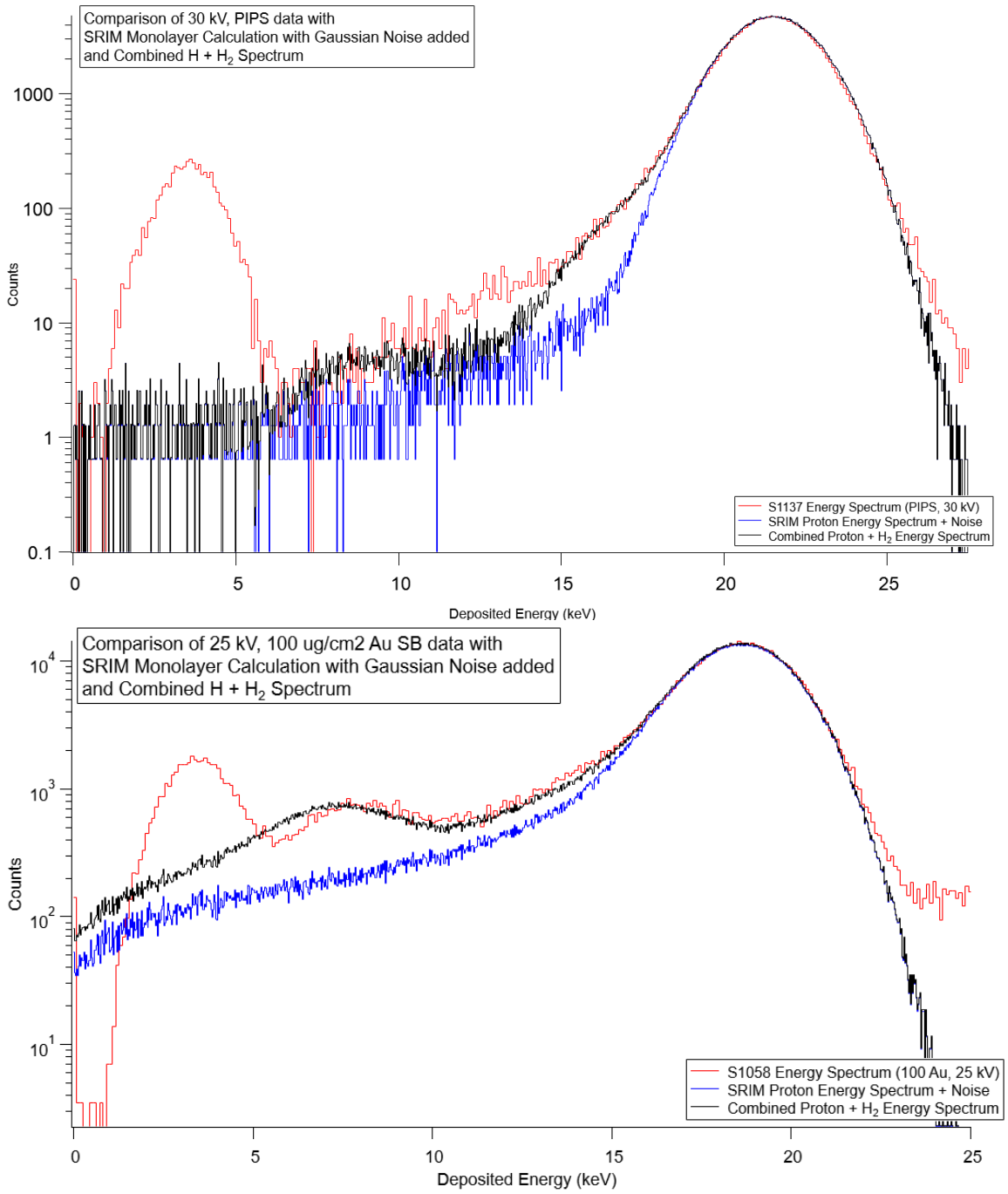

Figure 7.11: Top: Comparison of PIPS detector data (red) with the SRIM simulated energy spectra of the proton (blue) and combined admixture of the proton and 2.5% H_2^+ spectra (black). Bottom: Comparison of 100 $\mu g/cm^2$ SB detector data (red) with the SRIM simulated energy spectra of the proton (blue) and combined admixture of the proton and 5% H_2^+ spectra (black). Both plots illustrate that combined spectra fit the data much better than the proton spectra alone.

7.3 Determination of the Detection Efficiency

As described above, there is ample of evidence that H_2^+ is being created via charge exchange with a trapped proton and that the H_2^+ is being detected. The question remains, what effect does that have on the measured neutron lifetime? To answer this question, one must calculate what the detection efficiency for trapped H_2^+ ions would be for a wide range of apparatus configurations. To do this following the same method for correcting the proton rate in BL1, one must calculate the Rutherford backscatter fraction, f_{ruth}, the fraction of events stopped in the deadlayer, f_{stp}, and the events below threshold, f_{BT} with simulation. The detection efficiency for protons is given by:

$$\epsilon_p = 1 - f_{ruth}(p) - f_{stp}(p) - f_{BT}(p), \quad [1] \tag{7.3}$$

where there are three possibilities for a proton to go undetected. However, because H_2^+ is modeled as two independent protons, this simple calculation is not valid. There are now three possibilities for each of the H_2^+ protons to go undetected, for a total of nine distinct outcomes for the two protons. The two protons are identical so the probability for these events are the same which simplifies the calculation. Nevertheless, "cross terms" exist where the two protons have different outcomes. Take for example, an H_2^+ ion where one of the protons backscatters but the other deposits its full energy in the active region. This event would only go undetected if the deposited energy were below threshold. The complete list of H_2^+ ion possibles can be seen in table 7.1. When adding the two half energy protons together with the previously described Monte Carlo, the probability for a single proton to backscatter or be stopped in the deadlayer is taken into account. Therefore, the five outcomes in table 7.1 that include the fraction of transmitted events, $f_X(H_2)$, are consolidated by looking at the simulated H_2^+ energy spectrum. An example of the typical proton threshold used in analysis overlaid on simulated H_2^+ spectra can be seen in figure 7.12. $f_{BT}(H_2)$ is calculated by taking the fraction of events to the left of the threshold seen in figure 7.12 and dividing it by the total number of simulated events. As a result, the detection efficiency for an H_2^+

[1] In [67] there is also a given fraction for the protons that backscatter off the active region of the detector and do not deposit energy above threshold f_{act}. As discussed in section 6.6, f_{act} requires doubling the amount of simulations and gives a negligible change to the neutron lifetime so it has been excluded.

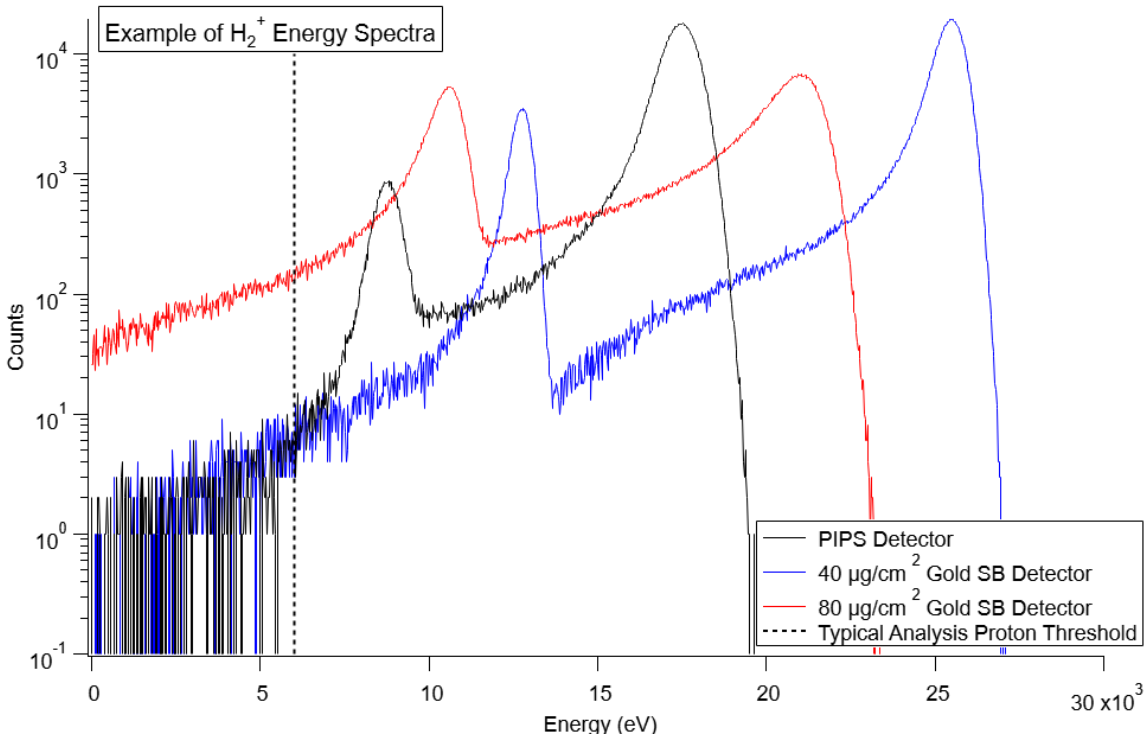

Figure 7.12: Example of simulated H_2^+ energy spectra for three different detector types, showing a typical analysis threshold.

Table 7.1: 9 possible outcomes for a H_2^+ ion to be undetected. Events that enter the active region may be undetected if they are below threshold.

proton outcome	Backscattered	Stopped in Deadlayer	Enters Active Region
Backscattered	$f_{ruth}(H) * f_{ruth}(H)$	$f_{stp}(H) * f_{ruth}(H)$	$f_X(H) * f_{ruth}(H)$
Stopped in Deadlayer	$f_{ruth}(H) * f_{stp}(H)$	$f_{stp}(H) * f_{stp}(H)$	$f_X(H) * f_{stp}(H)$
Enters Active Region	$f_{ruth}(H) * f_X(H)$	$f_{stp}(H) * f_X(H)$	$f_X(H) * f_X(H)$

ion is given by:

$$\epsilon_{H_2} = 1 - f_{ruth}(H_2) - f_{stp}(H_2) - 2(f_{ruth}(H) f_{stp}(H)) - f_{BT}(H_2), \tag{7.4}$$

where $f_{ruth}(H_2)$ is the fraction of H_2^+ events that have both half-energy protons backscatter, $f_{stp}(H_2)$ is the fraction of H_2^+ events that have both half-energy protons stop in the deadlater, $f_{ruth}(H)$ is the fraction of a half-energy events that backscatter, $f_{stp}(H)$ is the fraction of half-energy events that stop in the deadlayer and $f_{BT}(H_2)$ is the fraction of H_2^+ events that are below threshold. This method has been used to calculate ϵ_{H_2} for all possible detector and acceleration voltage configurations. A collection of the of the given fs and the detection efficiencies for the proton and the H_2^+ ion can be seen in tables 7.2 and 7.3, respectively.

As can be seen in the tables, for the PIPS detector and SB detectors with Gold layers of $60\,\mu g/cm^2$ and below, the difference in the detection efficiencies are $< 1.5\%$. It is not until the gold deadlayer becomes relatively thick and the backscatter fraction large that there are large differences in the detection efficiency. This gives us two insights. The first is a run planning insight: to avoid large differences in detection efficiency, it is best to avoid using $100\,\mu g/cm^2$ SB detectors, and $80\,\mu g/cm^2$ SB detectors should be run at acceleration voltages of 30 kV or larger. The second insight is an indication of how the neutron lifetime would be affected by the presence of H_2^+. For the vast majority of the apparatus configurations, there is little change to the neutron lifetime when compared to the total uncertainties of previous measurements of this type. As an example, let us consider a case where 5% of the trapped events are H_2^+ ions for a $60\,\mu g/cm^2$ SB detector at 30 kV. In this scenario, the detection efficiency difference is 1.07%, this would equate to a change in the measured neutron lifetime of $\approx 0.5\,s$ or a relative change of $\approx 0.06\%$.

Table 7.2: SRIM input parameters (left) and output results (right) for the determination of proton detection efficiencies.

Au ($\mu g/cm^2$)	$E_{sim}(p)$ (keV)	E_{thresh} (keV)	$f_{ruth}(p)$ (keV)	$f_{BT}(p)$ (%)	$f_{stp}(p)$ (%)	ϵ_p (%)
0	25	6.0	0.2744	0.0951	0.1019	99.5286
0	27.5	6.0	0.2223	0.0656	0.0674	99.6447
0	30	6.0	0.1889	0.0432	0.0487	99.7192
0	32.5	6.0	0.1591	0.0319	0.0356	99.7734
0	35	6.0	0.1322	0.0240	0.0254	99.8184
20	25	6.0	0.8312	0.0006	0.0000	99.1682
20	27.5	6.0	0.6911	0.0003	0.0000	99.3086
20	30	6.0	0.5891	0.0002	0.0000	99.4107
20	32.5	6.0	0.5180	0.0000	0.0000	99.4820
20	35	6.0	0.4443	0.0001	0.0000	99.5556
40	25	6.0	1.9565	0.0310	0.0019	98.0106
40	27.5	6.0	1.6206	0.0168	0.0004	98.3622
40	30	6.0	1.3898	0.0106	0.0005	98.5991
40	32.5	6.0	1.1674	0.0055	0.0004	98.8267
40	35	6.0	1.0247	0.0031	0.0001	98.9721
60	25	6.0	3.4607	0.2071	0.0433	96.2889
60	27.5	6.0	2.8517	0.1214	0.0273	96.9996
60	30	6.0	2.3728	0.0721	0.0165	97.5386
60	32.5	6.0	2.0273	0.0466	0.0117	97.9144
60	35	6.0	1.7492	0.0307	0.0075	98.2126
80	25	6.0	5.2507	0.6016	0.3187	93.8290
80	27.5	6.0	4.3362	0.3647	0.2030	95.0961
80	30	6.0	3.6404	0.2450	0.1390	95.0961
80	32.5	6.0	3.0984	0.1690	0.0831	96.6495
80	35	6.0	2.6553	0.1108	0.0577	97.1762
100	25	6.0	7.0557	1.3017	1.1730	90.4696
100	27.5	6.0	5.8895	0.8537	0.7750	92.4818
100	30	6.0	4.9691	0.5709	0.5317	93.9283
100	32.5	6.0	4.2546	0.3907	0.3783	94.9764
100	35	6.0	3.6033	0.2847	0.2530	95.8590

Table 7.3: SRIM input parameters (left) for the half-energy H^+ simulations used to determine the detection efficiencies for H_2^+. Output results (right) for the determination of H_2^+ detection efficiencies using the Monte Carlo method described in the text.

Au ($\mu g/cm^2$)	$E_{sim}(H)$ (keV)	E_{thresh} (keV)	$f_{ruth}(H_2)$ (%)	$f_{BT}(H_2)$ (%)	$f_{stp}(H_2)$ (%)	$2(f_{ruth}(H)f_{stp}(H))$ (%)	ϵ_{H_2} (%)
0	12.5	6.0	0.0129	1.7950	0.0186	0.0310	98.1425
0	13.75	6.0	0.0090	0.5251	0.0088	0.0179	99.4391
0	15.0	6.0	0.0065	0.1330	0.0045	0.0108	99.8452
0	16.25	6.0	0.0046	0.0387	0.0023	0.0066	99.9478
0	17.5	6.0	0.0035	0.0156	0.0013	0.0043	99.9753
20	12.5	6.0	0.0784	0.0091	0.0000	0.0000	99.9125
20	13.75	6.0	0.0577	0.0039	0.0000	0.0000	99.9384
20	15.0	6.0	0.0419	0.0014	0.0000	0.0000	99.9567
20	16.25	6.0	0.0311	0.0007	0.0000	0.0000	99.9682
20	17.5	6.0	0.0242	0.0004	0.0000	0.0000	99.9754
40	12.5	6.0	0.4964	0.2768	0.0001	0.0116	99.2151
40	13.75	6.0	0.3598	0.1360	0.0000	0.0060	99.4982
40	15.0	6.0	0.2636	0.0724	0.0000	0.0034	99.6606
40	16.25	6.0	0.1999	0.0381	0.0000	0.0018	99.7602
40	17.5	6.0	0.1568	0.0236	0.0000	0.0012	99.8184
60	12.5	6.0	1.4356	1.9343	0.0176	0.3177	96.2948
60	13.75	6.0	1.0761	0.9279	0.0075	0.1803	97.8082
60	15.0	6.0	0.8022	0.5015	0.0032	0.1018	98.5912
60	16.25	6.0	0.6084	0.2990	0.0016	0.0621	99.0289
60	17.5	6.0	0.4716	0.1804	0.0008	0.0394	99.3078
80	12.5	6.0	2.5201	7.7788	0.3271	1.8159	87.5581
80	13.75	6.0	2.0011	3.7027	0.1670	1.1561	92.9731
80	15.0	6.0	1.5775	2.0014	0.0877	0.7438	95.5897
80	16.25	6.0	1.2515	1.1824	0.0458	0.4789	97.0414
80	17.5	6.0	1.0058	0.7218	0.0259	0.3228	97.9237
100	12.5	6.0	3.2207	21.8126	1.9545	5.0180	67.9942
100	13.75	6.0	2.7132	11.1364	1.1587	3.5462	81.4454
100	15.0	6.0	2.2422	5.9109	0.6722	2.4554	88.7192
100	16.25	6.0	1.8817	3.4424	0.3980	1.7307	92.5473
100	17.5	6.0	1.5603	2.1283	0.2389	1.2210	94.8516

Chapter 8

Conclusion

8.1 Results

8.1.1 Updated Determination of the Proton Backscatter Extrapolation for BL1 Data

With the use of the new monolayer calculation model, the BL1 backscatter extrapolation can be recalculated. All nine different apparatus configurations used in the final result for the BL1 experiment have been re-simulated using the SRIM monolayer damage calculation model with at least a factor of three higher stats. This allows for a re-examination of the BL1 final result with a simulation model that is better tailored to the physical conditions of the experiment. With the updated simulation, a new f_{ruth}, f_{BT}, and f_{stp} were determined for each apparatus configuration; f_{act} has been neglected. Looking at the previous BL1 simulation results P_{bk} was dominated by f_{ruth}, and neglecting f_{act} only resulted in a 0.1 s change in the determined neutron lifetime.

The neutron lifetime, $\tau_{BL1update}$ for all 13 separate BL1 series were taken from table V in reference [67], from that point on, the new simulation is independent of the BL1 result. Because the monolayer damage calculation results in a much narrower proton peak, the output energy spectra must be corrected for the energy resolution in the BL1 experiment. According to reference [67], the energy resolution was approximately 6 keV FWHM during the BL1 experiment. Gaussian noise was added to the simulated energy spectra so that

a Gaussian fit to the central peak region has a width of approximately 2.5 keV, which corresponds to ≈6 keV FWHM. Then, using the method described in sections 6.6 and 6.7, f_{ruth}, f_{BT}, and f_{stp} were determined for each series. The new simulation method does show substantial differences in resulting values. For all instances, the new method showed fewer protons being stopped in the deadlayer of the detector and slightly fewer events below threshold. This results in a smaller fraction of undetected protons by about a factor of 3. From there, $\tau_{nBL1update}$ is corrected for the fraction of undetected protons:

$$\tau_{BL1update_{undet}} = \tau_{BL1update}\left(\frac{1}{1+(\frac{f_{BT}+f_{stp}}{100})}\right). \tag{8.1}$$

Now that the lifetime is corrected for undetected protons, the lifetime must be corrected for backscattered protons. The new simulation also shows a difference in the backscatter fraction for the configurations used in the BL1 experiment. f_{ruth} is larger for all configurations by up to 10%. Now $\tau_{BL1update_{undet}}$ is plotted against f_{ruth} and fit to a linear function. This fit may now be directly compared to the BL1 results, where the y-intercept is the neutron lifetime corresponding to zero backscatter. Ignoring f_{act} and redoing the exact same analysis from reference [67], one obtains a neutron lifetime of 886.72 ± 1.2 s with a χ^2 of 0.69 per degree of freedom for 11 degrees of freedom. For the updated SRIM monolayer simulation, the extrapolated lifetime is 886.69 ± 1.16 s with a χ^2 of 0.63 per degree of freedom with the same 11 degrees of freedom. The results of these data can be seen in figure 8.1. The slightly smaller uncertainty in the new result is caused by the larger backscatter fraction leading to a larger lever arm of the fit. Despite the noticeable changes in proton events that stopped in the deadlayer and the number of events that were backscattered using the new simulation model, these two almost perfectly account for each other and cause no change to the resulting lifetime. The monolayer simulation model is still preferred, however, because it better models the interactions in thin material layers and results in a much narrower proton energy spectra that one would expect before taking into account detector noise.

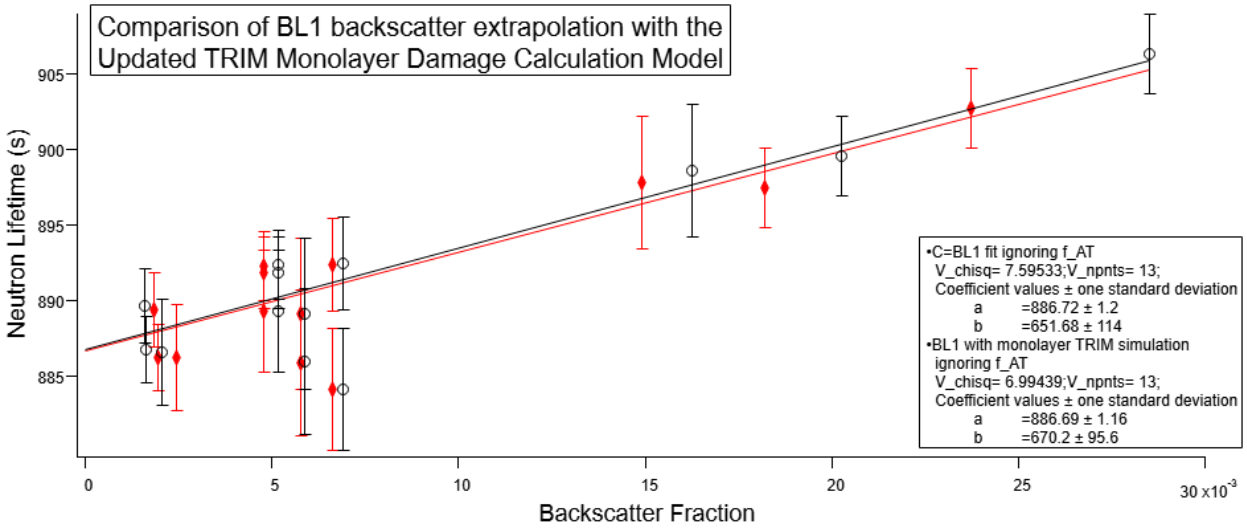

Figure 8.1: Comparison of the previous BL1 backscatter extrapolation neglecting f_{act} (red diamonds) and the updated results using the monolayer damage calculation model in SRIM (black open circles). This more appropriate simulation model shows no change in the extrapolated neutron lifetime.

8.1.2 Previously Inaccessible Systemic Tests

The in-beam method of the neutron lifetime is a systematically limited measurement. One of the major goals of the BL2 experiment was to search for new systematic effects that could possibly affect the neutron lifetime. One of the biggest questions about this experimental method is the possibility of protons escaping the trap. In the BL1 experiment, the apparatus was only able to run stably at trapping times of 5 ms and 10 ms, and the vast majority of data used in the final analysis was taken at 10 ms. With the design and installation of the cold bore isolation thin silicon windows, the BL2 experiment is now able to run stably between 3 and 100+ ms. This is well over an order of magnitude improvement in the range of possible trapping times compared to BL1. While more data still needs to be taken and conclusions from the data that have been taken are difficult to make, the ability to explore this effect is a major step forward in understanding this experimental method.

One of the largest systematic effects that must be accounted for is the different detection efficiencies of the proton detector depending on the detector type, deadlayer, and acceleration voltage. A new simulation model was used that provides a more believable understanding of the proton detection efficiencies over a wide range of configurations. As discussed in chapter 7, it is believed that charge exchange with molecular hydrogen is occurring. Seeing these H_2^+ ions in the data and seeing positive correlations with trapping time and pressure allows for a new systematic test to be explored. The detection efficiency for H_2^+ has been compared to the proton detection efficiency over all possible apparatus configurations. It has been shown that for the vast majority of configurations the difference in the detection efficiency is small. Through fits to the proton spectrum shape we see a sizable fraction of H_2^+ events in the data. However, the high detection efficiency of H_2^+ for the majority of apparatus configuration show that these events would lead to a minimal correction to the neutron lifetime. Furthermore, the high detection efficiency of H_2^+ ions show that this is effect is not a viable explanation for the difference in the average measured lifetimes between the beam and bottle methods.

8.2 Continued Data Taking

While data taking began in 2017 and continued through 2019, data taking in 2020 and 2021 was erratic at best. The March 2020 reactor cycle was cut short by the onset of the Covid-19 pandemic and the reactor did not run for months thereafter. From July 2020 until November 2020, reactor cycles were completed, but with minimal staffing. Because of the staffing requirements, the typical run configuration scheduling was not possible. Another Covid-19 pause in the reactor schedule occurred from December 2020 to January 2021. In February 2021, during reactor start-up, elevated levels of radiation were detected and the reactor was shut down. For an overview of the incident, one can see the Nuclear Regulatory Commission's report at https://www.nrc.gov/reactors/non-power/event-at-nist.html. From February 2021 until present, the reactor has been shut down and no new data collection has been possible. NIST currently gives a "no earlier than" start date for the reactor of July 2022. Further complicating the schedule, a planned cold source upgrade that begins in December 2022 and will last approximately one year. While the NIST is confident that the reactor will restart before this extended shutdown, it remains to be seen how much data taking will be possible. We have tentatively laid out a plan for approximately half a year's worth of data, broken into three reactor cycles. With the Mark III trap installed we plan to use the first half of the first cycle to quickly re-do some systematic tests that were previously done with the Mark II trap. These include checking the magnetic field linearity like in section 6.1, the unloading efficiency as a function of ramp voltage like in section 6.2, and the trapping efficiency as a function of door/mirror voltage like in section 6.3. The last half of the first cycle is planned to be devoted to proton trapping time effects like in section 6.5. The second cycle will be solely used to collect high statistics neutron lifetime data primarily with a PIPS detector. The third cycle plans to use the first half for neutron lifetime data with primarily an SB detector and the second half for neutron systematic tests, like those covered in [67, 3, 108]. Significant effort has been made to optimize the data taking run plan for such a short period of time, with the hope of completing a neutron lifetime measurement that is still useful to the community despite the disruptions in data taking.

8.3 Future Experiments

The BL2 apparatus uses re-purposed equipment that was designed for a smaller, less intense neutron beam; as such is not able to take full advantage of the NG-C beamline. The output of the NG-C neutron beamguide is an 11 cm x 11 cm square, however, the size constraints of the BL2 superconducting magnet require the beam collimator to be about 7 mm. A proposed experiment, called BL3, plans to take advantage of the high flux NG-C beamline by using all new equipment designed for a large area neutron beam. The designed BL3 magnet allows for beam collimator of 35 mm, an increase of over 20 times in beam area. The proton trapping region is also 2 times longer. With reactor upgrades and optimized collimation the neutron flux is expected to increase up to a factor of 4. These upgrades are expected to increase the proton rate by ≈ 90 times. Figure 8.2 shows a size comparison of a Mark III trap electrode currently used in BL2 and a BL3 test electrode blank.

The increased beam size will require a more sophisticated proton detection system. The proposed detector design is a 10 cm diameter pixelated solid silicon detector. The pixelation serves multiple purposes. Each pixel serves as its own individual detector, so a smaller pixel area decreases detector noise due to capacitance. The small pixels also keep the proton rate per pixel at a level where active multiple proton identification as described in section 4.2 is still possible.

Another major proposed upgrade is to create an Alpha-Gamma 2 (AG2) device that will calibrate the BL3 $1/v$ neutron fluence monitor. AG2 plans to run with an increased beam diameter of 35 mm compared to the current 10 mm diameter beam and increase the number of gamma detectors from 2 to 8. These upgrades will provide an almost 100x increase in total gamma count rate. AG2 also plans to have an in situ deposit holder for multiple different targets. As discussed in section 5.1, it is necessary to swap between thin and thick boron targets to account for drifts in the detection efficiency. This is currently a time consuming process as the vacuum system must be opened and closed every time there is a swap. With the proposed AG2 design there will be no need to open the vacuum system when swapping between deposits. With these rate increases and additional upgrades, it is estimated that the BL3 will be able to measure the neutron lifetime to better than the

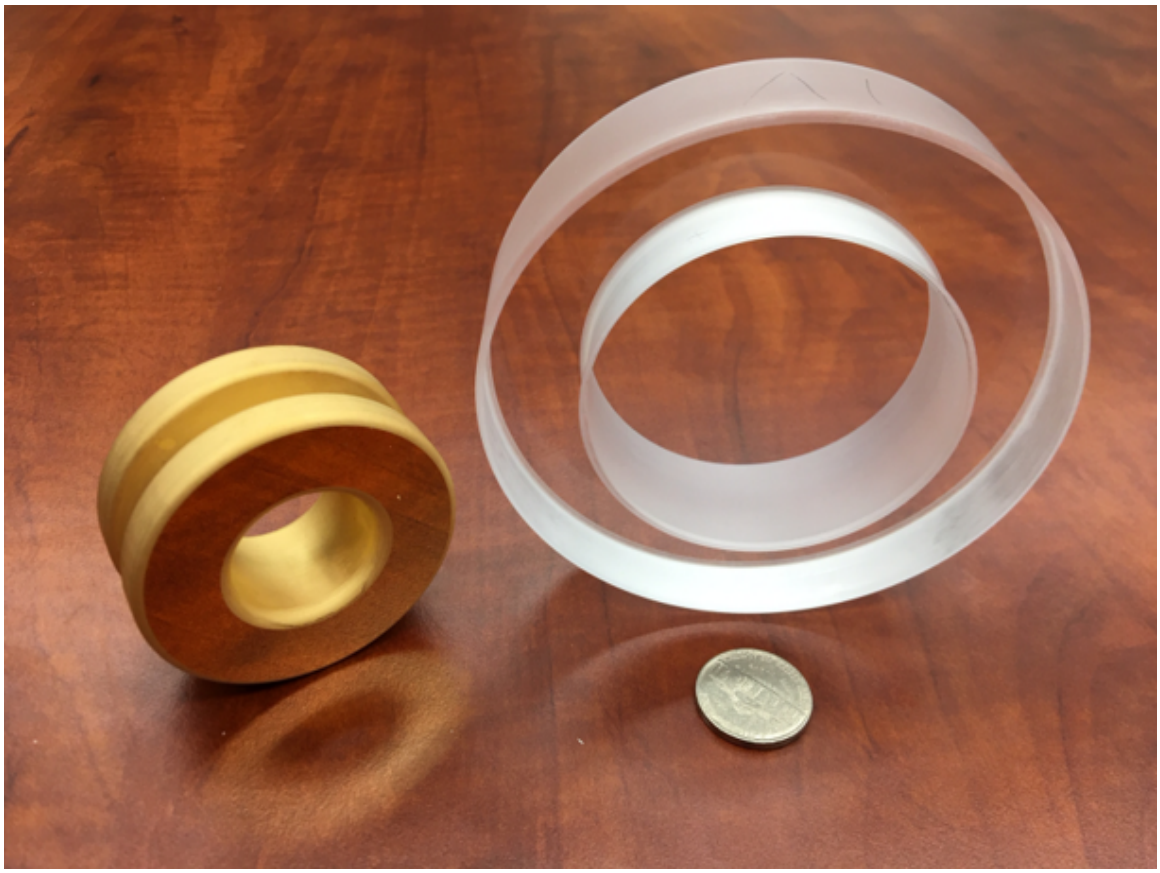

Figure 8.2: Comparison between a Mark III trap electrode and an electrode test blank for the proposed BL3 experiment.

1 s level every day. With this statistical power, a wide range of systematic tests can be performed quickly and with a precision never before achieved. The BL3 experiment hopes to have a fully operable apparatus by the end of 2025 and start running shortly thereafter with the ultimate uncertainty goal of measuring the neutron lifetime to a precision of $< 0.3\,s$, comparable to the most precise measurements to date.

8.4 Summary and Conclusion

The goal of this work was to develop a new analysis method with improved energy resolution and noise suppression, and to explore systematic tests with the in-beam measurement of the neutron lifetime. The former was accomplished by optimizing and implementing a finite response trapezoid filter for proton waveform analysis. This software filter allows for the optimization of filter parameters to suit the specific analysis needs and experimental conditions. Optimizing the trapezoid filter parameters improved the energy resolution of the analyzed proton energy spectrum and now allows for an absolute timing comparison to simulation that was not previously possible. The improved energy resolution also allows for waveform by waveform multiple proton identification. This method can now be used along side the typical Poisson statistical method used in this type of experiment. Using both methods to extract the proton rate gives a cross-check of analysis methods and increases the confidence in results.

Many systematic tests have been carried out over the course of this work. The systematic tests of the proton detector alignment and the dependence of the proton rate on the magnetic field showed that the neutron beam and magnetic field shapes are well understood. The implementation of a trap positioning piece, as well as better understanding of how the magnetic field shape affects the data, will significantly improve the systematic uncertainty for that effect. Tests of the quasi-Penning electrode trap unloading and trapping efficiencies showed that the trapping voltages are well understood and agree well with applicable simulation. It is believed no correction will be required for these effects. With the installation of the cold bore isolating silicon windows, data was taken over almost two orders of magnitude in trapping time. This has never before been achieved and allows for tests of previously

inaccessible systematic effects. While conclusions from tests of proton trapping time effects require additional data, the ability to make these measurements is a break through for the experimental method.

Charge exchange resulting in H_2^+ ions in the trap has been observed. A never before used SRIM damage calculation package, that is more applicable to the conditions of the experiment, showed good comparison to data. With this simulation, it was shown that the simulated proton energy spectrum alone was not enough to match the data. A small fraction of the H_2^+ ions energy spectrum added to the proton energy spectrum provided a much better match to data. The H_2^+ ion's detection efficiency has been calculated for all possible apparatus configurations and found to be within 1.5 % of the proton detection efficiency for the vast majority of likely apparatus conditions. Comparison of data and simulation show that the detection efficiency of H_2^+ ions is sufficiently high and the relative fraction low as to not make a significant impact on the measured neutron lifetime. Using this new simulation method, the previous BL1 backscatter extrapolation was re-simulated and re-analysed. Significant changes in the fraction of protons that backscatter or stop in the deadlayer were observed for some detector configurations, however, these differences resulted in no change to the extracted neutron lifetime.

Bibliography

[1] Allison, S. K. (1958). Experimental results on charge-changing collisions of hydrogen and helium atoms and ions at kinetic energies above 0.2 kev. *Rev. Mod. Phys.*, 30:1137–1168. 126, 128

[2] Amhis, Y. S. et al. (2021). Averages of b-hadron, c-hadron, and τ-lepton properties as of 2018. *Eur. Phys. J. C*, 81(3):226. 13

[3] Anderson, E. (2017). *Precision Neutron Flux Measurement and Advancement Using the Alpha Gamma Technique*. PhD thesis, The University of Indiana. x, 35, 49, 154

[4] Antonelli, M. et al. (2010). An Evaluation of $|V_{us}|$ and precise tests of the Standard Model from world data on leptonic and semileptonic kaon decays. *Eur. Phys. J. C*, 69:399–424. 13

[5] Arzumanov, S., Bondarenko, L., Chernyavsky, S., Geltenbort, P., Morozov, V., Nesvizhevsky, V., Panin, Y., and Strepetov, A. (2015). A measurement of the neutron lifetime using the method of storage of ultracold neutrons and detection of inelastically up-scattered neutrons. *Physics Letters B*, 745:79–89. ix, 22

[6] Arzumanov, S., Bondarenko, L., Morozov, V. I., Panin, Y. N., and Chernyavsky, S. (2012). Analysis and correction of the measurement of the neutron lifetime. *JETP letters*, 95(5):224–228. ix, 22

[7] Bar-Cohen, Y. (2016). *Low Temperature Materials and Mechanisms*. CRC Press. xiv, 126, 127

[8] Beck, M., Ayala Guardia, F., Borg, M., Kahlenberg, J., Muñoz Horta, R., Schmidt, C., Wunderle, A., Heil, W., Maisonobe, R., Simson, M., Soldner, T., Virot, R., Zimmer, O., Klopf, M., Konrad, G., Baeßler, S., Glück, F., and Schmidt, U. (2020). Improved determination of the $\beta-\overline{\nu}_e$ angular correlation coefficient a in free neutron decay with the aSPECT spectrometer. *Phys. Rev. C*, 101:055506. 10

[9] Becker, W., Deruytter, A. J., and Wartena, J. (1971). In *Proceedings of the Symposium on Neutron Standards and Flux Normalization*, page 125. 88

[10] Becquerel, H. (1896). Sur les radiations invisibles emises par les corps phosphorescents. *Comptes rendus de l'Academie des Sciences*, Paris 122:501–503. 1

[11] Bergman, A. A. and Shapiro, F. L. (1961). *JETP*, 13:5. 45, 88

[12] Berkner, K., Pyle, R., and Stearns, J. (1970). Cross-sections for electron capture by 0.3- to 70-keV deuterons in h2, h2o, CO, CH4and c8f16gases. *Nuclear Fusion*, 10(2):145–149. 126

[13] Birge, N. (2019). *Measurement of the Fierz Interference Term for Calcium-45*. PhD thesis, The University of Tennessee, Knoxville. 12

[14] Blucher, E. and Marciano, W. (2019). v_{ud}, v_{us}, the cabibbo angle, and ckm unitarity. 11

[15] Blucher, E. and Marciano, W. (2020). v_{ud}, v_{us}, the cabibbo angle, and ckm unitarity. 11

[16] Blucher, E. and Marciano, W. (2021). v_{ud}, v_{us}, the cabibbo angle, and ckm unitarity. 12, 13

[17] Brown, D., Chadwick, M., Capote, R., Kahler, A., Trkov, A., Herman, M., Sonzogni, A., Danon, Y., Carlson, A., Dunn, M., Smith, D., Hale, G., Arbanas, G., Arcilla, R., Bates, C., Beck, B., Becker, B., Brown, F., Casperson, R., Conlin, J., Cullen, D., Descalle, M.-A., Firestone, R., Gaines, T., Guber, K., Hawari, A., Holmes, J., Johnson, T., Kawano, T., Kiedrowski, B., Koning, A., Kopecky, S., Leal, L., Lestone, J., Lubitz, C., Márquez Damián, J., Mattoon, C., McCutchan, E., Mughabghab, S., Navratil, P., Neudecker, D., Nobre, G., Noguere, G., Paris, M., Pigni, M., Plompen, A., Pritychenko, B., Pronyaev, V., Roubtsov, D., Rochman, D., Romano, P., Schillebeeckx, P., Simakov, S., Sin, M., Sirakov, I., Sleaford, B., Sobes, V., Soukhovitskii, E., Stetcu, I., Talou, P., Thompson, I., van der Marck, S., Welser-Sherrill, L., Wiarda, D., White, M., Wormald, J., Wright, R., Zerkle, M., Žerovnik, G., and Zhu, Y. (2018). Endf/b-viii.0: The 8th major release of the nuclear reaction data library with cielo-project cross sections, new standards and thermal

scattering data. *Nuclear Data Sheets*, 148:1–142. Special Issue on Nuclear Reaction Data. 33

[18] Burgess, C. P. and Moore, G. D. (2006). *The standard model: A primer*. Cambridge University Press. 6

[19] Byrne, J., Dawber, P., Spain, J., Dewey, M., Gilliam, D., Greene, G., Lamaze, G., Williams, A., Pauwels, J., Eykens, R., et al. (1989). Determination of the neutron lifetime by counting trapped protons. *Nuclear Instruments and Methods in Physics Research Section A: Accelerators, Spectrometers, Detectors and Associated Equipment*, 284(1):116–119. 26

[20] Byrne, J. and Dawber, P. G. (1993). *Nucl. Instrum. Meth. A*, 332:363. 91

[21] Byrne, J., Dawber, P. G., Habeck, C. G., Smidt, S. J., Spain, J. A., and Williams (1996). *Europhys. Lett.*, 33:187. ix, 22, 23

[22] Byrne, J., Dawber, P. G., Spain, J. A., Williams, A. P., Dewey, M. S., Gilliam, D. M., Greene, G. L., Lamaze, G. P., Scott, R. D., Pauwels, J., Eykens, R., and Lamberty, A. (1990). Measurement of the neutron lifetime by counting trapped protons. *Phys. Rev. Lett.*, 65(3):289–292. 23

[23] Byrne, J. and Worcester, D. L. (2019). The neutron lifetime anomaly and charge exchange collisions of trapped protons. *J. Phys. G*, 46(8):085001. 126

[24] Cabibbo, N., Swallow, E. C., and Winston, R. (2004). Semileptonic hyperon decays and cabibbo-kobayashi-maskawa unitarity. *Phys. Rev. Lett.*, 92:251803. 13

[25] Carlson, A. D. (1985). New measurements of the ratio of the ^{10}b(n,α) to ^{6}li(n,t) cross sections in the ev energy region. In *Proceedings of the International Conference on Nuclear Data for Basic and Applied Science*, page 1451. 88

[26] Carlson, A. D. et al. (2007). An international neutron cross section standards evaluation. In *Proceedings of the 2007 International Conference on Nuclear Data for Science and Technology - ND 2007*, page 1233. 88

[27] Chadwick, J. (1932). Possible Existence of a Neutron. *Nature*, 129:312. 2

[28] Chadwick, J. and Goldhaber, M. (1934). A nuclear photo-effect - disintegration of the diplon by gamma rays. *Nature*, 134:237–238. 2

[29] Chadwick, J. and Goldhaber, M. (1935). The Nulcear Photoelectric Effect. *Proc. R. Soc.*, Lond A, 151:479–493. 2

[30] Chowdhurti, Z. (2000). *Precision Neutron Flux Measurement and Advancement Using the Alpha Gamma Technique*. PhD thesis, Indiana University. 46

[31] Cook, J. (2009). Design and estimated performance of a new neutron guide system for the NCNR expansion project. *Rev. Sci. Instruments*, 80(2). 85

[32] Cooke, R. and Fumagalli, M. (2018). Measurement of the primordial helium abundance from the intergalactic medium. 14

[33] Cowan, C. L., Reines, F., Harrison, F. B., Kruse, H. W., and McGuire, A. D. (1956). Detection of the free neutrino: A Confirmation. *Science*, 124:103–104. 2

[34] Cyburt, R. H., Fields, B. D., Olive, K. A., and Yeh, T.-H. (2016). Big bang nucleosynthesis: Present status. *Reviews of Modern Physics*, 88(1). 14

[35] Denecke, B., Eykens, R., Pauwels, J., Robouch, P., Gilliam, D., Hodge, P., Hutchinson, J., and Nico, J. (1999). Characterization of actinide targets by low solid-angle alpha particle counting. *Nuclear Instruments & Methods in Physics Research Section A-accelerators Spectrometers Detectors and Associated Equipment - NUCL INSTRUM METH PHYS RES A*, 438:124–130. 81

[36] Dubbers, D. and Schmidt, M. G. (2011). The neutron and its role in cosmology and particle physics. *Reviews of Modern Physics*, 83(4):1111. 6

[37] Ezhov, V. F., Andreev, A. Z., Ban, G., Bazarov, B. A., Geltenbort, P., Glushkov, A. G., Knyazkov, V. A., Kovrizhnykh, N. A., Krygin, G. B., Naviliat-Cuncic, O., and Ryabov, V. L. (2014). Measurement of the neutron lifetime with ultra-cold neutrons stored in a magneto-gravitational trap. ix, 22

[38] Fermi, E. (1934). An attempt of a theory of beta radiation. 1. *Z. Phys.*, 88:161–177. 2, 3

[39] Feynman, R. P. and Gell-Mann, M. (1958). Theory of the fermi interaction. *Phys. Rev.*, 109:193–198. 5

[40] Frauenfelder, H., Bobone, R., von Goeler, E., Levine, N., Lewis, H. R., Peacock, R. N., Rossi, A., and De Pasquali, G. (1957). Parity and the polarization of electrons from co^{60}. *Phys. Rev.*, 106:386–387. 5

[41] Friedman, J. I. and Telegdi, V. L. (1957). Nuclear emulsion evidence for parity nonconservation in the decay chain $\pi^+ \to \mu^+ \to e^+$. *Phys. Rev.*, 106:1290–1293. 5

[42] GaGe (2022). High-speed digitizers / oscilloscopes. 44

[43] Gamow, G. and Teller, E. (1936). Selection rules for the β-disintegration. *Phys. Rev.*, 49:895–899. 3

[44] Garwin, R. L., Lederman, L. M., and Weinrich, M. (1957). Observations of the failure of conservation of parity and charge conjugation in meson decays: the magnetic moment of the free muon. *Phys. Rev.*, 105:1415–1417. 5

[45] Gilbody, H. B. and Hasted, J. B. (1957). Anomalies in the adiabatic interpretation of charge-transfer collisions. *Proceedings of the Royal Society A*, 238(1214). 126

[46] Gilliam, D., Greene, G., and Lamaze, G. (1989). Absolute neutron counting based on b-10 alpha-gamma coincidence methods. *Nuclear Instruments and Methods in Physics Research Section A: Accelerators, Spectrometers, Detectors and Associated Equipment*, 284(1):220–222. 37, 79

[47] Gilliam, D. M., Lamaze, G. P., Dewey, M. S., and Greene, G. L. (1993). Mass assay and uniformity tests of boron targets by neutron beam methods. *Nucl. Instrum. Methods A*, 334:149–153. 89

[48] Glashow, S. L. and Iliopoulos, J. (1971). Divergences of massive yang-mills theories. *Phys. Rev. D*, 3:1043–1045. 5

[49] Goldhaber, M., Grodzins, L., and Sunyar, A. W. (1958). Helicity of neutrinos. *Phys. Rev.*, 109:1015–1017. 5

[50] Gonzalez, F. M. et al. (2021). An improved neutron lifetime measurement with UCNτ. ix, 12, 18, 22

[51] Gorchtein, M. (2019). γw box inside out: Nuclear polarizabilities distort the beta decay spectrum. *Phys. Rev. Lett.*, 123:042503. 9

[52] Hardy, J. C. and Towner, I. S. (2005). New limits on fundamental weak-interaction parameters from superallowed β decay. *Phys. Rev. Lett.*, 94:092502. 5

[53] Hardy, J. C. and Towner, I. S. (2020). Superallowed $0^+ \rightarrow 0^+$ nuclear β decays: 2020 critical survey, with implications for V_{ud} and ckm unitarity. *Phys. Rev. C*, 102:045501. 8, 12

[54] Higgs, P. W. (1964). Broken symmetries, massless particles and gauge fields. *Phys. Lett.*, 12:132–133. 5

[55] Hirota, K. et al. (2020). Neutron lifetime measurement with pulsed cold neutrons. ix, 19, 22

[56] Jackson, J. D. (1975). *Classical electrodynamics; 2nd ed.* Wiley, New York, NY. 92

[57] Jackson, J. D., Treiman, S. B., and Wyld Jr, H. W. (1957). Possible tests of time reversal invariance in beta decay. *Physical Review*, 106(3):517. 9

[58] Jordanov, V. T. and Knoll, G. F. (1994). Digital synthesis of pulse shapes in real time for high resolution radiation spectroscopy. *Nuclear Instruments and Methods in Physics Research Section A*, 345(2):337–345. 52, 53

[59] Kibdi, T., Burrows, T., Trzhaskovskaya, M., Davidson, P., and Nestor, C. (2008). Evaluation of theoretical conversion coecients using bricc. *Nuclear Instruments and Methods in Physics Research Section A: Accelerators, Spectrometers, Detectors and Associated Equipment*, 589(2):202–229. 59

[60] Kobayashi, M. and Maskawa, T. (1973). CP Violation in the Renormalizable Theory of Weak Interaction. *Prog. Theor. Phys.*, 49:652–657. 6

[61] Lamaze, G., Gilliam, D., and Williams, A. (1988). Prompt gamma as a fluence rate monitor in neutron beam experiments. *Journal of Radioanalytical and Nuclear Chemistry*, 123(2):551–559. 79

[62] Lawrence, D. J., Wilson, J. T., and Peplowski, P. N. (2021). Space-based Measurements of Neutron Lifetime: Approaches to Resolving the Neutron Lifetime Anomaly. *Nucl. Instrum. Meth. A*, 988:164919. ix, 20, 22

[63] Mampe, W., Bondarenko, L., Morozov, V., Panin, Y. N., and Fomin, A. (1993). Measuring neutron lifetime by storing ultracold neutrons and detecting inelastically scattered neutrons. *JETP LETTERS C/C OF PIS'MA V ZHURNAL EKSPERIMENTAL'NOI TEORETICHESKOI FIZIKI*, 57:82–82. ix, 22

[64] Marciano, W. J. and Sirlin, A. (2006). Improved calculation of electroweak radiative corrections and the value of V_{ud}. *Phys. Rev. Lett.*, 96:032002. 11

[65] Märkisch, B., Mest, H., Saul, H., Wang, X., Abele, H., Dubbers, D., Klopf, M., Petoukhov, A., Roick, C., Soldner, T., and Werder, D. (2019). Measurement of the weak axial-vector coupling constant in the decay of free neutrons using a pulsed cold neutron beam. *Phys. Rev. Lett.*, 122:242501. 9, 12

[66] Meadows, J. W. (1971). In *Proceedings of the Symposium on Neutron Standards and Flux Normalization*, page 129. 88

[67] Nico, J., Dewey, M., Gilliam, D., Wietfeldt, F., Fei, X., Snow, W., Greene, G., Pauwels, J., Eykens, R., Lamberty, A., et al. (2005). Measurement of the neutron lifetime by counting trapped protons in a cold neutron beam. *Phys. Rev. C*, 71:055502. viii, xi, 26, 29, 33, 36, 41, 42, 77, 92, 93, 94, 95, 96, 110, 117, 145, 150, 151, 154

[68] NIST (2021). Neutron scattering lengths and cross sections. 110

[69] Pais, A. (1986). *Inward Bound: of Matter and Forces in the Physical World*. 1

[70] Pattie, Jr., R. W. et al. (2018). Measurement of the neutron lifetime using a magneto-gravitational trap and in situ detection. *Science*, 360(6389):627–632. ix, 18, 22

[71] Pauli, W. (1978). Dear radioactive ladies and gentlemen. *Phys. Today*, 31N9:27. 2

[72] Pauwels, J., Eykens, R., Lamberty, A., Van Gestel, J., Tagziria, H., Scott, R., Byrne, J., Dawber, P., and Gilliam, D. (1991). The preparation and characterisation of 6lif and 10b reference deposits for the measurement of the neutron lifetime. *Nuclear Instruments and Methods in Physics Research Section A: Accelerators, Spectrometers, Detectors and Associated Equipment*, 303(1):133–140. 37, 46

[73] Pauwels, J., Scott, R., Eykens, R., Robouch, P., Van Gestel, J., Verdonck, J., Gilliam, D., and Greene, G. (1995). Improvements in the preparation and areal characterisation of 10b and 6lif reference deposits. *Nuclear Instruments and Methods in Physics Research Section A: Accelerators, Spectrometers, Detectors and Associated Equipment*, 362(1):104–111. Proceedings of the 17th World Conference of the International Nuclear Target Development Society. 37, 46, 89

[74] PDG (2020). Review of Particle Physics. *Progress of Theoretical and Experimental Physics*, 2020(8). 083C01. 6, 8, 10

[75] Peimbert, M. (2008). The primordial helium abundance. 14

[76] Phelps, A. V. (1992). Collisions of h+, h2+, h3+, arh+, h, h, and h2 with ar and of ar+ and arh+ with h2 for energies from 0.1 ev to 10 kev. *Journal of Physical and Chemical Reference Data*, 21(4):883–897. 126, 128

[77] Pichlmaier, A., Varlamov, V., Schreckenbach, K., and Geltenbort, P. (2010). Neutron lifetime measurement with the UCN trap-in-trap MAMBO II. *Phys. Lett. B*, 693:221–226. ix, 20, 22

[78] Počanić, D., Frlež, E., Baranov, V. A., Bertl, W., Brönnimann, C., Bychkov, M., Crawford, J. F., Daum, M., Khomutov, N. V., Korenchenko, A. S., Korenchenko, S. M., Kozlowski, T., Kravchuk, N. P., Kuchinsky, N. A., Li, W., Minehart, R. C., Mzhavia, D.,

Ritchie, B. G., Ritt, S., Rozhdestvensky, A. M., Sidorkin, V. V., Smith, L. C., Supek, I., Tsamalaidze, Z., VanDevender, B. A., Wang, Y., Wirtz, H.-P., and Ziock, K. O. H. (2004). Precise measurement of the $\pi^+ \to \pi^0 e^+ \nu$ branching ratio. *Phys. Rev. Lett.*, 93:181803. 12

[79] Richardson, J. M. (1993). *Precision Neutron Flux Measurement and Advancement Using the Alpha Gamma Technique*. PhD thesis, Harvard University. 46

[80] Robson, J. M. (1950). Radioactive decay of the neutron. *Phys. Rev.*, 78:311–312. 2

[81] Rutherford, E. (1920). Nuclear Constitution of Atoms. *Proc. R. Soc.*, Lond A, 97:374–400. 1

[82] Salam, A. (1968). Weak and Electromagnetic Interactions. *Conf. Proc. C*, 680519:367–377. 5

[83] Scott, R. D., D'hondt, P., Eykens, R., Robouch, P., Reher, D. F. G., Sibbens, G., Pauwels, J., and Gilliam, D. M. (1995). The characterization of ^{10}b and ^{6}lif reference deposits by measurement of neutron-induced charged particle reactions - a second campaign. *Nucl. Instrum. Methods A*, 362:151–159. 89, 110

[84] Scott, R. D., Pauwels, J., Eykens, R., Byrne, J., Dawber, P. G., and Gilliam, D. M. (1992). The characterisation of ^{1}0b and ^{6}lif reference deposits by the measurement of neutron induced charged particle reactions. *Nucl. Instrum. Methods A*, 314:163–170. 89

[85] Sears, V. F. (1992). Neutron scattering lengths and cross sections. *Neutron News*, 3(3). 110

[86] Seng, C. Y., Gorchtein, M., and Ramsey-Musolf, M. J. (2019). Dispersive evaluation of the inner radiative correction in neutron and nuclear β-decay. 6, 11

[87] Serebrov, A., Varlamov, V., Kharitonov, A., Fomin, A., Pokotilovski, Y., Geltenbort, P., Butterworth, J., Krasnoschekova, I., Lasakov, M., Tal'Daev, R., et al. (2005). Measurement of the neutron lifetime using a gravitational trap and a low-temperature fomblin coating. *Physics Letters B*, 605(1):72–78. ix, 20, 22

[88] Serebrov, A. P. et al. (2018). Neutron lifetime measurements with a large gravitational trap for ultracold neutrons. *Phys. Rev. C*, 97(5):055503. ix, 15, 22

[89] Shahi, C., Arif, M., Cory, D., Mineeva, T., Nsofini, J., Sarenac, D., Williams, C., Huber, M., and Pushin, D. (2016). A new polarized neutron interferometry facility at the {NCNR}. *Nuclear Instruments and Methods in Physics Research Section A: Accelerators, Spectrometers, Detectors and Associated Equipment*, 813:111 – 122. 40

[90] Snell, A. H. and Miller, L. (1948). On the decay of the neutron. *Phys. Rev.*, 74:1217. 2

[91] Snell, A. H., Pleasonton, F., and McCord, R. V. (1950). Radioactive decay of the neutron. *Phys. Rev.*, 78:310–311. 2

[92] Stebbings, R. F., Smith, A. C. H., and Ehrhardt, H. (1964). Charge transfer between oxygen atoms and o+ and h+ ions. *Journal of Geophysical Research (1896-1977)*, 69(11):2349–2355. 126

[93] Stedeford, J. B. H. and Hasted, J. B. (1955). Further investigations of charge exchange and electron detachment - I. Ion energies 3 to 40 keV - II. Ion energies 100 to 4000 eV. *Proceedings of the Royal Society A*, 227(1171). 126, 128

[94] Sternberg, M. G., Segel, R., Scielzo, N. D., Savard, G., Clark, J. A., Bertone, P. F., Buchinger, F., Burkey, M., Caldwell, S., Chaudhuri, A., Crawford, J. E., Deibel, C. M., Greene, J., Gulick, S., Lascar, D., Levand, A. F., Li, G., Pérez Galván, A., Sharma, K. S., Van Schelt, J., Yee, R. M., and Zabransky, B. J. (2015). Limit on tensor currents from ^{8}Li β decay. *Phys. Rev. Lett.*, 115:182501. 5

[95] Steyerl, A., Pendlebury, J. M., Kaufman, C., Malik, S. S., and Desai, A. M. (2012). Quasielastic scattering in the interaction of ultracold neutrons with a liquid wall and application in a reanalysis of the mambo i neutron-lifetime experiment. *Phys. Rev. C*, 85:065503. ix, 22

[96] Sudarshan, E. C. G. and Marshak, R. E. (1958). Chirality invariance and the universal fermi interaction. *Phys. Rev.*, 109:1860–1862. 5

[97] 't Hooft, G. (1971). Renormalizable Lagrangians for Massive Yang-Mills Fields. *Nucl. Phys. B*, 35:167–188. 5

[98] Tawara, H. (1978). Cross sections for charge transfer of hydrogen beams in gases and vapors in the energy range 10 ev–10 kev. *Atomic Data and Nuclear Data Tables*, 22(6):491–525. 126

[99] Towner, I. (1992). The nuclear-structure dependence of radiative corrections in superallowed fermi beta-decay. *Nuclear Physics A*, 540(3):478–500. 9

[100] Weast, R. C. and Astle, M. J. (1982). *Handbook of Chemistry and Physics*. CRC Press, Boca Raton, FL. 27

[101] Weinberg, S. (1967). A model of leptons. *Phys. Rev. Lett.*, 19:1264–1266. 5

[102] Wietfeldt, F. E. et al. (2020). A Comment on "The possible explanation of neutron lifetime beam anomaly" by A. P. Serebrov, et al. xiv, 127

[103] Wilkinson, D. (1998). Phase space for neutron beta-decay: an update. *Nuclear Instruments and Methods in Physics Research Section A: Accelerators, Spectrometers, Detectors and Associated Equipment,*, 404:305–310. 12

[104] Wilson, J. T., Lawrence, D. J., Peplowski, P. N., Eke, V. R., and Kegerreis, J. A. (2020a). Measurement of the Free Neutron Lifetime using the Neutron Spectrometer on NASA's Lunar Prospector Mission. 20

[105] Wilson, J. T., Lawrence, D. J., Peplowski, P. N., Eke, V. R., and Kegerreis, J. A. (2020b). Space-based measurement of the neutron lifetime using data from the neutron spectrometer on nasa's messenger mission. *Phys. Rev. Research*, 2:023316. 20

[106] Wu, C. S., Ambler, E., Hayward, R. W., Hoppes, D. D., and Hudson, R. P. (1957). Experimental test of parity conservation in beta decay. *Phys. Rev.*, 105:1413–1415. 5

[107] Yue, A. (2011). *Progress Towards a Redetermination of the Neutron Lifetime through the Absolute Determination of the Neutron Flux*. PhD thesis, The University of Tennessee, Knoxville. xi, 37, 85, 86, 87, 88

[108] Yue, A., Dewey, M., Gilliam, D., Greene, G., Laptev, A., Nico, J., Snow, W., and Wietfeldt, F. (2013). Improved Determination of the Neutron Lifetime. *Phys. Rev. Lett.*, 111(22):222501. ix, 18, 22, 37, 87, 110, 154

[109] Ziegler, J. (2013). The stopping and range of ions in matter. 117

[110] Ziegler, J., Biersack, J., and Ziegler, M. (2015). *The Stopping and Range of Ions in Matter*. 119

Appendices

A Example of 1/v Neutron Flux Monitor SCA Threshold Counts

Run	T_{11}	T_{21}	T_{31}	T_{41}	T_{12}	T_{22}	T_{32}	T_{42}	T_{13}	T_{23}	T_{33}	T_{43}	T_{14}	T_{24}	T_{34}	T_{44}
0	19825	19819	9961	57	20413	20403	10171	15	20373	20368	10190	12	20335	20329	10238	37
1	20035	20025	9945	66	20259	20247	9980	14	20340	20334	10274	16	20202	20192	10065	34
2	20158	20151	10094	43	20277	20271	10141	11	20166	20160	10027	16	20400	20391	10193	37
3	20239	20232	10065	63	20416	20407	10392	17	20209	20197	10041	13	20094	20088	10109	42
4	20229	20224	10041	64	20347	20337	10161	12	20121	20115	9990	20	20282	20265	10272	36
5	20192	20182	10000	44	20424	20419	10049	10	20501	20487	10207	15	20081	20072	9945	37
6	20236	20227	10049	52	20067	20051	10135	9	20227	20217	9994	9	19935	19930	10045	34
7	20085	20073	10059	50	20406	20395	10095	6	20459	20450	10093	22	20132	20126	10102	38
8	19974	19963	9815	85	20203	20191	10178	18	20105	20097	10079	13	20068	20062	10001	61
9	20179	20165	10029	61	20295	20284	10234	15	20307	20295	10176	8	20255	20244	10123	35
10	20281	20271	10138	45	20076	20065	10060	12	20070	20062	10005	13	20427	20420	10225	22
11	20009	20003	10078	48	20373	20359	10125	12	20375	20368	10284	17	20144	20131	10097	29
12	20011	20000	9887	50	20328	20318	10268	14	20370	20365	10184	15	20116	20108	10282	21
13	20246	20237	10183	43	20498	20490	10325	8	20061	20057	10003	11	20092	20083	9909	29
14	20037	20032	10037	74	20299	20290	10061	12	20354	20354	10203	11	20264	20258	10107	41
15	20275	20269	10305	355	20030	20023	10117	16	20530	20520	10259	14	20311	20300	10243	272
16	20228	20216	10231	73	20102	20092	10095	9	20457	20447	10383	27	20089	20078	9930	35
17	20015	20007	9950	67	20341	20325	10159	9	20240	20231	10133	5	20363	20356	10222	42
18	19840	19831	10184	369	20265	20257	10079	10	20477	20472	10265	17	20382	20374	10118	221
19	20301	20289	10040	62	20206	20196	10125	16	20176	20171	10137	10	20128	20121	10137	46
20	20091	20086	9992	44	20370	20365	10149	12	20398	20387	10256	12	20369	20361	10250	46
21	19920	19908	9904	77	20256	20246	10190	10	20464	20459	10166	9	20189	20179	10075	35
22	20251	20235	10035	58	20193	20179	10102	11	20354	20349	10297	13	20436	20428	10157	22
23	20204	20197	10117	41	20138	20131	10055	18	20188	20178	10177	16	20167	20161	10200	27
24	20120	20105	10030	51	20476	20459	10139	10	20198	20186	9996	13	20353	20346	10042	38
25	20034	20024	9910	59	20242	20234	10075	13	20310	20304	10189	9	20342	20332	10241	34
26	20268	20258	10194	38	20361	20341	10150	14	20207	20199	10204	12	20480	20469	10181	23
27	20030	20021	10142	49	20296	20290	10140	11	20324	20314	10285	12	20556	20550	10185	39
28	20180	20169	10201	43	20287	20282	10230	14	20395	20385	10311	22	19959	19952	9946	47
29	20114	20111	9963	45	20422	20414	10133	14	20454	20447	10185	18	20177	20167	10082	35

Figure 3: Example of the text file of the 16 integer values from the 1/v neutron monitor SCAs. Each row is a single run, the first column is the run number, additional columns are the SCA threshold values T_{ij}, where i is the threshold label and j is the detector label.

B Trapezoid Filter Recursion Relation Used in Analysis

$$h(i) = \begin{cases} h(i-1) + v(i); & i < \tau_{rise} \\ h(i-1) + v(i) - v(i-\tau_{rise}); & \tau_{rise} \leq i < \tau_{rise} + \tau_{top} \\ h(i-1) + v(i) - v(i-\tau_{rise}) - v(i-\tau_{rise}-\tau_{top}); & \tau_{rise} + \tau_{top} \leq i < 2 * \tau_{rise} + \tau_{top} \\ h(i-1) + v(i) - v(i-\tau_{rise}) - v(i-\tau_{rise}-\tau_{top}) + v(i-2*\tau_{rise}-\tau_{top}); & i \leq 2 * \tau_{rise} + \tau_{top} \end{cases}$$

C Collection of Pseudodata Waveforms Showing a Wide Variety of Proton and Background Events.

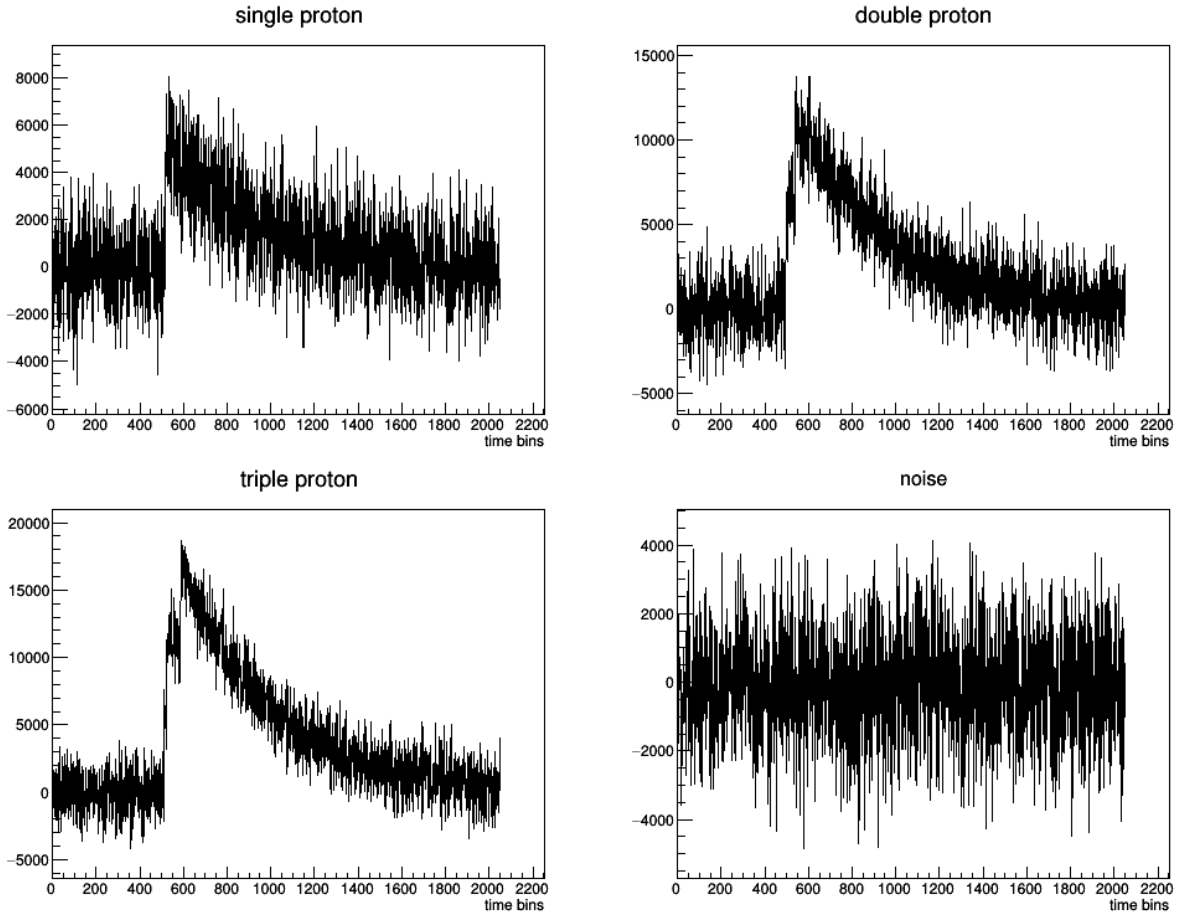

Figure 4: Example of pseudodata waveforms showing the most common signal types.

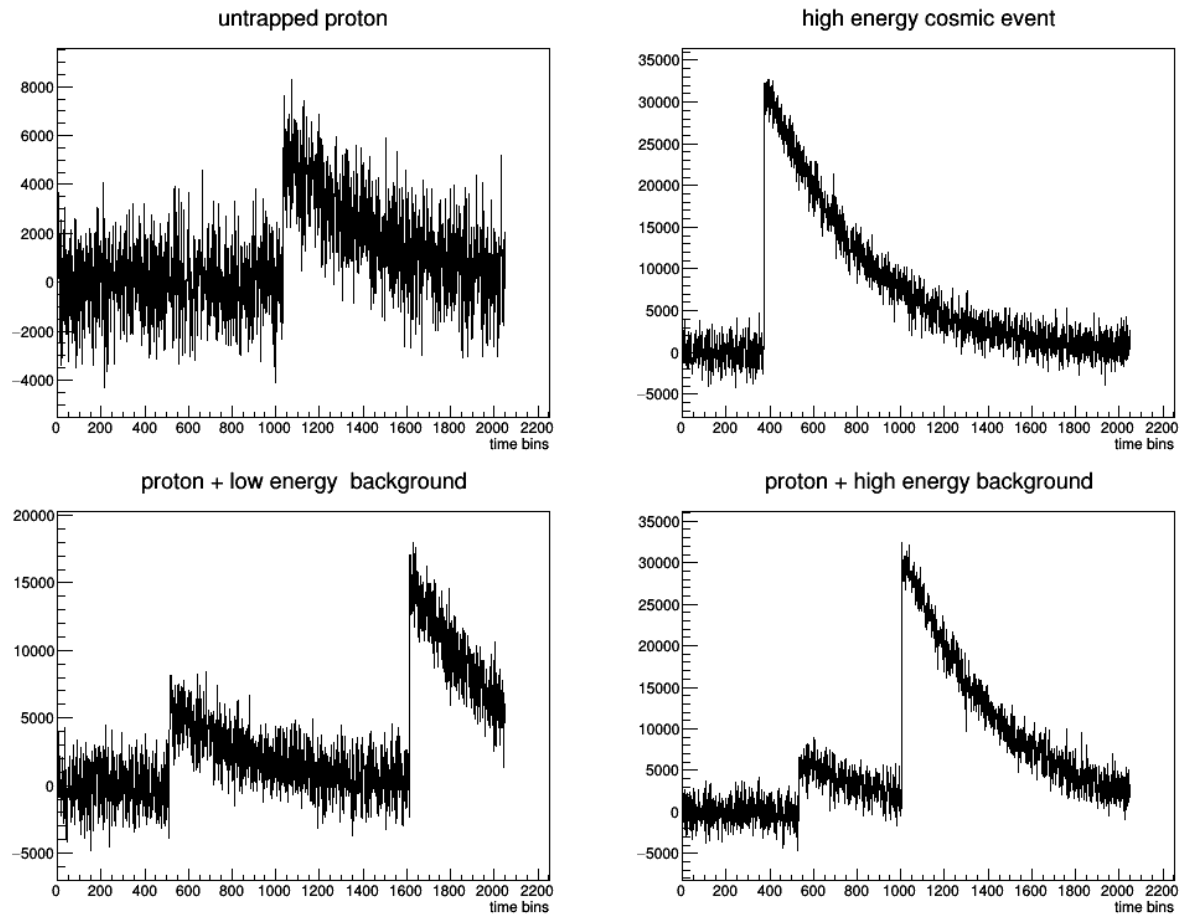

Figure 5: Example of pseudodata waveforms of the most common background events.

D Damage Calculation Model Descriptions from SRIM Textbook

D.1 Ion Distribution and Quick Calculation of Damage

This option should be used if you don't care about details of target damage or sputtering. The damage calculated with this option will be the quick statistical estimates based on the Kinchin-Pease formalism (see section Physics of Recoil Cascades for details about target damage). The following data will be calculated correctly: Final distribution of ions in the target, Ionization energy loss by the ion into the target, Energy transferred to recoil atoms, Backscattered Ions and Transmitted Ions. You will get identical ion range results as when you use the Full Damage Cascade option below, since the random number generator for the ions is separate from that used for the recoils. This is useful to compare calculations.

D.2 Detailed Calculation with Full Damage Cascades

This option follows every recoiling atom until its energy drops below the lowest displacement energy of any target atom. Hence all collisional damage to the target is analyzed. The one exception is for very rare massive cascades which exceed 20,000 atoms. At this point TRIM runs out of memory, and an error message is posted indicating that the limit of 20,000 recoiling atoms in a single cascade has been exceeded. The calculation continues after the message is posted. This error can be eliminated using the datafile:

`\Data\TRIM.cfg`.

See the later section in this chapter on "Changing Maximum Size of Recoil Cascades (TRIM.cfg)"

D.3 Monolayer Collision Steps

This calculation requires TRIM to make the ion have a collision in each monolayer of the target. This omits any use of the Free Flight Path, described in Chapter 7, and every collision will be calculated without any approximations. The results of using this option

will ultimately give the same averaged quantities such as mean range, ionization, damage, etc., but the calculation will take far longer to execute. This type of calculation is essential for special applications such as sputtering (below) and to generate data on every possible collision in the file COLLISON.txt (see Chapter 9 for more details).

E Collection of Neutron Lifetime vs Trapping Time Plots for Post Silicon Window Installation

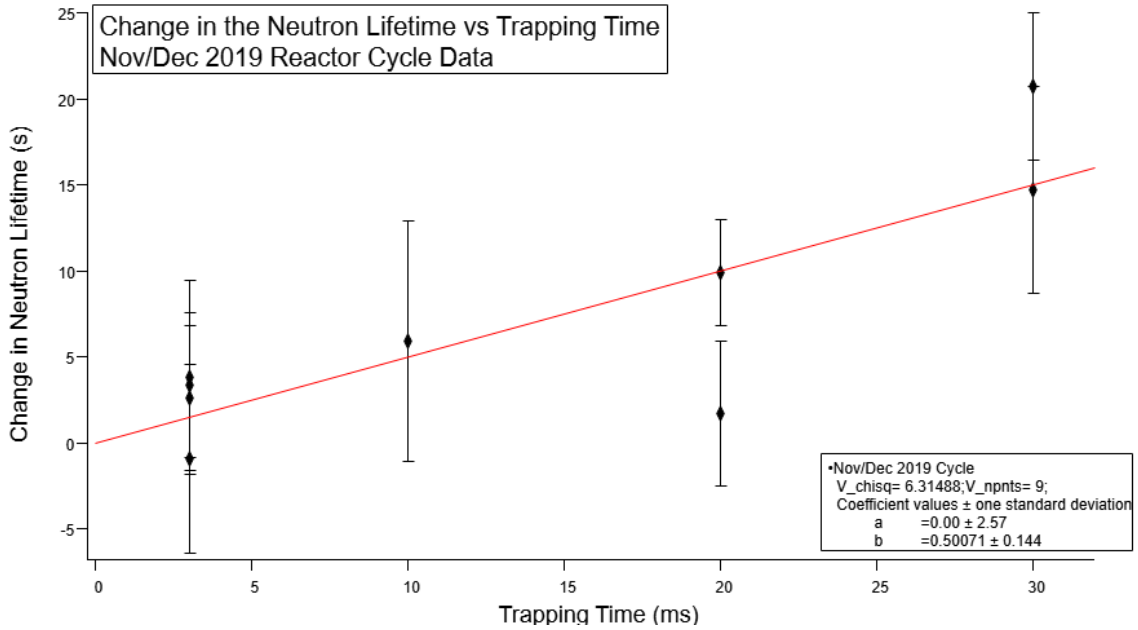

Figure 6: Change in measured neutron lifetime vs trapping time, November/December 2019 reactor cycle.

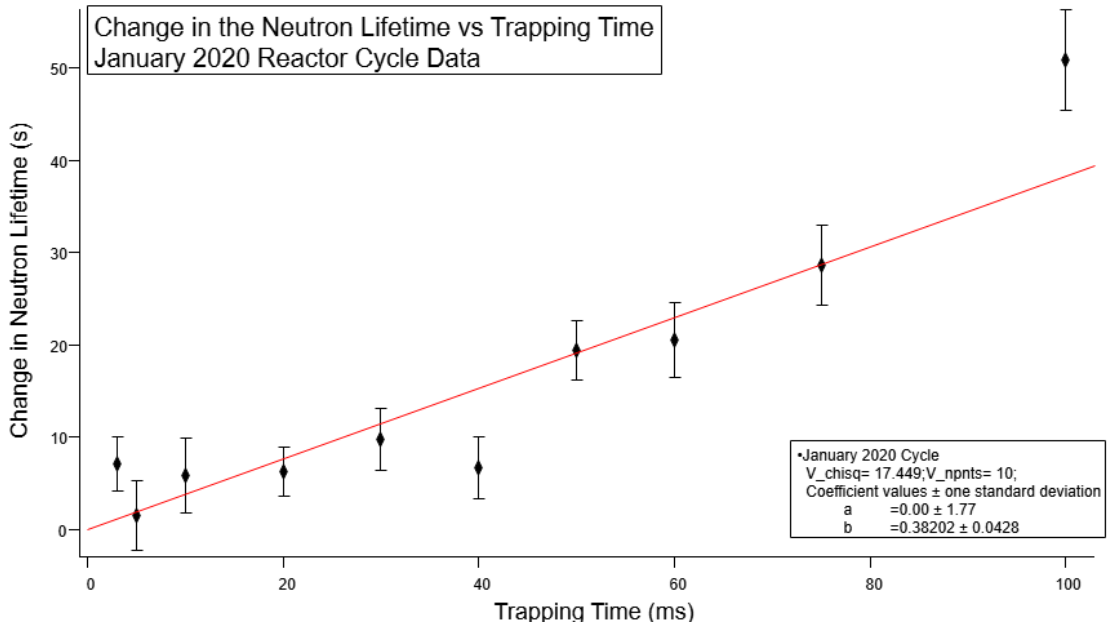

Figure 7: Change in measured neutron lifetime vs trapping time, January 2020 reactor cycle.

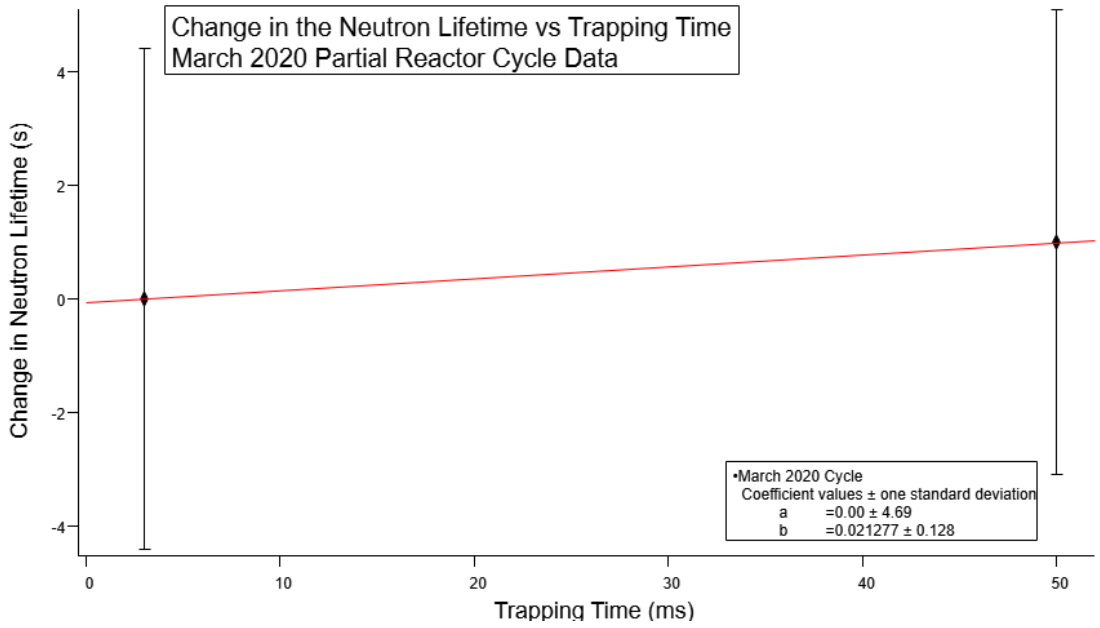

Figure 8: Change in measured neutron lifetime vs trapping time, March 2020 reactor cycle.

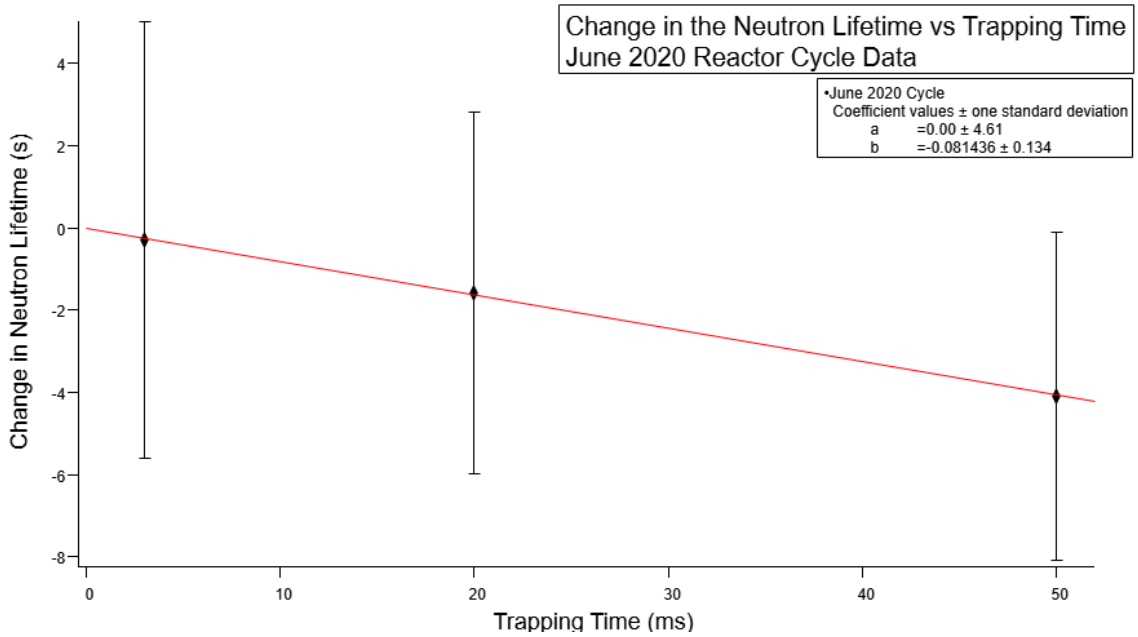

Figure 9: Change in measured neutron lifetime vs trapping time, June 2020 reactor cycle.

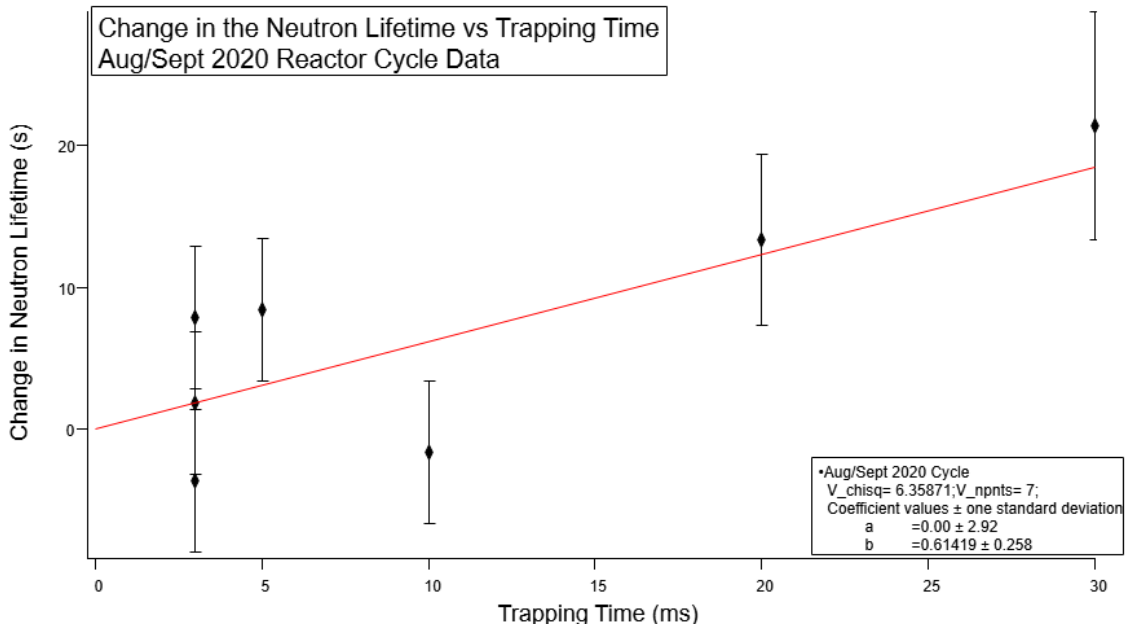

Figure 10: Change in measured neutron lifetime vs trapping time, August/September 2020 reactor cycle.

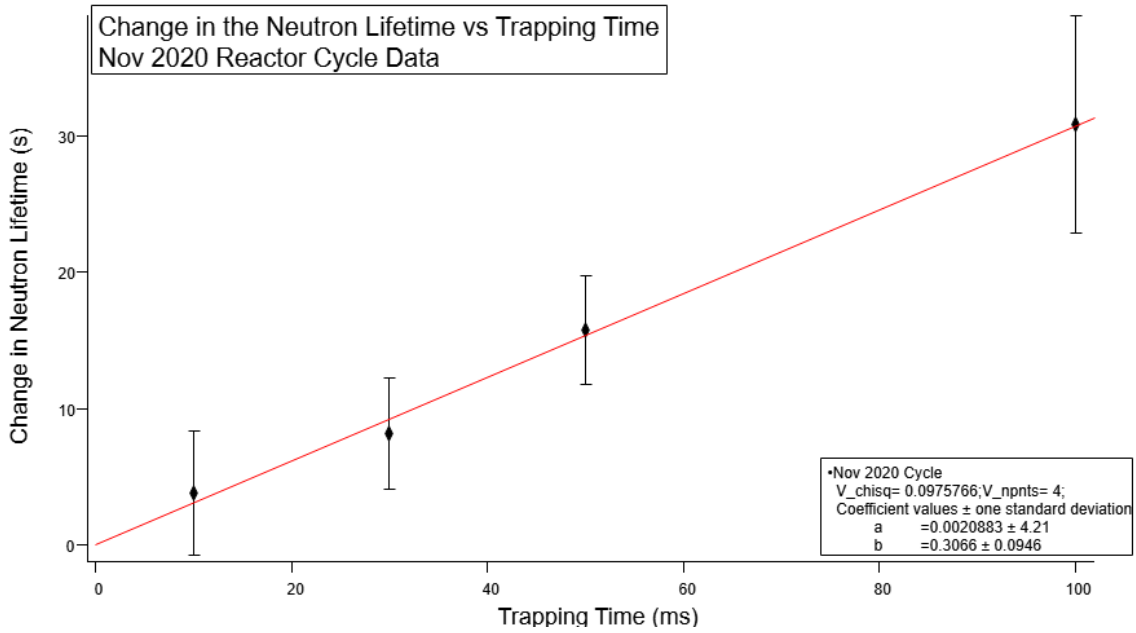

Figure 11: Change in measured neutron lifetime vs trapping time, November 2020 reactor cycle.

Vita

Jimmy was born and raised in Sevierville, Tennessee. During high school Jimmy attended the Tennessee Governor's School for emerging technologies at Tennessee Technological University, where he developed his interest in physics. Upon graduation Jimmy enrolled at the University of Tennessee, Knoxville, where he received a Bachelor of Science degree in Physics with a minor in Mathematics. Jimmy was named to the Dean's List all eight semesters during this time and graduated with the distinction of magna cum laude. After graduation Jimmy chose to attend graduate school at the University of Tennessee to pursue a Doctor of Philosophy degree is Nuclear Physics. After this first year of graduate school Jimmy joined the neutron physics group and began work on multiple experiments. Jimmy's research interests include the fundamental symmetries of the weak interaction and charged particle detection. After graduation Jimmy accepted a postdoctoral position at Syracuse University.